DEVELOPMENT OF A NOVEL NITRIC OXIDE SENSOR USING NITROPHORIN 4 ON AN ATTENUATED TOTAL REFLECTANCE PLATFORM

by

John Laurence Lemon

_____

A Dissertation Submitted to the Faculty of the

DEPARTMENT OF CHEMISTRY AND BIOCHEMISTRY

In Partial Fulfillment of the Requirements

For the Degree of

DOCTOR OF PHILOSOPHY

WITH A MAJOR IN CHEMISTRY

In the Graduate College

THE UNIVERSITY OF ARIZONA

2012

THE UNIVERSITY OF ARIZONA
GRADUATE COLLEGE

As members of the Dissertation Committee, we certify that we have read the dissertation prepared by JOHN L. LEMON

entitled Development of a Novel Nitric Oxide Sensor Using Nitrophorin 4 on an

Attenuated Total Reflectance Platform

and recommend that it be accepted as fulfilling the dissertation requirement for the

Degree of Doctor of Philosophy

_____ Date: December 20, 2012
Dr. William R. Montfort

_____ Date: December 20, 2012
Dr. S. Scott Saavedra

_____ Date: December 20, 2012
Dr. Katrina M. Miranda

_____ Date: December 20, 2012
Dr. Michael L. Heien

Final approval and acceptance of this dissertation is contingent upon the candidate's submission of the final copies of the dissertation to the Graduate College.

I hereby certify that I have read this dissertation prepared under my direction and recommend that it be accepted as fulfilling the dissertation requirement.

_____ Date: December 20, 2012
Dissertation Director: Dr. William R. Montfort

STATEMENT BY AUTHOR

This dissertation has been submitted in partial fulfillment of requirements for an advanced degree at the University of Arizona and is deposited in the University Library to be made available to borrowers under rules of the Library.

Brief quotations from this dissertation are allowable without special permission, provided that accurate acknowledgment of source is made. Requests for permission for extended quotation from or reproduction of this manuscript in whole or in part may be granted by the head of the major department or the Dean of the Graduate College when in his or her judgment the proposed use of the material is in the interests of scholarship. In all other instances, however, permission must be obtained from the author.

SIGNED: JOHN LAURENCE LEMON

ACKNOWLEDGMENTS

I would like to start by thanking my mother Despina, my sister Alexis, my stepmother Susan, and especially, my father Larry, for their support during this process. I would like to thank my advisor, Bill, for his guidance, and allowing me initiate and develop my own research project. I would also like to thank my committee, particularly Dr. Miranda and Dr. Saavedra for their assistance with my work.

There are so many people and places that have influenced my journey it's difficult to acknowledge everyone. This path began at Henninger high school with Ms. Emord, where I began to ponder the natural world. I owe much of my development to SUNY Fredonia and the talented faculty there. Without the knowledge they imparted, this would not have been possible. I would also like to recognize my first mentors in the laboratory, Thai Le, Scott Long, and especially Tomika Velarde. Their approach to research was a fine example.

I would like to thank my Montfort lab colleagues, Aaron Issaian, Brad Fritz, Mark Lee, and Andrzej Weichsel for their development of protein constructs, which they graciously allowed me to use. Aaron Issaian in particular has made a material contribution to the work presented herein, and his help has been critical. I could not ask for a better colleague in the laboratory. I would also like to thank Stacy Elliot and Jacquie Brailey for teaching me a bit about molecular biology. A special thanks to the rest of the Montfort group, including but not limited to, Saumya Ramanathan, Juliana The and Rahul Purohit, who helped make going to work more enjoyable.

I would also like to thank Sue Roberts, Steve Hernandez, Phil Anderson and Tony Day for their help with the transmission electron microscopy project.

This work is dedicated to my best friend, the late Danny Keeler, I know your atoms have already become beautiful things. My friends that are also my family, Bobby Madrid, Aron Arvai, Shawn "Red" Dwyer, Thai Le, Zac Hohman, Damian Gosch, Ben Wachter and Marche Byerley. Most importantly, my partner in life, my love, Anne Simon, who is everything to me. Anne, your love and support have meant the world to me.

TABLE OF CONTENTS

TABLE OF CONTENTS – *continued*

LIST OF FIGURES

LIST OF FIGURES - *continued*

LIST OF FIGURES – *continued*

LIST OF FIGURES - *continued*

LIST OF FIGURES - *continued*

LIST OF FIGURES - *continued*

LIST OF TABLES

ABSTRACT

Nitric oxide plays a major role in physiology and disease pathology. There are many available methods for the detection of NO; however, these techniques typically detect products of nitric oxide decomposition. Herein, I present a novel method of direct nitric oxide detection using a nitrophorin mutant to capture NO on an optical waveguide platform. Nitrophorins are unique among ferric proteins for their ability to bind NO strongly. The spectral shift of the Soret band of the Nitrophorin was used to monitor NO concentration. The limit of detection was found to be 18 nM, and a linear response to 225 nM. The sensor is highly specific, non-destructive and reusable. Detection of NO was demonstrated in a solution of BSA at serum level concentration, and cell culture solution containing 10% FBS. This method allows for direct NO with high specificity, low detection limit and good temporal resolution.

Also described herein are the investigations of the structure of the NO receptor, soluble guanylate cyclase (sGC). sGC is a 150 kDa heterodimeric protein that catalyzes the production of cyclic guanosine monophosphate from guanosine triphosphate, which leads to many downstream affects such as vasodilation. The structural analysis was performed with transmission electron microscopy (TEM). Data presented indicate that the protein is too heterogeneous to be reconstructed with TEM. This is either the result of the sample preparations examined, the purity of the sample, the inherent flexibility or conformational heterogeneity of the protein after applying the sample to the TEM grid.

The final project presented describes the use of silica colloidal crystals for the enhancement of the sensitivity of protein microarrays as a function of silica particle size. Protein microarrays are a tool used to discover biomarkers of diseases, and increasing the sensitivity lowers the limit of detection of the method. This is accomplished by an increase of the surface area available for proteins to bind, and by using silica so that the surface chemistry of the microarray is maintained. It was concluded that 510 nm colloids provide the greatest enhancement of the fluorescence of a BSA ant-BSA-FITC system, providing a 17-fold enhancement over the control.

CHAPTER 1

INTRODUCTION

1.a. Nitric oxide

1.a.1. Nitric oxide in biology

In the early 1980s scientists began studying a molecule that was acted as an endogenous vasodilator in the endothelium of arteries in the early 1980s.[1, 2] The molecule was referred to as endothelium derived relaxation factor (EDRF), and its chemical make-up was unknown until 1987, when it was finally identified as nitric oxide (NO). The identification of NO *in vivo* was a surprise to many because until then it had only been known as an environmental pollutant and toxic gas caused by combustion and lightening. NO was shown early on to be of paramount importance and involved in many physiological processes (Figure 1.1).[3] In 1992 NO was named "molecule of the year" in the journal *Science*. The Nobel prize in medicine was awarded in 1998 to Robert F. Furchgott, Louis Ignarro and Ferid Murad, for the discovery of NO as EDRF.

NO is an important signaling molecule in physiology; it is involved with the regulation of numerous biological activities including cardiovascular,[4] central nervous system[5] and immune response.[6, 7] NO is also implicated in numerous pathological conditions such as cancer,[8] sepsis[9] and arthritis.[6, 10] NO is synthesized *in vivo* by nitric oxide synthases (NOSs) and has recently been shown to also be formed *in vivo* by the reduction of nitrite.[11, 12] NOSs convert oxygen and L-arginine to citrulline and NO, and comes in three isoforms, inducible, endothelial and neuronal NOS.[11] Inducible NOS may

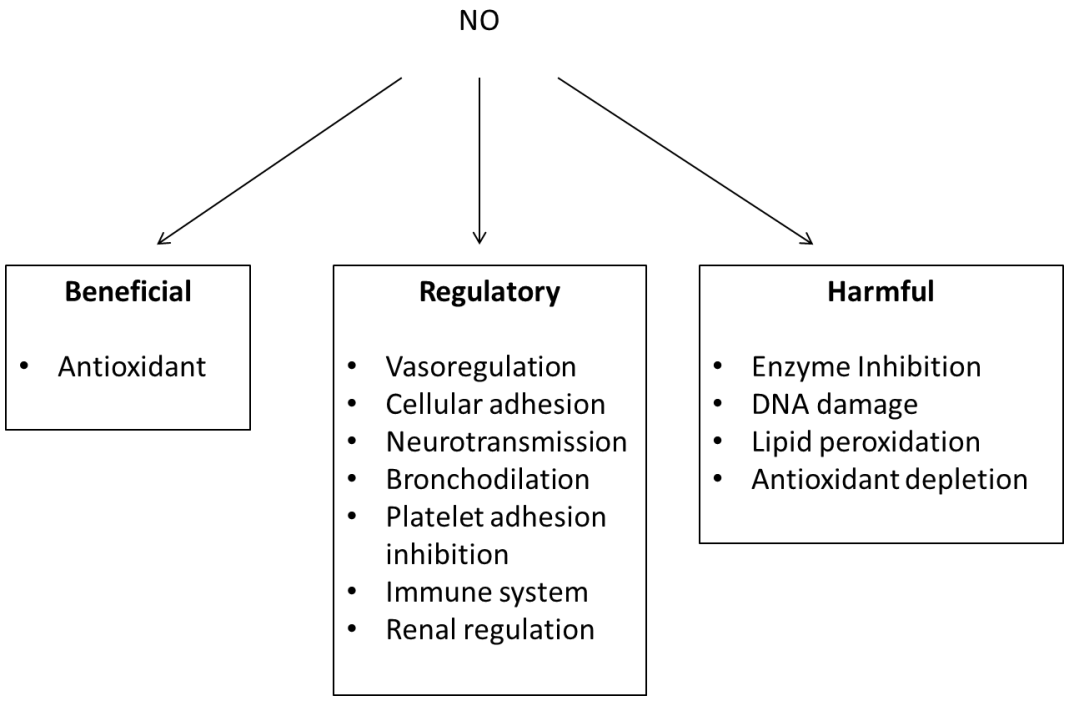

Figure 1.1. Biological roles of NO, adapted from Wink and Mitchell. Adapted with permission from reference 6. Copyright 1998 Elsevier.

be present in many cell types including those in the immune and cardiovascular systems.[11]

It is used by the macrophage immune cells to kill pathogens and tumor cells, and by many cells in response to hypoxia. Neuronal NOS is used in neuronal signaling and endothelial NOS is used for vasodilation (see Figure 1.2). The major target for NO *in vivo* is soluble guanylate cyclase (sGC).[13]

Significant advances in understanding NO biology are hindered by the lack of direct NO detection methods. Monitoring NO concentrations in cell cultures, tissues, organs and bodily fluid has the potential to aid in treatment evaluation and in progression of the disease. The standard ways to evaluate this important molecule is with indirect methods, monitoring products of NO degradation. A selective, sensitive detection method for NO would greatly impact the field and advance this critical science.

1.a.2. Nitric oxide chemistry

Understanding NO chemistry is key for understanding biological function and dysfunction. NO is a diatomic dissolved gas that has a diffusion coefficient of 3300 $\mu m^2/s$ *in vivo*,[14] which makes it extremely mobile and a fast signaling agent. NO has a half-life of only a few seconds *in vivo*.[15, 16] NO is an uncharged molecule with an unpaired electron in an anti-bonding *pi* orbital. NO is lipophilic, with a partition coefficient of ~4, which allows it to easily cross cell membranes, and surprisingly without much reactivity.[15] In solution at low concentrations it reacts with only a few

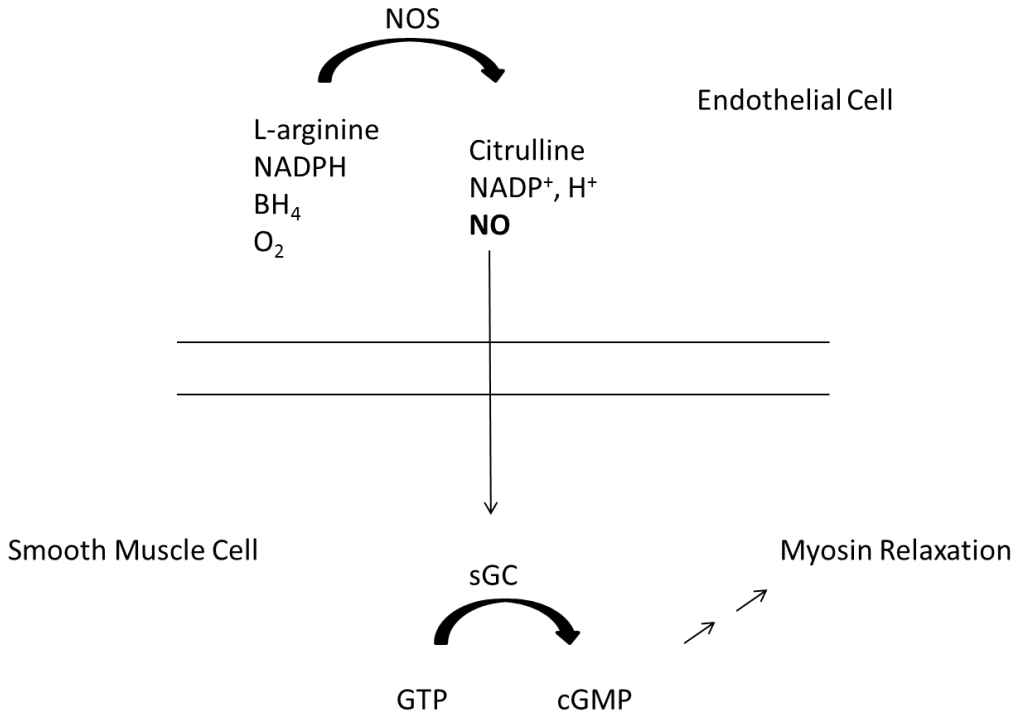

Figure 1.2. Principle mechanism of NO vasodilation in the bloodstream.

other types of molecules including free radicals, oxygen, superoxide, thiols and heme-containing proteins.[16] Thus, for a free radical, it is not very reactive, also evidenced by the fact that it does not react with itself. The rate law of the autoxidation of NO is defined by the equation:[17]

$$-d[NO]/dt = 4k_{aq}[NO]^2[O_2] \qquad \text{(eq. 1.1)}$$

where k_{aq} is 2 x 10^6 $M^{-2}s^{-1}$. The autoxidation rate law is second order with respect to [NO], so the reaction rate is dependent on the square of the concentration of NO. To illustrate this point, in water the half-life of 2 mM NO is < 1s, where the half-life of 5 nM NO is 70 h.[15]

A major sink for NO *in vivo* is reaction with oxyhemoglobin to form methemoglobin and nitrate; it can also form nitrosylhemoglobin.[15, 18] NO reacts with superoxide anion radical to form the powerful oxidant peroxynitrite ($ONOO^-$), at diffusion limited rates.[15] Peroxynitrite is responsible for many of the deleterious toxic effects of NO.

As a result of these reactive pathways, monitoring the concentration of NO is a great challenge. Often methods rely on degradation products such as N_2O_3, which is produced from reaction of NO with oxygen. Other methods measure nitrate, the product of the reaction of NO and oxyhemoglobin, and nitrite, produced by various mechanisms. These methods then purport to relate those concentrations to that of NO, which in some cases may not be accurate. Also there can be an equilibrium shift in the degradation

products of NO based on cellular conditions, such as hypoxia, where there is insufficient oxygen present. Under these conditions, oxidation products are not the ideal monitoring species. Another situation where correlation to degradation products does not always hold is the quantification of nitrites and nitrates, because of their dietary consumption, which affect their concentrations *in vivo*. These species concentrations can be unreliable unless dietary restriction is enforced. Therefore, there is a need for simple, direct detection for NO quantification, not its degradation products.

1.a.3. Concentration of nitric oxide in vivo

The concentration *in vivo* is very important because the difference between physiological concentrations and pathological ones can be only 1 or 2 orders of magnitude.[15] The reactivity of NO leads to difficulty in measuring the actual concentration *in vivo*. Another complicating factor for the quantification of NO is its fleeting nature, with a half-life on the order of seconds.[16] It's electrochemistry makes it subject to interference from other biological compounds. Even though NO has been known as EDRF since 1987, to this day the debate continues as to its actual concentration in cells, tissues, organs, etc. Once thought to be micromolar, the concentration of NO is now presumed to be low nanomolar or less, under normal physiological conditions, and this value is still debated. However, in pathological circumstances the concentration can be much higher, especially in sepsis, a condition characterized by systemic inflammation. The range is purported to be up to micromolar under these conditions.[16] Many of the original experiments predicting high concentrations of NO were largely performed by

electrochemical sensors. More recent evidence has proven this is not the case except for NO release during immunological response from macrophages. The general consensus is that NO concentration is likely in the picomolar to micromolar range overall and for most physiological processes is likely to be in the ~100 pM to ~5 nM range, although the prevailing dogma is that it is low nanomolar.[16, 19, 20] Thus, there is still much too learn about the concentration of NO *in vivo*.

1.b. Nitric oxide donors

NO is a gas at room temperature and pressure and solutions may be purged with gaseous NO to saturation of 2 mM. However, the gas is toxic at high concentrations, and NO begins to decompose rapidly in solution. Therefore researchers such as Keefer *et. al.* have developed NO donor compounds to release NO in solution under more controllable conditions. One of the most commonly employed NO donors is DEA/NO, which was used in this work. DEA/NO releases 1.5 molar equivalent NO per mole DEA/NO,[21, 22] but can release as much as 1.8 molar equivalent NO per mole DEA/NO. The theoretical 2 moles of NO per mole of DEA/NO is never realized. The reaction of DEA/NO to form NO is shown below.[23]

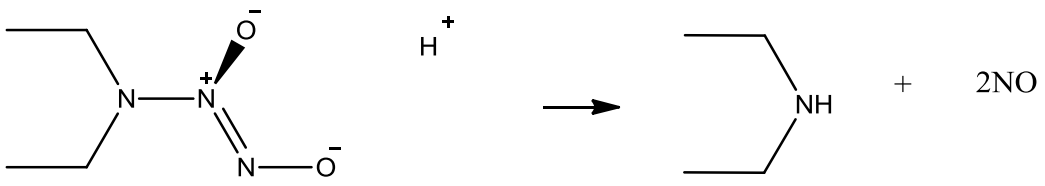

The above reaction is pH and temperature dependent with a pseudo first order rate. The observed rate constant at pH 8.00 is 0.00215 s^{-1} and at pH 5.16 it is 0.568 s^{-1}, both at 37 ^{o}C.[23] Thus the reaction occurs extremely rapidly at low pH. The half-life ranges from 2 min at 37 ^{o}C to 16 min at 22-25^{o}C, at pH 7.4.[22] DEA/NO kept on ice dissolved in 10 mM NaOH is stable for 24 hours. These properties of DEA/NO make it a useful NO donor.

1.c. Nitric oxide detection

The quantification of NO is important to understanding its role in physiology and pathology. The measurement of NO is particularly challenging due to its reactivity and short half-life. Many techniques have been developed to address the challenges of nitric oxide detection. Among these are electrochemical,[24] fluorescent,[25] chemiluminescent,[26] and absorbance spectroscopy,[27] and have been recently reviewed.[16] The detection limits of the techniques vary substantially as do the practicality of the methods. Many physiological studies quantify degradation products of nitric oxide such as nitrite and nitrate which are then correlated to nitric oxide.[*e.g.* 28-30] This can be problematic because nitrite and nitrate are consumed in the diet and drinking water in large amounts.[31, 32]

Likewise, many cellular studies use fluorescent probes that actually detect a degradation product of NO, N_2O_3. This can be problematic during hypoxic states when the degradation pathway to N_2O_3 is affected due to a lack of oxygen.

An optimal sensor would measure NO directly and selectively, have a large dynamic range, a low detection limit and high temporal resolution. For intracellular measurements, high spatial resolution would also be beneficial.

1.c.1. Griess assay

The Griess assay is an absorbance assay widely employed for NO detection, and was first developed in 1864 by Peter Griess.[33] It is a very commonly employed technique typically for *in vitro* analysis, and is amenable to a variety of sample types. While the Griess assay actually quantifies nitrite, it can also quantify nitrate with the use of the reductant Vanadium (III) chloride to reduce nitrate to nitrite.[16, 34] In the Griess assay, nitrite reacts with sulfaniliamide, which then reacts with *N*-(1-naphthyl)ethylenediamine forming an azo dye, and is quantified by the concentration of dye ($\lambda_{max} \sim 540$).[16] The limit of detection (LOD) of the Griess assay is 0.5 μM.[35] This detection limit is rather high and the method is best suited for batch monitoring. It is a standard assay but limited because basal levels of nitrite and/or nitrate must be determined in order to attribute changes in concentration to NO in physiological studies, or subjects should be placed on a low nitrate diet. The Griess assay requires an oxidized derivative, NO_2^-, thus it is not useful in hypoxic cellular conditions, where oxygen levels are low and NO degradation pathways change.[36]

1.c.2. Oxyhemoglobin assay

Like the Griess assay the oxyhemoglobin assay is a common absorbance based method of NO analysis and is typically used for *in vitro* analysis. The use of oxyhemoglobin as an assay for NO was first described by Haussmann *et. al.* in 1985.[37] In this method, methemoglobin is reduced to its ferrous state and allowed to bind oxygen, yielding oxyhemoglobin. It is then incubated with the NO containing sample where the oxyhemoglobin is subsequently oxidized by NO, creating methemoglobin (ferric heme) and nitrate:[27]

$$Hb(Fe^{2+})O_2 + NO \rightarrow MetHb(Fe^{3+}) + NO_3^-$$

The reaction is followed by monitoring the characteristic absorbance Soret maxima of oxyhemoglobin and methemoglobin at 400 nm and 417 nm, respectively. The difference between isosbestic point at 411 nm and the decrease at 400 nm is plotted against concentration to generate a calibration curve. Strictly speaking, the oxyhemoglobin method is not specific to NO, but rather to the generation of ferric heme. This method is therefore sensitive to reducing or oxidizing interferents[38] and to samples containing other hemoproteins.[27] It is time consuming to reduce the hemoglobin and purify immediately prior to analysis. The oxyhemoglobin assay has a limit of detection (LOD) of 2.8 nM.[27]

1.c.3. Electrochemical methods

Electrodes are often capable of real time monitoring and can be miniaturized for *in situ* analysis, making them potentially well suited for biological analysis and provides for a popular approach to detection. Electrochemical NO electrodes can be very sensitive and are widely used, but are limited by common biological interferents such as ascorbate, nitrite, uric acid, dopamine and carbon monoxide.[16] To reduce the susceptibility of interfering species, electrodes are often coated with semi-permeable membranes or electrocatalytic membranes to lower to oxidation potential and to exclude interferents.[16] Most electrochemical sensors for NO function by oxidizing NO to NO_2^-, rather than reduction from NO to NO^-, due to interference from the reduction of O_2 to O_2^-.[16] The oxidation potential is actually quite high, +0.7-0.9 V versus Ag/AgCl,[39] which leaves it susceptible to electrochemical interferences by nitrite, dopamine, ascorbate, uric acid and carbon monoxide.[16]

Nickel porphyrin-based electrodes have also been developed.[40] Although adequate limits of detection were reported, e.g. 10 nM,[41] the initial versions had a propensity to become fouled with biological molecules.[14, 40] They are also plagued by biological interferents such as nitrite, catecholamines and ascorbate.[40]

There is a long history of NO sensitive electrodes based on semi-permeable membranes, such as those based on a chloroprene rubber gas-permeable membrane.[42] This sensor had a linear response from 1 to 3 μM.[42] More recently work by Shoenfisch *et. al.* utilized xerogel-based permselective membranes using amino and alkyl-alkoxysilane xerogel precursors and Nafion® as a method for selectivity.[39] This sensor had a detection limit of 25 nM NO.[39] This was then improved upon by using

fluoroalkoxysilane as a xerogel precursor, which had a limit of detection of 83 pM.[43] CO is an interferent to this electrode design, producing ~5% of the electrochemical signal that is produced by NO, largely due to its small, non-polar nature and similar oxidation potential.[43] This is a problem because CO is thought to be in the low nanomolar range *in vivo*,[44] but could potentially be higher.[45]

A novel electrode was made from hemoglobin encased in a sodium montmorillonite on a pyrolytic graphite surface.[46] The electrode function is based on the attenuation of the reduction potential of O_2 by NO.[46] This sensor achieved a detection limit of 20 pM, but was insensitive to small changes of NO concentration.[46] It also had significant interferences from dopamine, uric acid and epinephrine.[46]

A major shortcoming of NO electrodes is their susceptibility to interferents such as ascorbate, uric acid, dopamine, nitrite and especially carbon monoxide which is typically overlooked in most publications.[16] NO electrodes were also the subject of an in-depth review by Hall and Garthwaite highlighting the dramatic and irreconcilably large range of NO concentrations reported in the literature.[19] This study illustrates the possible role of cross-reactivity of NO electrodes.[19]

1.c.4. Chemiluminescence detection of nitric oxide

Along with the absorbance methods of oxyhemoglobin and the Griess assay, electrochemical methods are the most common techniques used to quantify NO in biological studies. These are proven techniques but they don't directly quantify NO. Rather, they rely on degradation products or rely on redox chemistry that is inherently

nonspecific and subject to interferents. The Griess assay has been used for more than 100 years with much success. It can be used in a variety of matrices, which makes it very versatile, but has a limit of detection of only 0.5 μM.[35] The oxyhemoglobin method has a good detection limit of 2.8 nM,[27] requires time consuming protein reduction and purification just prior to analysis, and is subject to redox interferents.[38] Electrochemical methods can be very sensitive and have been widely used for physiological studies, but are subject to common biological interferents.

Chemiluminescence can be used to measure NO, nitrite or nitrate and can have a very low detection limit. There are two methods generally used for the chemiluminescent detection of NO. The first is a reaction between NO and O_3 forming an excited state NO_2*, which emits a photon upon collision with a carrier gas molecule (e.g. N_2) and relaxing to the ground state:[16, 47]

$$NO + O_3 \rightarrow NO_2^* + O_2,$$

$$NO_2^* \rightarrow NO_2 + h\nu$$

In this experiment, NO is purged from solution by a carrier gas and flowed into a reaction cell with a photomultiplier tube, which is not appropriate for many biological samples.[16] The detection limit is based on sample volume, but is in the nanomolar to picomolar range.[16]

The other method of chemiluminescent detection is the reaction of NO with H_2O_2 to form $ONOO^-$, which then reacts with luminol, creating chemiluminescence.[48] This

method has an impressive limit of detection of 100 fM, but only has a linear response to 1 nM.[48] Chemiluminescence analyzers are commercially available and are commonly employed to quantify NO. Both types of chemiluminescence detection have very low detection limits, and large dynamic ranges. A major drawback of the ozone method is that it is unsuited for many biological applications.[16, 47]

1.c.5. Fluorescence based methods

Thus far we have considered absorbance based methods that are simple and generally available, but often suffer from a high limit of detection, poor temporal resolution and indirect NO quantification and/or cumbersome protein purification. Electrochemical methods allow for excellent detection limits in some cases but are plagued by interfering species.[16] Chemiluminescence detection can have outstanding detection limits and in some methods direct detection of NO, but is not appropriate for all biological applications.[16, 47]

Fluorescent probes are particularly useful for measuring intracellular levels of NO *in vitro* due to their high spatiotemporal resolution. However, many of the common fluorescent probes measure N_2O_3, a degradation product of NO.[16] N_2O_3 occurs from the reaction of NO with O_2. Those fluorophores, such as 3-Diaminonaphthalene (DAN), detect N_2O_3, and cannot be used to measure NO in real time because NO must degrade prior to detection.[16] However, this means that the fluorophore is not interfering with the physiological role of NO.[49] DAN, like many NO sensitive fluorophores, increase fluorescence upon reaction with an NO degradation product.[16] The use of DAN is

limited by its cytotoxicity, poor solubility, small extinction coefficient and the autofluorescence caused by excitation in the UV.[49]

The fluorescein derivatives diaminofluorosceins (DAFs) have been used extensively for cellular NO imaging, due to their large extinction coefficient and favorable excitation wavelength (similar to fluorescein).[49] DAFs react with N_2O_3, which causes an increase in fluorescence.[49] The limit of detection can be as low as 5 nM (DAF-2).[49] Although they are susceptible to common interfering species such as NO_2^-, NO_3^- H_2O_2 and $ONOO^-$, and the fluorophores are pH dependent.[16, 49] This pH dependence can pose a problem when applied to biologically relevant samples where intracellular pH changes slightly, disallowing detection of small changes in NO concentration.[49] DAF-2 DA, a diacetate-derivatized form of DAF-2, allows for cellular uptake of the fluorophore, where it remains trapped due to hydrolysis of the acetate bonds to an impermeable form.[16] Unfortunately, DAFs have been shown to react with ascorbic acid and dehydroascorbic acid yielding products with similar optical properties as the N_2O_3 reaction product.[50, 51] They are not useful in hypoxic cellular conditions due to the fact that these probes require oxidized derivatives.[36] The fluorescence of DAF probes is also strongly influenced by the concentration of divalent metal cations, especially calcium.[36, 52]

More recently, the Lippard research group has synthesized Cu(II)-fluorescein probes that react directly with NO.[25, 36, 53-55] These fluorophores are based on fluorescein with a moiety that binds Cu(II).[25, 53, 54] Cu(II) is reduced to Cu(I), the remaining fluorophore scaffold is *N*-nitrosated and the metal dissociates from the scaffold,

increasing fluorescence by reducing the quenching induced by Cu(II).[25, 53, 54] These fluorophores have a limit of detection limit of 5 nM (FL1 version of the probe).[55] However, the response of FL1 to $ONOO^-$ is ~15% of the signal from NO.[54] To increase the dynamic range, the FL2 series was synthesized.[36, 54] The temporal response is ~20 min for full fluorescent signal for FL2 and the cell trapped version FL2A.[54] There was also interference from nitrite, which produced ~6% of the fluorescent signal and significant interference from $ONOO^-$ and H_2O_2, producing ~15% of the signal achieved for FL2A.[53, 54]

1.c.5.a. Genetically encoded fluorescence based methods

There have been several attempts to use molecular biological probes incorporated into the genome of a cell line for NO detection.[56, 57] Sato *et. al.* (2005) developed a method of NO detection by transfecting vascular endothelial cells with a fluorescent cGMP binding domain based on cGMP protein dependent kinase along with cyan and yellow fluorescent protein (CGY) on sGC α and β domains.[56] The cGMP produced by sGC bound to the CGY domain yielded a FRET signal between the two fluorescent proteins, allowing a limit of detection of 100 pM.[56] Since cGMP is an important secondary messenger, and is produced as an amplification step, there is the potential for biological effects on the sensor, although the authors claim it is immediately broken down by phosphodiesterases.[56] This sensor is also reported to be reversible.[56] They conclude that vascular endothelial cell produce a basal level of ~1 nM in serum supplemented media, with no sheer stress.[56]

Sato *et. al.* (2006) demonstrated the use of a detector cell line based method on their sensor described above.[58] In this detection scheme the authors use cells of a pig kidney cell line with the incorporated sGC cGMP probe in close proximity to cells of interest, in their case hippocampal neuronal cells.[58] This method yielded a limit of detection of 20 pM.

Most NO detection methods described thus far typically do not measure NO directly, with a few exceptions. The genetically encoded methods described herein present an interesting approach on NO detection by incorporating the NO reporter into the genome of a cell line. Some of these approaches take advantage of unique specific interactions of NO and its primary endogenous receptor soluble guanylate cyclase, which yields unequivocal selectivity. These systems are well suited to work on cell systems, but would not immediately translate to other samples. They generally have very low detection limits because they are based on fluorescent proteins. Although these methods offer advantages, they are very specific for the application and require significant effort to alter the molecular biology of each different system it is employed in to incorporate the NO reporter.

1.d. Dietary nitrites and nitrates

The most commonly employed techniques in physiological studies measure nitrite and/or nitrate, using the Griess assay or chemiluminescence with reduction of nitrate to nitrite. The direct correlation to nitric oxide is often assumed. However, these studies typically do not take into account the nitrite and nitrate consumed in the diet, unless

carefully designed. The EPA allows for drinking water to contain 0.161 mM nitrate, and this value is often sometimes exceeded in ground water. Vegetables contain large amounts of nitrates as well, especially leafy greens. To illustrate this point, a plate of spinach can contain more nitrate than the nitrate produced by all forms of nitric oxide synthase combined *in vivo*.[32] More careful studies take this into account and hospitalize patients to feed them a low nitrate diet and distilled water.[59, 60] However, it would be ideal to measure nitric oxide directly.

1.e. Nitrophorins

The focus of the sensor developed herein is based on a nitrophorin (NP) protein. The nitrophorins are a group of 7 proteins from a blood-feeding insect, *Rhodnius prolixus*, known as the "kissing bug." There is also another form of nitrophorin found from *Cimex lectularius*, the bedbug. Nitrophorin's function is to aid in increasing the blood meal of the insect through the transport and release of NO by causing vasodilation and platelet inhibition. There are seven nitrophorins from the *Rhodnius prolixus* species, NP 1-7, the numbers correspond to their respective abundance (with 1 being the most abundant). NP7 was only recently discovered in the cDNA library of the salivary gland of *Rhodnius prolixus*.[61, 62] *Rhodnius* nitrophorins are all structurally similar, ~20 kDa proteins that contain an 8 stranded β-barrel, known as a lipocalin fold, which binds a heme on one end through a proximal histidine. The heme in nitrophorins is ruffled and non-planar, which is thought to stabilize the ferric form of the iron center. A ferric heme is best for transport of NO because the ferrous heme containing proteins have binding

constants in the femtomolar to nanomolar range. If this were the case with nitrophorins, they would not be effective in releasing NO into the victim.

Nitrophorins are unique among ferric proteins for their strong affinity to NO at low pH, with the dissociation constant (K_d) in the mid to low nanomolar range at pH 5. Binding is greatly reduced when the pH is elevated to 7.5, where the K_d is typically in the micromolar range. This supports the main function of the nitrophorins, which is to release NO at the site of feeding in the host, thereby leading to vasodilation and increasing blood flow to the insect. Another function of the nitrophorins is to bind histamine released by mast cells in response to the insect bite. There is a concomitant rise in the binding of histamine by nitrophorins with increasing pH, as their affinity for NO decreases. This allows the protein to have a dual function. As it releases NO into the wound site, it binds histamine, thereby decreasing the tissue's response to histamine, which includes inflammation and immune response, enabling *Rhodnius prolixus* to escape detection. NP2 also functions as an anticoagulant, preventing blood clotting at the site of the wound. NP7 binds to phosphotidylserine moieties on the surface of immune cells, interfering with coagulation. These actions of the NPs allow the animal to feed for extended periods of time without detection.

The *Rhodnius prolixus* species is found in the Americas but is most common in South America. The disease vector *Trypanosoma cruzi* is spread through *Rhodnius prolixus*, in the feces of the insect, which causes Chagas' disease. When the victim scratches the wound, the vector enters the new host, where it causes cardiac disease. Some 16-18 million people are chronically infected with Chagas' disease. The cardiac

output of those infected with the disease is 25% less than normal, and is a serious health concern.

1.e.1. Nitrophorin 4

NP4 is an interesting example of the nitrophorins. The structure of NP4 has been determined by the Montfort group to ultrahigh resolution, and in the presence and absence of NO, histamine and related ligands (Figure 1.3). These structures reveal that two loops, A-B and G-H, are flexible and close down over the opening of the β-barrel upon NO binding, forming a hydrophobic pocket that entraps the NO molecule within the protein.[63] NP4 is known to bind NO and histamine. These ligands have distinguishing spectral characteristics that make them distinctly identifiable. NP4 has a Soret λ_{max} of 404 nm when unligated, which shifts to 419 nm when ligated with NO (both at pH 8.0).[64] The NP4-histamine complex has a λ_{max} of 413 nm (at pH 8.0).[65] The calculated isoelectric point of NP4 is 6.35.[62]

The association rate of NO binding to NP4 is fast, with a rate constant of 2.5 $\mu M^{-1}s^{-1}$, at pH 5.0, the rate constant is second order with respect to NO.[66] There is also a slow secondary rate that is first order with respect to NO with a rate constant of 33 s^{-1}.[66] The rate NO dissociation from NP4 is pH dependent and is also biphasic.[66] The initial steps are slow, having rate constants of 0.15 s^{-1} and 0.02 s^{-1}, which is followed by a faster step with a rate constant of 21 s^{-1}, at pH 5.0.[66] The pH dependence of the equilibrium dissociation constant of NP4, is the result of an increase in the rate constants of the slow phases of dissociation to 1.8 s^{-1} and 0.6 s^{-1}, respectively, at pH 8.0.[66]

Figure 1.3. Structure of NP4, heme, histidine 59, and NO are depicted in red. The flexible loops A-B, and G-H are shown in gold. Reprinted from reference 64 with permission. Copyright 2005 American Chemical Society.

1.f. Protein Adsorption to Surfaces

The NO optical sensor described herein makes use of NP4 adsorbed onto a glass surface. There is a long history of adsorption of proteins to surfaces for use as sensors and affinity probes. Conversely and more commonly, the intentional minimization of protein adsorption to surfaces is desired for materials such as laboratory ware and implantable devices. The intermolecular interactions dictating protein adsorption to surfaces involve electrostatic, hydrogen bonding, van der Waals forces and hydrophobic effects.[67] This involves both the properties of the surface and those of the protein. Although it has been studied extensively it is still difficult to predict and thus is an empirical science. The factors that influence protein adsorption to a given surface are buffer type, pH, ionic strength, temperature and pI of the protein.[67, 68]

It would be intuitive to think proteins adsorb best to oppositely charged surfaces. For example, a positively charged protein binding to a negatively charged surface. This is true to some extent, and adsorption rates are high when there is an electrostatic attraction, but proteins adsorb to the surface maximally when the pH of the buffer is equal to the pI of the protein.[67, 68] Protein-protein repulsion is minimized when the pH of the buffer equals the pI of the protein.[68]

Protein adsorption to surfaces is led by enthalpic contributions from favorable protein-surface interactions, in addition to entropic gains from the release of solvent molecules and ions adsorbed to the surface and the protein.[67] Electrostatic contributions dominate if the protein and the surface are oppositely charged. Typically, if there is no

net overall charge on either the surface or the protein then the interaction is dictated by hydrogen bonding. The functional groups participating in hydrogen bonding are carbonyl groups, vicinal silanol groups, imido groups, individual silanols and amino groups.[67] The initial adsorption events of the protein adsorbing out of solution occur within micro-to-milliseconds.[69] This can be followed by multipoint adhesion via conformational changes in the protein within 50-200 milliseconds.[67] Increasing temperature generally leads to increased adsorption.[68]

Ionic strength may also affect protein adsorption. Increasing ionic strength enhances the adsorption of proteins to like-charged surfaces, and conversely, decreases adsorption to oppositely charged surfaces.[68] These effects are due to the charge shielding nature of additional ions in solution. Ionic shielding of charges can also increase protein packing density, by limiting protein-protein repulsion, but can also limit cooperative effects of protein binding.[68] It is interesting to note that larger proteins tend to bind stronger to surfaces than smaller ones simply due to a larger contact area.

Studies of protein adsorption demonstrate that maximal binding occurs on hydrophobic surfaces.[67, 70] This is thought to be due in part to conformational rearrangements in the protein induced by the surface.[70] It is now widely accepted that proteins undergo conformational changes when adsorbed to surfaces.[68] Enzymatic activity can be reduced upon adsorption or remain similar to activity in solution.[68] Loss of activity can be due to conformational changes and/or improper surface orientations. Adsorption can also induce protein unfolding and denaturation. The orientation of the protein on a surface can lead to the binding site being sterically hindered, preventing

activity, or exposed to the solution, where the chances of retaining ligand binding or activity are increased.

The adsorption of a protein on a given surface must be investigated empirically to determine appropriate conditions under which non-specific binding to the surface will occur with minimal loss of activity. Activity or ligand binding must also be interrogated to identify if the protein has been greatly perturbed or inhibited due to the nature of adsorption.

1.f.1. The surface chemistry of glass

Glass can be a very useful surface for protein adsorption, particularly when studying activity through changes in absorbance. Glass is optically transparent into the ultraviolet wavelengths. Glass is also very flat and can be used as an optical waveguide for measurements at the surface. The surface of glass has been well characterized and has silanol groups at a density of 2.5/nm^2.[71] The silanol groups are acidic with pK_a values that ranges from 5-7.[71-73] The pH of the surface depends on the treatment and cleaning method of the glass. It has been shown that treatment with acid, base or plasma creates a hydrophilic surface by increasing silanol concentration. These treatments convert siloxane bonds into silanol groups. This is an advantage for protein adsorption because proteins can use these silanols for hydrogen bonding sites during adsorption events.

1.g. Attenuated total reflectance spectroscopy

Attenuated total reflectance (ATR) is a technique that has been used to study protein adsorption.[74, 75] ATR is based on total internal reflection, which occurs when light is coupled into a medium of lower refractive index from a medium of higher refractive index at an angle equal to or greater than the critical angle. This property of light coupling is described in Snell's Law:

$$n_1 \sin\theta = n_2 \sin\varphi \qquad \text{(eq. 1.2)}$$

Where $n_1 > n_2$, and $\varphi = 90^o$, θ is the critical angle. A beam of light at an angle greater than or equal to the critical angle will undergo total internal reflection. A part of this light propagates down the waveguide and will penetrate outside of the waveguide creating an evanescent field and decay exponentially. The depth of penetration (D_p), assuming a thin film and two phase approximation, is described by the equation:[76]

$$D_p = (\lambda/4\pi n_2)\,[\sin^2\theta - (n_1 - n_2)^2]^{-1/2} \qquad \text{(eq. 1.3)}$$

where θ is the internal reflection angle. This type of spectroscopy is surface sensitive due to the exponential decay of the evanescent field at the interface between the two media. As seen in equation 1.2, there is a wavelength dependence to the depth of penetration as well as a dependence on the refractive index of the materials, n_1 and n_2.

1.h. Overview of experiments

The research described herein involves the study of protein on surfaces, using three distinct approaches: (i) a novel sensor for nitric oxide, (ii) imaging of a fragment of soluble guanylate cyclase in an attempt to obtain a three-dimensional molecular envelope and (iii) the use of silica colloidal crystals for use as protein microarrays.

A nitric oxide sensor was developed using NP4 and an attenuated total reflectance waveguide platform (Chapter 2). NP4 binds nitric oxide tightly at low pH (pH ~5). There is a spectral shift between the unligated (λ_{max} ~404 nm) and the NO bound forms (λ_{max} ~416 nm) of NP4 on the sensor surface. This shift in the Soret band was the basis of the sensor. The mutant NP4 was intended to have a depleted pH dependence as compared to wild type, but this aspect was not entirely realized. Nevertheless, the protein proved useful for the purpose of an NO sensor. Using the ATR technique, spectra were generated from protein bound to the surface. This sensor allowed for the direct detection of NO with high specificity, low detection limit, and with good temporal resolution. This sensor was also shown to be reusable.

Fragments of the endogenous nitric oxide receptor soluble guanylate cyclase (sGC) were imaged in an attempt to produce a three-dimentional reconstruction using transmission electron microscopy (TEM) (chapter 3). sGC converts guanosine triphosphate to cyclic guanosine monophosphate (cGMP). Upon binding NO the activity of sGC increases activity by nearly 200 fold over basal levels. cGMP is involved in many downstream signaling processes including vasodilatation. sGC is an ~150 kDa heterodimer of two similar subunits α and β. There is a heme group on the β subunit, which binds NO. Aside from the heme functionality, the two subunits are very similar.

They both contain an N-terminal H-NOX (Heme-Nitric oxide/Oxygen) domain, PAS domain, coiled coil region and a catalytic domain, based on homology models. Each of these domains has analogs in other proteins but a three-dimensional structure of sGC remains unknown. Our lab has developed an *E. coli* expression system for the insect *Manduca sexta* variant of sGC, known as msGC. These constructs are ~90 kDa and lack the α and β cyclase domains but retain the HNOX, PAS and coiled coil regions on α and β subunits. It has been shown that these constructs retain their affinity for NO, CO and the synthetic ligand YC-1.[13, 77] By imaging the protein it was thought to be possible to reconstruct the 3D shape from the 2D projections. We have imaged msGC fragments using electron microscopy to begin understanding overall shape and domain arrangement of the molecule.

The final project described in chapter 4 uses silica colloidal crystals as substrates for microarrays. As a result of using silica colloidal crystals sintered to quartz slides the surface area is enhanced, thus increasing the capacity for protein binding to the surface. Four different silica colloid particle sizes were spin coated, using novel procedures. These were then used as protein microarrays for a BSA/ anti-BSA assay to illustrate the advantage of this platform. The particle sizes were compared for their increased fluorescence versus a plain quartz slide in order to optimize the particle size for the greatest enhancement. Arrays with smaller particle sizes give more surface area per unit volume based on their geometry, but there exists a point when the particle sizes become too small and steric hindrance becomes a limiting factor. This is because the proteins can no longer enter the pores created by the colloids in the crystals and thus cannot take

advantage of the increased surface area The optimal silica colloid size for microarray applications were investigated.

CHAPTER 2

DEVELOPMENT OF A NOVEL NITRIC OXIDE SENSOR USING NITROPHORIN 4 ON AN ATTENUATED TOTAL REFLECTANCE PLATFORM

2.a. Introduction

Nitric oxide (NO) is an important molecule in physiology involved in numerous biological roles including cardiovascular,[4] central nervous system[5] and immune response.[7] NO is synthesized *in vivo* by nitric oxide synthases,[11] and has recently been shown to also be formed *in vivo* by the reduction of nitrite.[12] NO has been implicated in numerous pathological conditions such as cancer,[8] sepsis,[9] and arthritis.[10] Advancement of our understanding of NO in biology is limited due, in part, to the lack of direct NO detection methods. Evaluation of treatments and insight into NO's role in disease progression are just a few areas that would be greatly improved with increased knowledge of NO concentrations *in vivo*.

Many techniques have been developed to address the challenges of nitric oxide detection. Among these are electrochemical,[24] fluorescent,[25] chemiluminescent,[26] and absorbance spectroscopy approaches,[27] all of which have been recently reviewed.[16] The detection limits of the techniques vary substantially as do the practicality of the methods. Many physiological studies quantify degradation products of nitric oxide such as nitrite and nitrate, which are then correlated to nitric oxide.[*e.g.* 28-30] This can be problematic because nitrite and nitrate are consumed in the diet and drinking water in large amounts, and physiological studies must be carefully controlled.[31, 32]

The oxyhemoglobin assay is a common method of analysis for NO but is sensitive to reducing or oxidizing interferents[38] and to samples containing other hemoproteins.[27] It is also time consuming to chemically reduce the hemoglobin and remove the reductant immediately prior to analysis. The detection of NO in organs and blood is typically performed with a Griess assay, chemiluminescence analyzer or more commonly, electrochemically. The Griess assay actually detects nitrite, and nitrate if it is first reduced to nitrite.[16] The limit of detection (LOD) of the Griess assay is 0.5 μM.[35] Chemiluminescence can be used to measure NO, nitrite or nitrate but is not applicable to all biological experiments.[16, 47] Electrochemical NO electrodes can be very sensitive but are limited by common biological interferents such as ascorbate, nitrite, uric acid, dopamine and carbon monoxide.[16] Fluorescent probes are particularly useful for measuring intracellular levels of NO due to their high spatiotemporal resolution. However, many of the common fluorescent probes measure N_2O_3, a degradation product of NO.[16] All of the above methods are proven techniques and are useful in their own right, but a direct NO sensor with a low limit of detection would be immediately useful.

Attenuated total internal reflectance has been used to study protein adsorption;[74, 75] a schematic can be seen in Figure 2.1. Herein, we describe the use of soluble guanylate cyclase (sGC) from *Manduca sexta* and nitrophorin 4 (NP4) from *Rhodnius prolixus* as biosensors for NO.

sGC is as an endogenous receptor for NO and upon NO binding, sGC increases its rate of cGMP production. sGC is a 150 kDa protein that contains a heme moiety that has a Soret band at 433 nm, which shifts to 400 nm upon NO binding (Figure 2.2, data

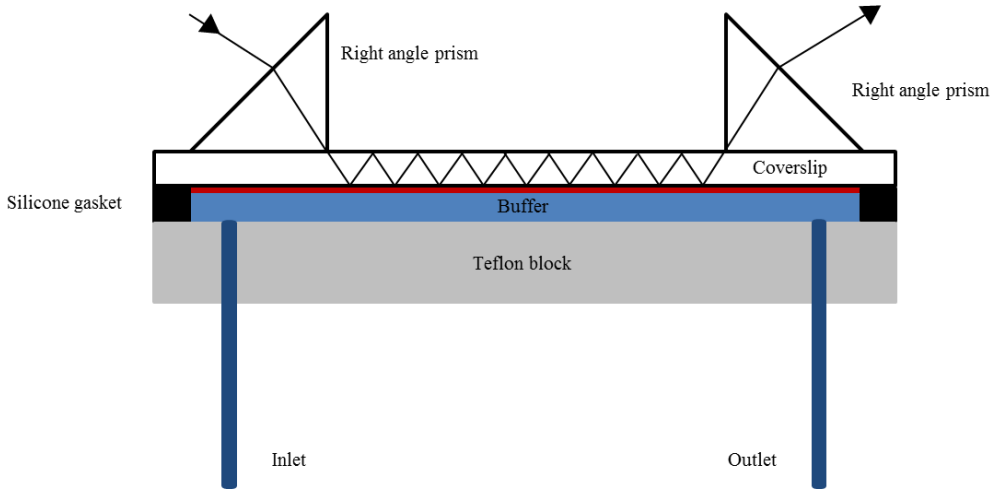

Figure 2.1. Cross-section schematic of ATR flow cell. Silicone gasket is in black, adsorbed protein layer in red. See text for details.

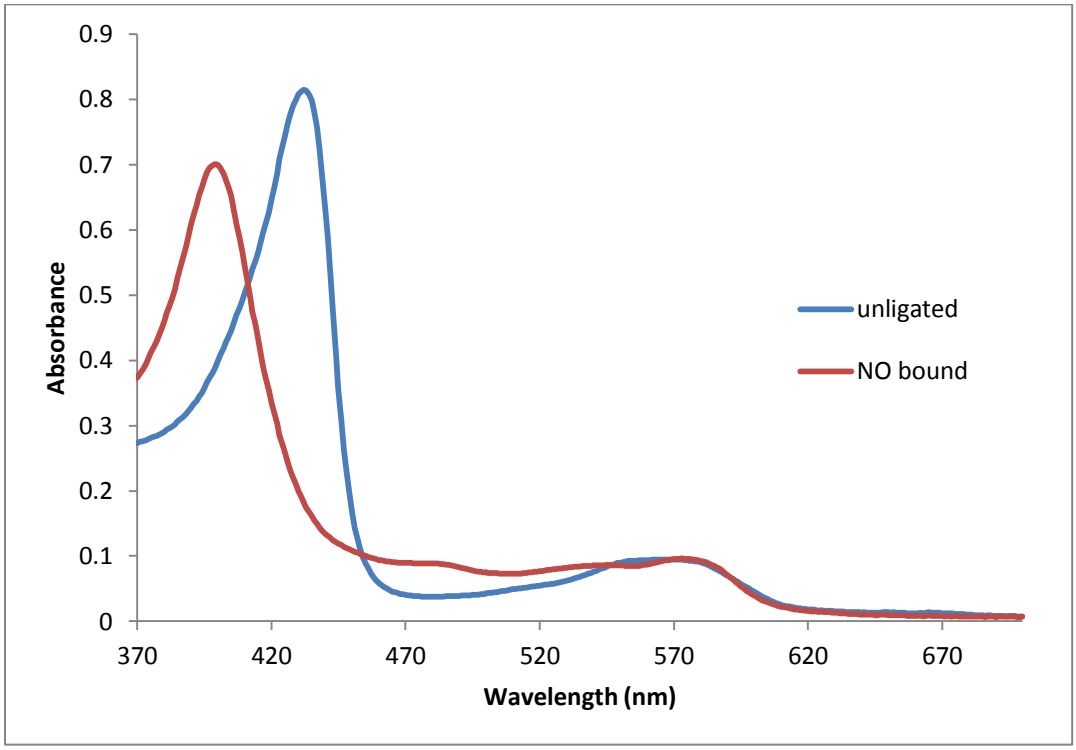

Figure 2.2. Solution spectra of sGC NT-13 unligated and with NO bound in 50 mM sodium phosphate, pH 7.4, and 300 mM NaCl. Data provided by Aaron Issaian.

provided by Aaron Issaian).

Nitrophorin 4 (NP4) is an ~20 kDa protein that has an eight stranded β-barrel, which binds a *b*-type heme group through a proximal histidine residue.[78] Nitrophorins are unique among ferric proteins for their strong affinity to NO at low pH (~5). Nitrophorins are found naturally in bedbugs and kissing bugs where they are used to deliver NO to victims as a vasodilator during blood-feeding. The kissing bug nitrophorins then function to bind histamine at physiological pH (~7.5), which decreases inflammation and helps the insect avoid detection from its prey.[78] Solution spectra of NP4 unligated and with NO bound can be seen in Figure 2.3 (data provided by Aaron Issaian).

The sensors developed detect a shift in the λ_{max} between unligated and NO bound spectra, using ATR spectroscopy.

2.b. Materials and methods

2.b.1. Protein and DEA/NO preparation

NP4 was prepared by over expression in *E. coli* and refolding after isolation from inclusion bodies, as described previously.[65, 79] The following point mutations were incorporated: D30N, E32Q, D35N (herein referred to as NP4 NQN), by Aaron Issaian. sGC fragments were prepared as described by Fritz *et. al.*[80, 81] Briefly, heterodimeric fragments of *Manduca sexta* soluble guanylate cyclase, containing residues α 49-450 and β 1-380, were expressed in *E. coli* using the pET-Duet-1 plasmid. DEA/NO and Angeli's salt were gifts of Professor Katrina Miranda (University of Arizona). Each preparation

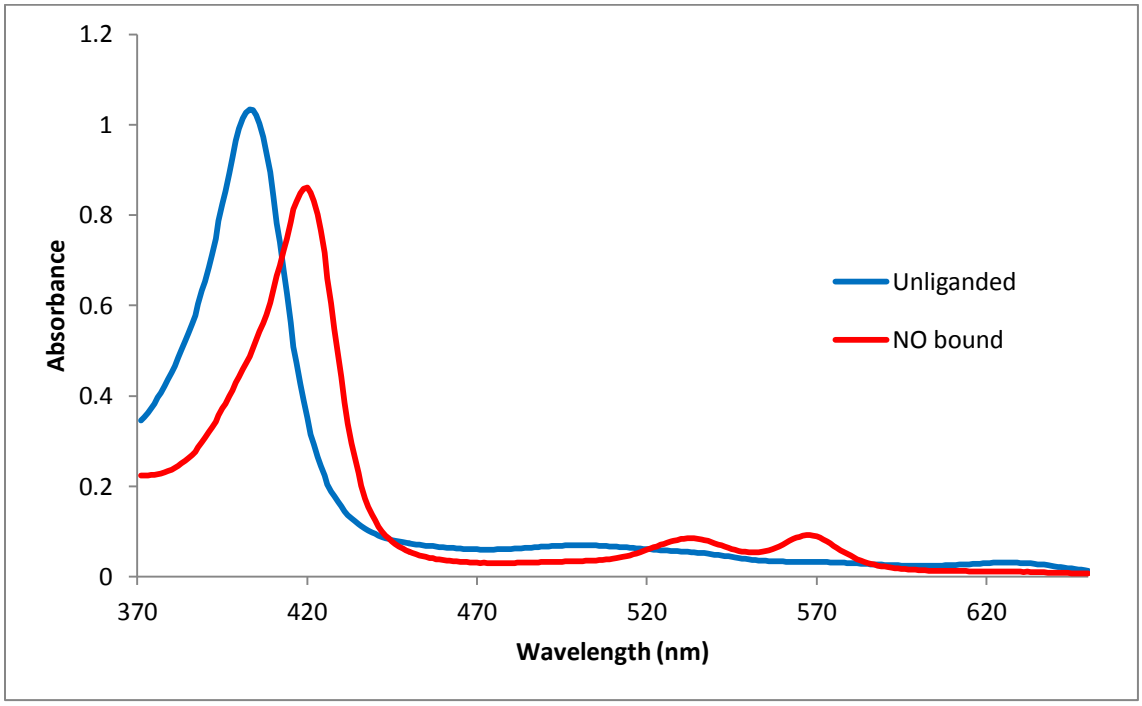

Figure 2.3 Solution absorbance spectra of NP4 NQN unligated and NO ligated in 20 mM Tris buffer, pH 7.5. Data provided by Aaron Issaian.

was quantified spectroscopically; each displayed an ε_{250} of 8 $mM^{-1}cm^{-1}$. Stock solutions were made in 10 mM NaOH at 100 times the desired concentrations and a final 1:100 dilution was made with buffer. All DEA/NO solutions were kept on ice until used. For data analysis it was assumed that 1.5 moles of NO were released per mole of DEA/NO.[20] There was a small increase of 0.17 pH units upon the addition of 100x DEA/NO to 5 mM buffer due to the 10 mM solvent of the DEA/NO solution. This small increase in pH was ignored in the reporting of the pH of the experiments.

2.b.2. Attenuated total reflectance spectroscopy

A custom attenuated total reflectance spectrometer is illustrated in Figure 2.1. Briefly, a white light source is coupled into a coverslip using a right angle prism. Light propagates down the coverslip, which acts as a waveguide. An evanescent wave of light enters the flow cell, and its intensity decays exponentially away from the surface of the coverslip, making it a highly surface sensitive technique. Protein bound to the surface is monitored with the incoming light and spectra are generated.

A 75 W xenon lamp (Newport Instruments) was used as a white light source. The light was focused into a fiber optic cable connected to a collimating lens followed by a polarizing lens. The ATR flow cell was secured onto a rotary stage with an xyz translational stage. The light was coupled into and out of a 3" x 1" glass coverslip #1 (Electron Microscopy Sciences) with 10 mm x 10 mm x 14.1 mm BK-7 glass right angle prisms (Edmund Optics). The out-coupled light was focused with a lens attached to a

fiber optic cable into a monochromator (Newport Instruments MS260i) and detected by a CCD camera (Andor iDus420A).

Coverslips were gently cleaned with cotton and diluted Alconox Liqui-Nox detergent and rinsed with Milli-Q purified water (18.2 MΩcm) water. They were then soaked in piranha (7:3 concentrated sulfuric acid: 30% hydrogen peroxide) for approximately one h (caution: piranha is extremely reactive). The coverslips were then rinsed with copious amounts of Milli-Q purified water and stored in Milli-Q purified water until use. The ATR flow cell was assembled with a coverslip, silicone gasket and a Teflon block with inlet and outlet tubing, and held together with an aluminum holder. The cell was mounted directly into the xyz translational stage. Solutions were injected into the flow cell via syringe.

Deaerated solutions were used unless otherwise noted and prepared by purging buffer with argon for 30 min followed by vacuum filtration. The ATR flow cell was equilibrated with buffer and dark and background spectra were then collected. ATR spectra were collected for the resulting NP4 NQN film in both TE and TM polarizations. The TM polarization data were used in all calculations and figures presented. Where indicated, spectra were averaged by acquiring multiple spectra and numerically averaging the absorbance values. Also where indicated a running average was performed on the spectra to smooth the data. This was performed by averaging five or ten pixels together in a running average. The baseline drifted during the course of the experiments. When the baseline was corrected, it was done so by using the minimum point of all spectra

collected and setting that to zero absorbance units. This was always in the far red of the spectrum around 725 nm, where there should be no absorption from the protein.

2.c. Results and discussion

2.c.1 Adsorption of sGC

Soluble guanylate cyclase (sGC) was used to construct an NO sensor using an attenuated total internal reflectance (ATR) waveguide platform. sGC was a natural choice due to the fact that it is the major receptor for NO *in vivo* (see chapter 3.a.),[13] and binds NO very strongly (femtomolar to picomolar range). Fragments of sGC were constructed in our laboratory to increase the yield and solubility as compared to the full length version of the protein. The full length protein is a heterodimer of two subunits, α_1 and β_1. The subunits are similar in that each contains H-NOX, PAS, coiled coil and catalytic domains, with a single heme group residing on the β_1 H-NOX domain. Construct NT-13 is a fragment of sGC that contains the HNOX, PAS and coiled coil domains of both α_1 and β_1 subunits, but lacks both cyclase domains. Therefore, it lacks catalytic activity but still binds NO through the heme moiety (see chapter 3.a. for more details of sGC and NT-13). NT-13 was adsorbed to a glass coverslip and probed as an NO sensor.

SGC was deposited in 10 mM sodium phosphate buffer (pH 7.3), which yielded adsorption to the surface (Figure 2.4). However, it was in very low abundance as indicated by the absorbance value of the soret band. While sGC has a high molar absorptivity, it will only be a good choice for ATR if sufficient protein can be adsorbed.

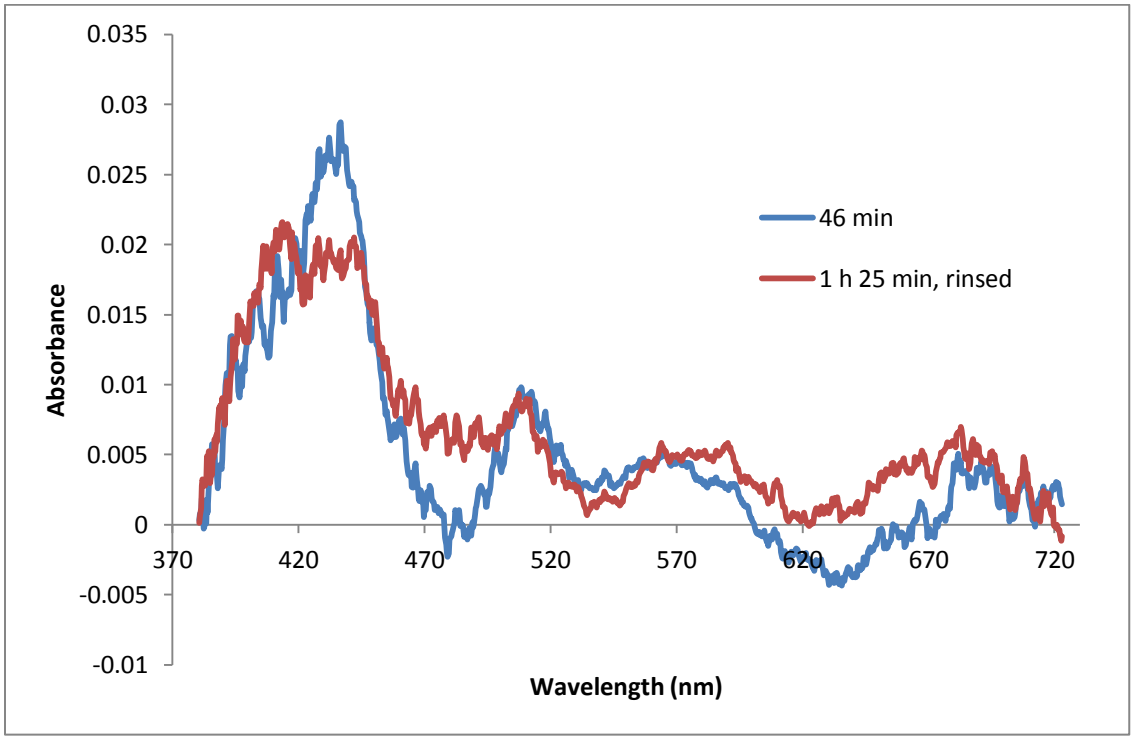

Figure 2.4. NT-13 (0.63 mg/mL) was adsorbed to a piranha cleaned 75 mm #1 coverslip. ATR absorbance spectra are shown after 46 min and then after being rinsed with 10 mL of buffer after 1 h 25 min. 10 mM sodium phosphate buffer, pH 7.3, was used. A 10 point running average was performed to smooth the data.

It appears that due to the length of time of adsorption, or possibly the rinsing of the flow cell, the Soret band spilt into peaks at 410 nm and 436 nm. This indicated the presence of at least two subspecies of heme states, including possibly oxidized iron, which has a λ_{max} of around 400 nm.

2.c.2 Optimization of buffer for sGC adsorption

In an effort to increase the adsorption on sGC, the pH of the deposition buffer was lowered from 7.30 to 6.02 and the buffer was changed to MES. The buffer and the pH are known to play a key role in protein adsorption, since it affects the surface charge of the protein as well as that of the surface.

Using 5 mM MES pH 6.5 improved the adsorption of NT-13 to glass, with an increase of about 2.5 fold (Figure 2.5). However, it still had a low absorbance maximum of ~0.09 (baseline corrected), and an unusually large absorbance in the 500 nm to 650 nm range of the spectra. Therefore an even lower pH of 6.02, 5 mM MES buffer, was investigated (Figure 2.6). This resulted in a slight increase to 0.1 absorbance value (baseline corrected) of the Soret band, and more normal Q band range. While these absorbance values are enough to identify the spectra, it would make a more sensitive NO sensor if the absorbance values were greater. In an effort to attain greater protein adsorption, modifications to the glass surface were considered. It was also of utmost importance to determine if the protein still functioned to bind NO.

2.c.3. NT-13 NO binding

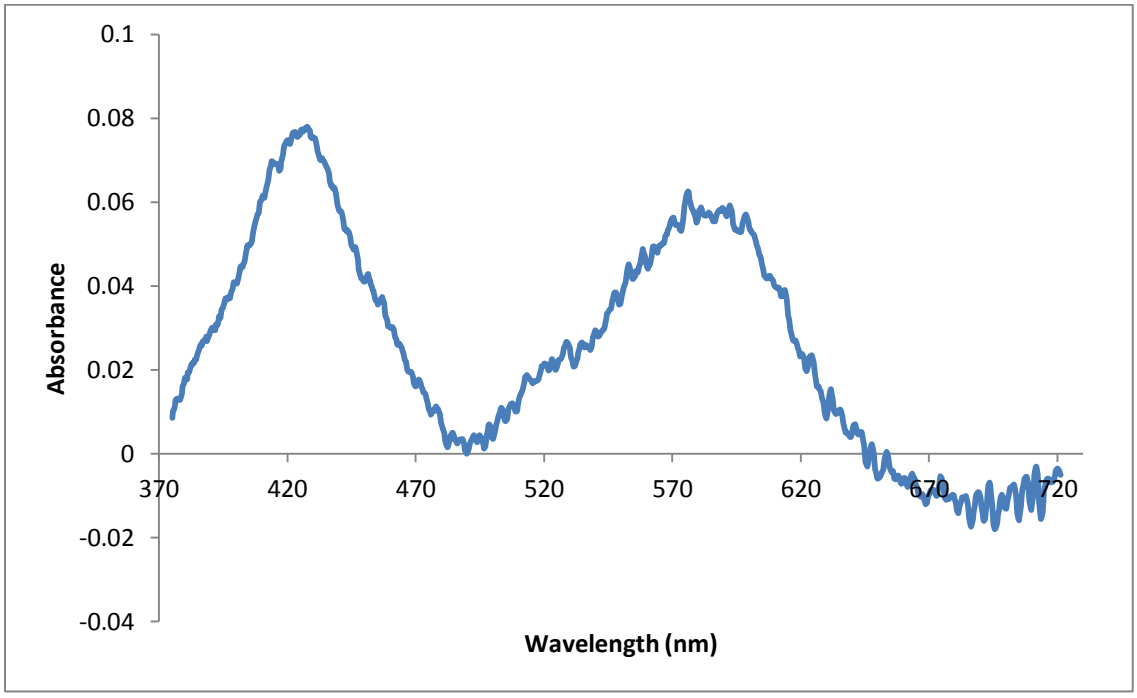

Figure 2.5. NT-13 (0.35 mg/mL) was adsorbed to a piranha cleaned 75 mm coverslip and 34 min incubation rinsed with 10 mL 5 mM MES buffer, pH 6.50. Ten ATR absorbance spectra were averaged, and a 5 point running average was performed.

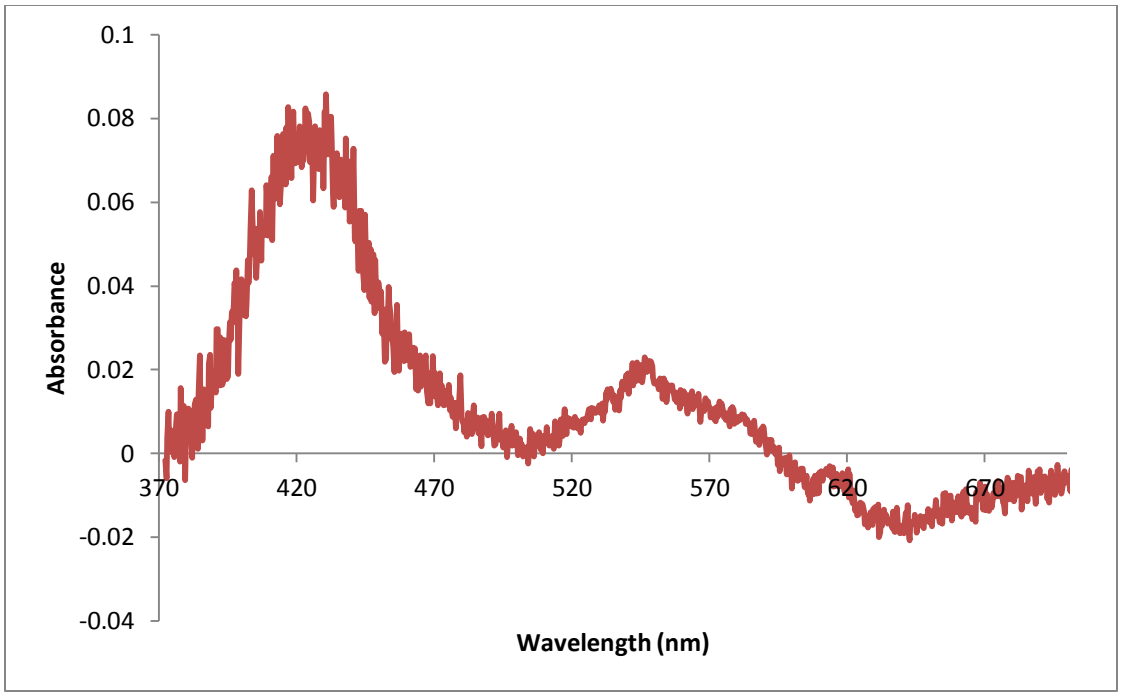

Figure 2.6. ATR absorbance spectra after NT-13 (0.417 mg/mL) was adsorbed to a piranha cleaned 75 mm coverslip and incubated for 2 h 35 min then rinsed with 10 mL buffer (5 mM MES, pH 6.02).

For developing an NO sensor from an NO binding protein, it is imperative that the protein not only bind to the surface, but that it also remain active. In order to determine if sGC NT-13 was still active while adsorbed to the surface, the NO donor DEA/NO was flowed into the flow cell.

sGC NT-13 (0.35 mg/mL) was adsorbed to a piranha cleaned 75 mm coverslip and incubated for 34 min. The flow cell was then rinsed with 10 mL buffer (5 mM MES, pH 6.50). 10 spectra were averaged and a 5 point running average of these spectra was also performed. A series of DEA/NO solutions were injected with concentrations of 1 nM, 10 nM, 100 nM, 10 μM and 500 μM. DEA/NO solutions were kept on ice until use.

NO binding to NT-13 was demonstrated using 5 mM MES buffer pH 6.50. Figure 2.7 shows a shift in the spectrum of NT-13 after 500 μM DEA/NO was injected into the flow cell. DEA/NO was given 43 min to decompose to NO, as it's half-life is 16 min at pH 7.4 and faster at lower pH.[22, 82] It was concluded that sGC was still active, although the spectra were not very clear and had odd features (such as a peak at 445 nm), and left much to be desired.

2.c.4. NT-13 adsorbed to modified glass

Surface modification to enhance protein adsorption was also investigated. Gamma-aminopropyltrimethoxysilane (GAPS) and glycydoxypropyltrimethoxylsilane (GOPS) were investigated, as they are known to aid in the binding of proteins to surfaces. Additionally, GOPS covalently binds to proteins, affixing them to the surface.

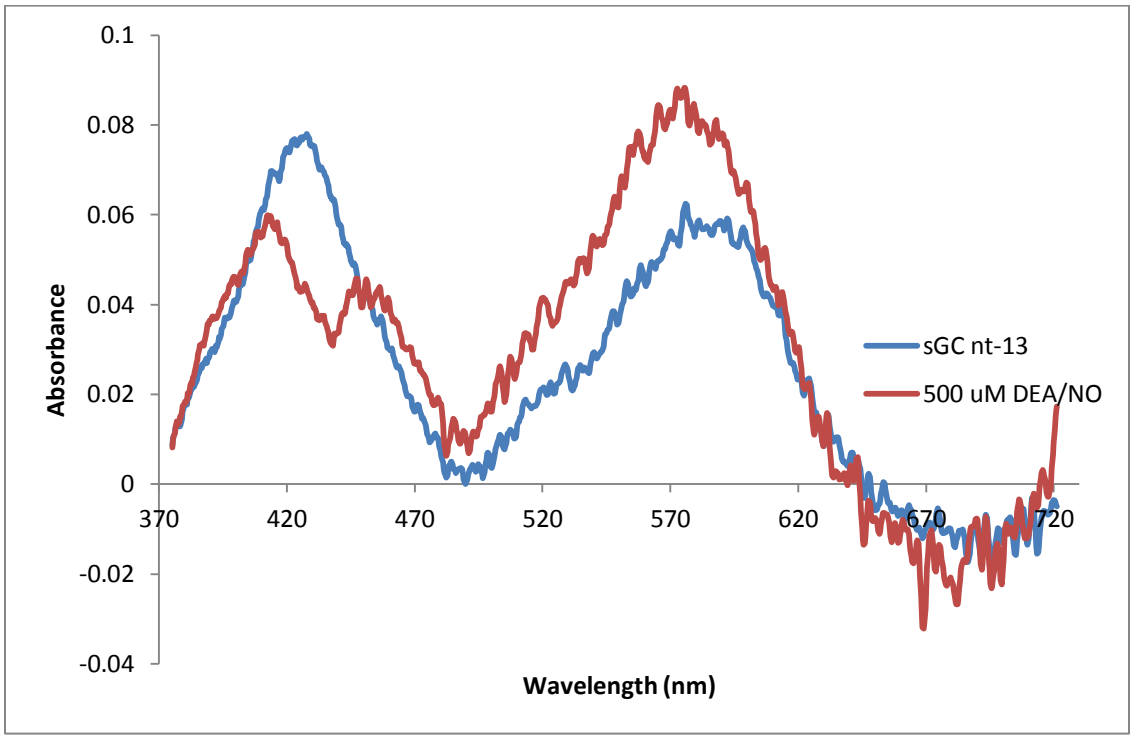

Figure 2.7. ATR absorbance spectra of NT-13 on piranha cleaned coverslip; 34 min incubation rinsed with 10 mL buffer (5 mM MES, pH 6.50). Ten spectra were averaged, and a 5 point running average performed.

Coverslips were modified with GAPS by the following procedure. 75 mm coverslips were cleaned in piranha, rinsed well with water followed by ethanol, and stored in ethanol until used. A solution of 2% GAPS in a 95:5 ethanol:water mixture was stirred for 5 min to allow for hydrolysis of the silane. Coverslips were dipped into the solution for 2 min while being stirred. Coverslips were removed and rinsed with ethanol and placed in an oven at 110 ^{o}C for 10 min to cure. GOPS coverslips were modified in the same way except that the 95:5 ethanol:water mixture was adjusted to pH 5.0 prior to hydrolysis of the silane.

The GAPS surface was incubated with 0.5 mg/mL NT-13 for 6 h 34 min in 10 mM sodium phosphate buffer, pH 7.3. During the rinse step with 10 mL of buffer, an air bubble occurred so Figure 6 displays the spectrum just prior to rinsing (10 point running average). The air bubble was evacuated in the next step. To determine if the protein was still active, a solution of 473 nM DEA/NO (0.9 mL) was injected and the spectrum was collected after 6 min (Figure 2.8). This was not enough time to allow all of the DEA/NO to release NO, since the half-life is 16 min at pH 7.4,[22, 82] but enough was released to produce a shift in the spectrum. There was a decrease in the Soret band at 433 nm. It appeared that the protein was still active but since there wasn't a concomitant rise at 400 nm it cannot be certain. The GAPS modification was not found to increase the surface bound protein, but the protein may have remained active.

Next, GOPS coverslips were tested to determine if NT-13 would increase adsorption (Figure 2.9). The experiment was cut short due to coverslip breakage, but the absorbance value of the Soret band was not as large as on bare glass under similar

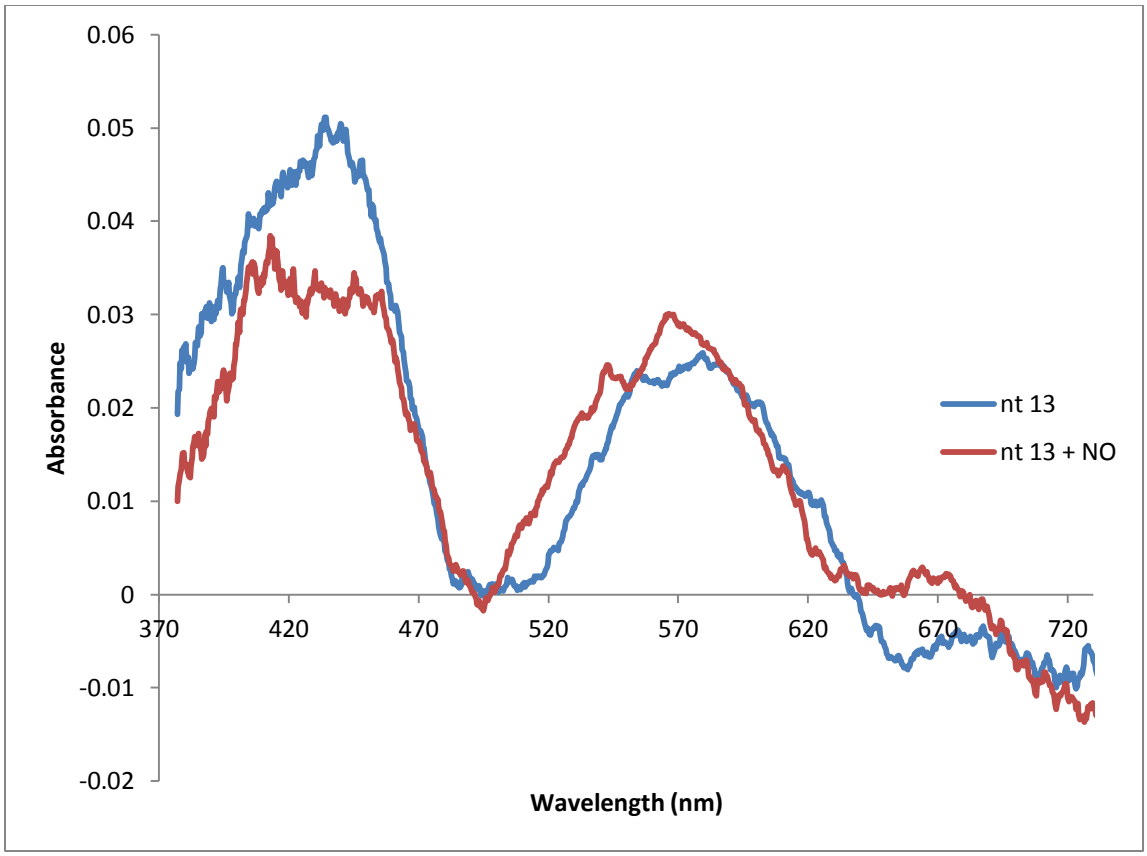

Figure 2.8. ATR absorbance spectra after NT-13 (0.5 mg/mL) was incubated for 6 h 34 min in 10 mM sodium phosphate buffer, pH 7.3, on a GAPS modified coverslip. A 10 point running average was applied.

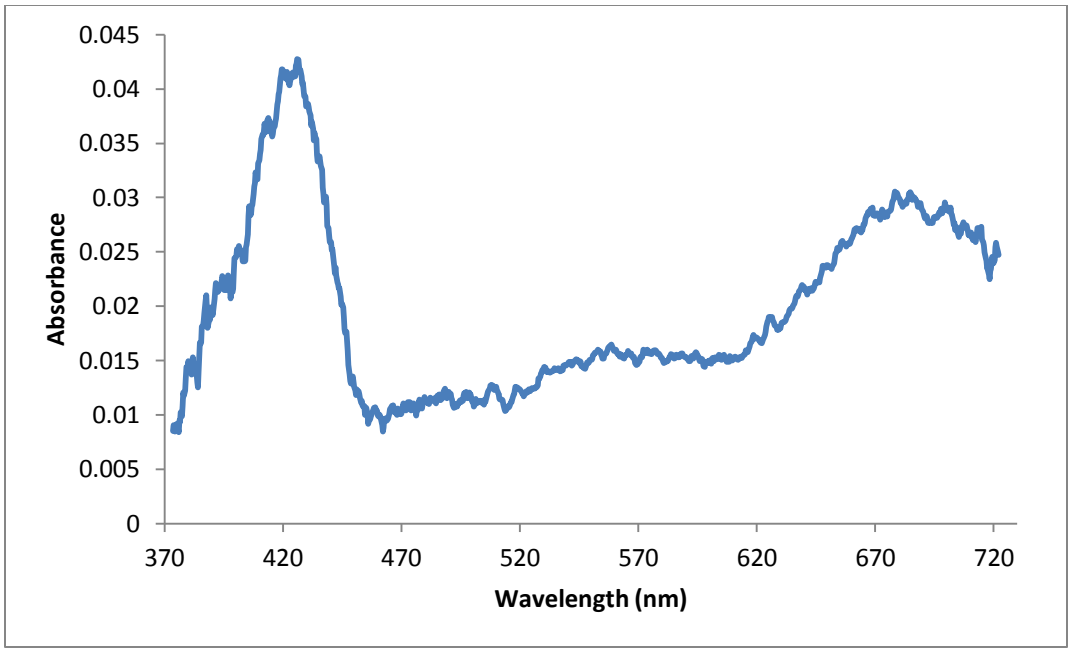

Figure 2.9. ATR absorbance spectra of NT-13. NT-13 (0.2 mg/mL) was incubated for 1 h 56 min in 10 mM phosphate buffer, pH 7.3, on a GOPS modified coverslip. A ten point running average was applied.

condition. It was therefore concluded that the modifications to the surface were either the same or worse for binding NT-13. We therefore decided to change the protein itself to increase adsorption.

2.c.5. Nitrophorin 4 as an NO sensor

Since we had only limited success with sGC, we determined it was best to examine other NO binding proteins for use as an NO sensor. Nitrophorin 4 (NP4) was an obvious choice since it is also a natural NO binding protein. It has advantages over sGC in that the NO binding is more readily reversible (by increasing the pH), can be produced in large yields, is 25% the size of sGC (which could increase surface packing density) and is structurally stable (sGC tends to aggregate). For these reasons, I investigated nitrophorin as a protein based NO sensor on an ATR platform.

We took advantage of the uniquely tight binging of nitric oxide (NO) to nitrophorins to construct a nitric oxide sensor on an optical waveguide platform. The basis of the sensor is a spectral shift in the Soret band from a λ_{max} of 403 nm unligated to 419 nm with NO bound. We attempted to design nitrophorin 4 to have less pH sensitivity for binding NO by introducing three site-specific mutations, D30N, E32Q, D35N, denoted as NP4 NQN (MW = 20880 Da). This work was performed by Aaron Issaian. *wt*NP4 binds NO with a K_d of 50 nM at pH 5.0 and its K_d rises to 540 nM at pH 8.0, in solution.[83] The K_d we determined for NP4 NQN was 85 ± 3 nM at pH 5.00 and 450 ± 40 nM at pH 7.5 (Figures 2.10-2.13, determined by Aaron Issaian). A significant decrease

of pH dependence on NO binding was not realized; nonetheless, the protein was successfully used as an NO sensor.

The optical waveguide allowed for use as a flow cell. The number of internal reflections in the waveguide increases as the thickness of the waveguide decreases.[74, 75] The use of a coverslip was required to provide enough signal for absorbance measurements.

To determine if NP4 NQN would be able to adsorb to glass coverslips, we examined the deposition of NP4 NQN in 5 mM Tris, pH 7.6 (Figure 2.14). This condition proved to be successful, as a good spectrum was recorded. The Soret was at 409 nm, which was a red shift of about 6 nm from the solution maximum. The absorbance value of ~0.1 (baseline corrected) was respectable, higher than NT-13, but a larger value would be more desirable.

2.c.6. NP4 NQN NO binding

If an NO sensor was to be constructed from NP4 NQN, the protein must not only be bound to the surface, it must remain active as well. To determine if NP4 NQN was still able to bind NO while adsorbed to the surface, DEA/NO was injected.

Figure 2.15 shows the resultant spectra from successive DEA/NO injections, proving that NP4 NQN still binds NO while bound to the glass coverslip. Binding was reversible in this experiment and rinsing with 5 mM Tris pH buffer (pH 7.5) following the last DEA/NO injection shifted the spectrum back to nearly the original spectrum

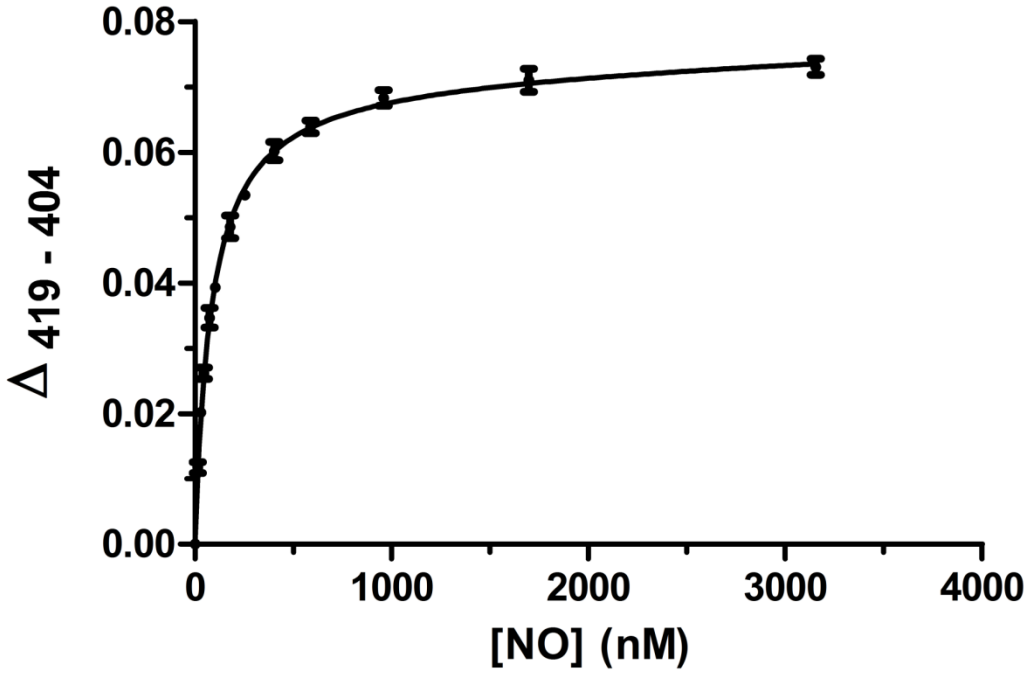

Figure 2.10. NP4 NQN solution binding assay, in 5 mM sodium acetate, pH 5.00. Data provided by Aaron Issaian

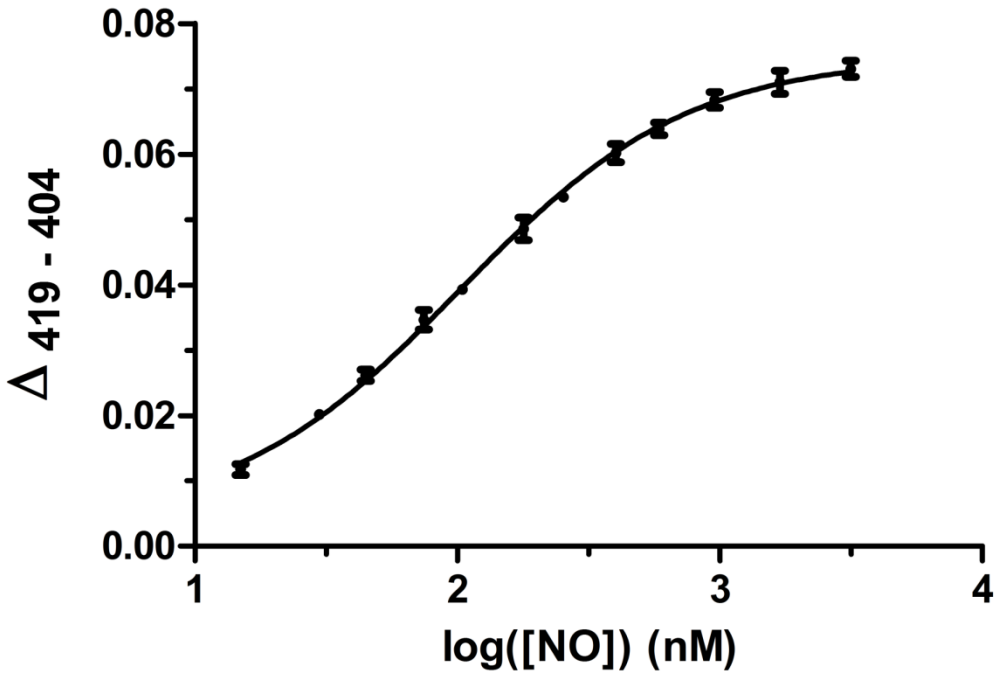

Figure 2.11. NP4 NQN solution binding assay, in 5 mM sodium acetate, pH 5.00, on a log scale. Data provided by Aaron Issaian.

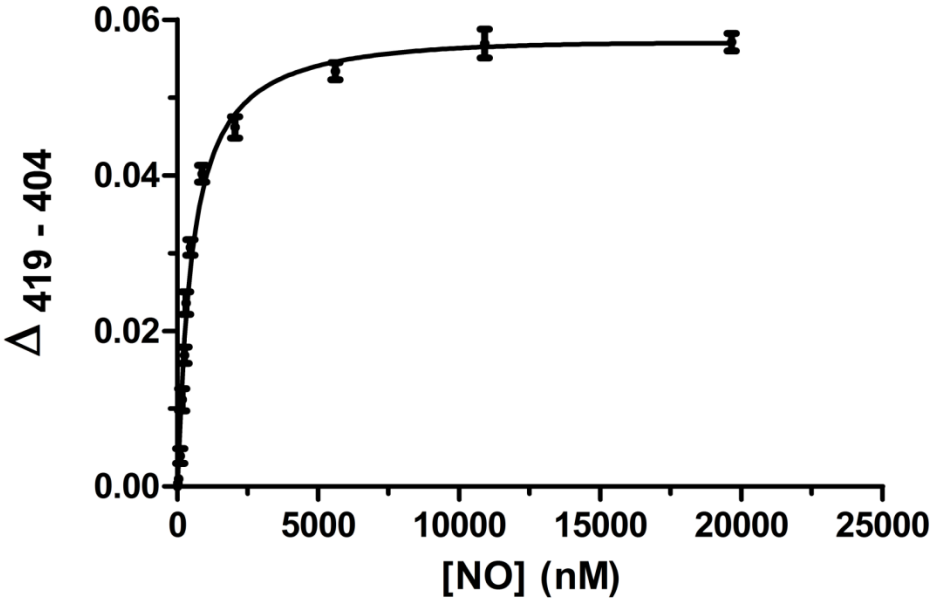

Figure 2.12. NO binding curve to NP4 NQN, performed in 10 mM TRIS, pH 7.50. Data provided by Aaron Issaian.

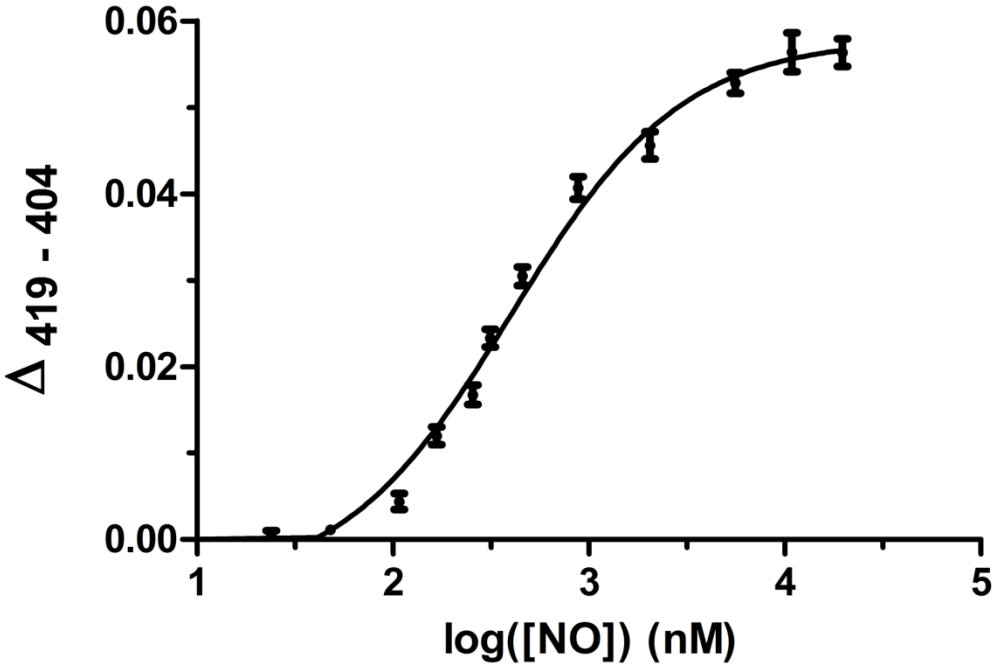

Figure 2.13. NO binding curve to NP4 NQN, performed in 10 mM TRIS, pH 7.50. Data provided by Aaron Issaian.

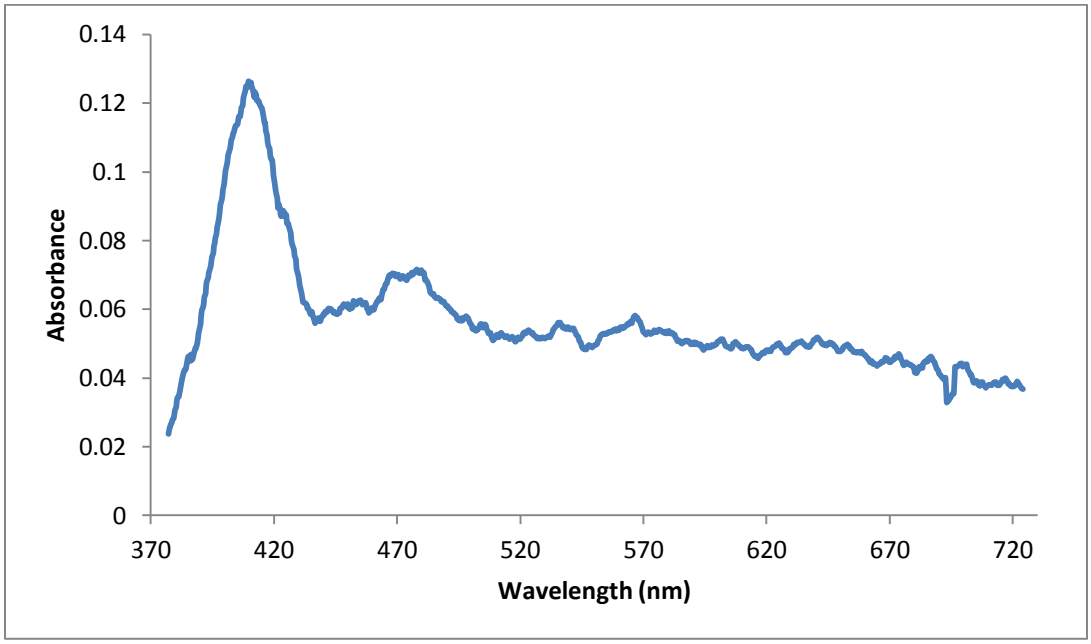

Figure 2.14. NP4 NQN (10 μM) was incubated for 2 h 53 min on a piranha cleaned coverslip in 5 mM Tris buffer, pH 7.6, then rinsed with 18 mL of buffer. ATR absorbance spectra were obtained and a 10 point running average was performed.

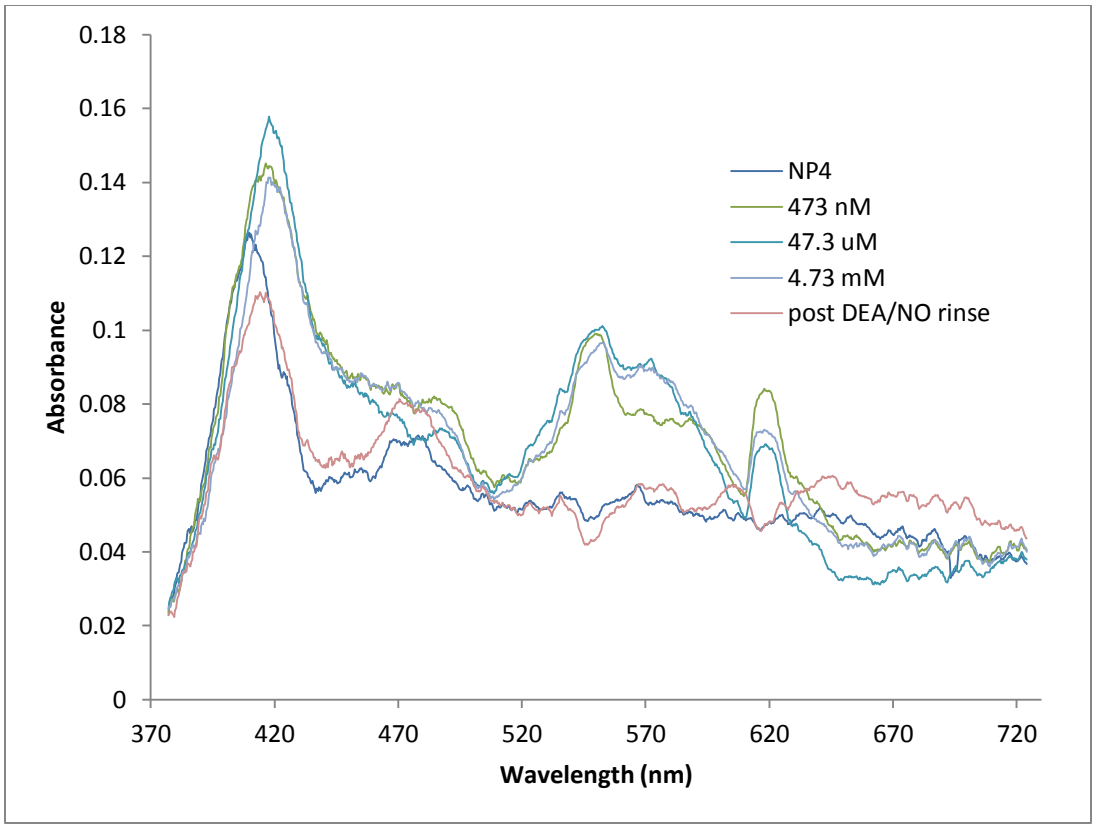

Figure 2.15. ATR absorbance spectra after NP4 NQN (10 μM) was adsorbed for 2 h 53 min to a piranha-cleaned 75 mm coverslip in 5 mM Tris, pH 7.6, then rinsed with 18 mL of the same buffer. DEA/NO was injected (700 mL) with concentrations of 473 nM, 47 μM and 4.73 mM, and given 8-10 min to decompose and release NO. The flow cell was then rinsed with 20 mL of buffer. A ten point running average was performed to smooth the spectra.

obtained prior to DEA/NO injections. This was a major advancement in the development of the NO sensor since I now have a protein that is still active on the surface and binds reversibly. Next, I investigated whether we could get increased protein adsorption to the surface, and at the same time take advantage of the higher NO binding constant for NP4 at lower pH. I varied pH, cleaning method, surface modification and buffer type to optimize binding.

2.c.7. Optimization of pH for adsorption of NP4 NQN

To determine if there were better conditions for adsorption, I examined two other buffers at different pH values. We decided to investigate more acidic conditions, due a lower K_d for NO binding to NP4, which would yield a sensor with a lower detection limit.

NP4 NQN binding increased using 5 mM MES pH 6.02 (Figure 2.16) compared to 5 mM Tris, pH 7.6. The absorbance of the Soret band was 0.21, which is 2 fold greater. The protein was still active and displayed reversible shifting from a λ_{max} at 404 nm to 416 nm when NO bound, and back when the flow cell was rinsed. Figure 2.17 is a spectrum of NP4 NQN adsorbed using 5 mM sodium acetate buffer pH 5.00. The absorbance value of the Soret is very close to that with pH 6.02 MES buffer. At pH 5, the K_d of NO to NP4 is at a minimum, so that would be the ideal pH for the sensor with respect to detection limit.

2.c.8. GOPS surface modification for increased NP4 NQN binding

In a further effort to increase the absorbance value of the Soret band we used a

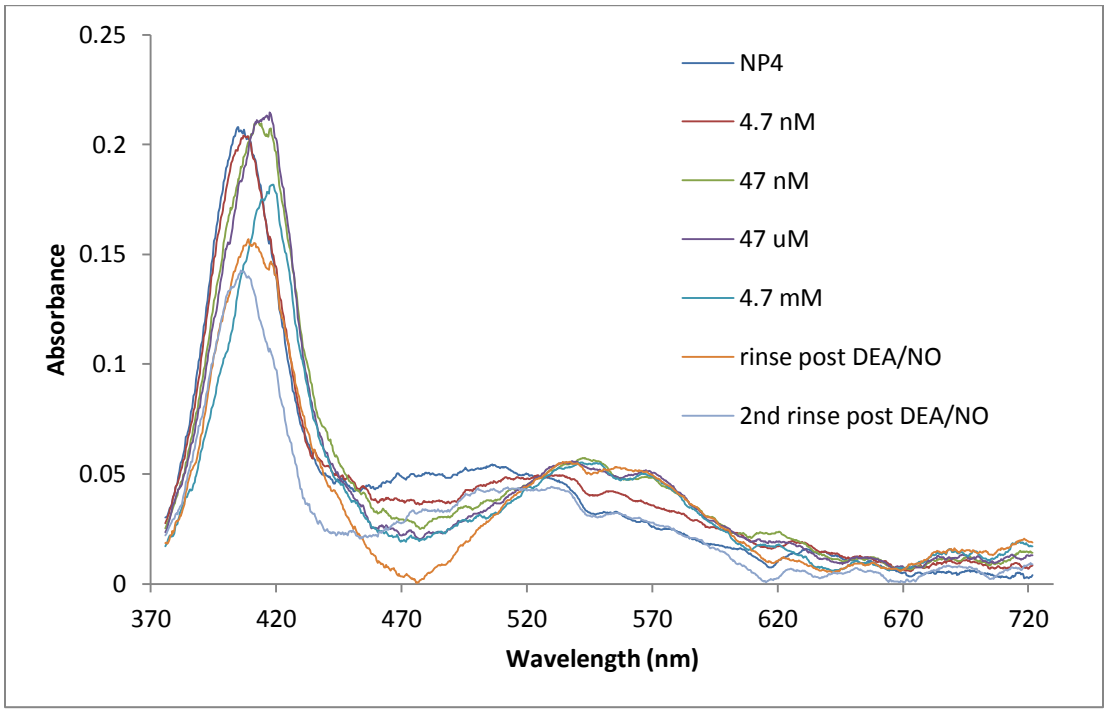

Figure 2.16. ATR absorbance spectra after NP4 NQN (0.2 mg/mL) was adsorbed on piranha cleaned glass coverslips in 5 mM MES buffer, pH 6.02, for 20 min, then rinsed with 10 mL of the same buffer. DEA/NO was injected (500 to 700 μL) at concentrations of 4.73 nM, 473 nM, 47.3 μM and 4.73 mM, each injection was given 5-7 min for equilibration. The flow cell was then rinsed with 20 mL of buffer twice. Spectra were subjected to 10 point running average.

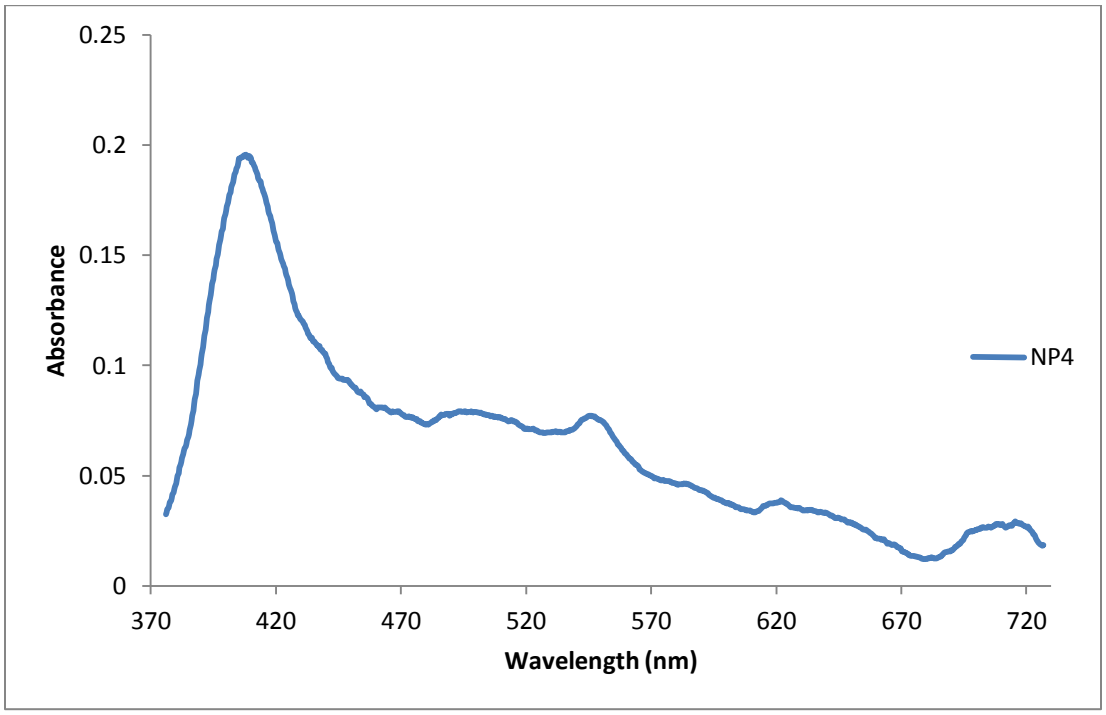

Figure 2.17. NP4 NQN (0.2 mg/mL) was also adsorbed to piranha cleaned glass in 5 mM sodium acetate buffer, pH 5.00, for 29 min. Five ATR absorbance spectra were averaged and a 10 point running average was then performed.

GOPS modified coverslip to bind NP4 NQN to the surface. GOPS modified surfaces are known to bind proteins.

As can be seen in Figure 2.18, the absorbance of the Soret band increased by about 15 % over that of a plain glass coverslip (Figure 2.16). Due to the small increase in surface coverage of NP4 NQN with GOPS it was not used in subsequent experiments.

2.c.9. Ferrous form of NP4 NQN

Experiments were conducted in an effort to obtain reduced NP4 NQN (Fe^{2+}), which is expected to bind NO with a dissociation constant of ~ 5-90 fM.[83] The most straightforward method of using the reducing agent sodium dithionite accomplished the reduction.

The Soret peak shifted from 414 nm to 430 nm, as expected for the reduction of NP4 NQN (Figure 2.19). It is not known why the Soret in the starting spectrum was at 414 nm prior to addition of sodium dithionite, but it is reasonable to assume that such a shift to 430 nm was due to reduction. The protein oxidized back to the Fe^{3+} state within 20 min. This experiment was only performed once.

It was rationalized, due to the short-lived nature of the reduced form of the protein that sodium dithionite would have to be added with the sensor in order to keep it reduced. However, sodium dithionite is also reactive with proteins, which would limit the sensor's lifetime, and with NO, which precludes simultaneous addition of both. If the reduced protein were somehow stabilized, or another reductant were used that is not reactive with NO, then it would open up the possibility. Following the measurement NP4 NQN could

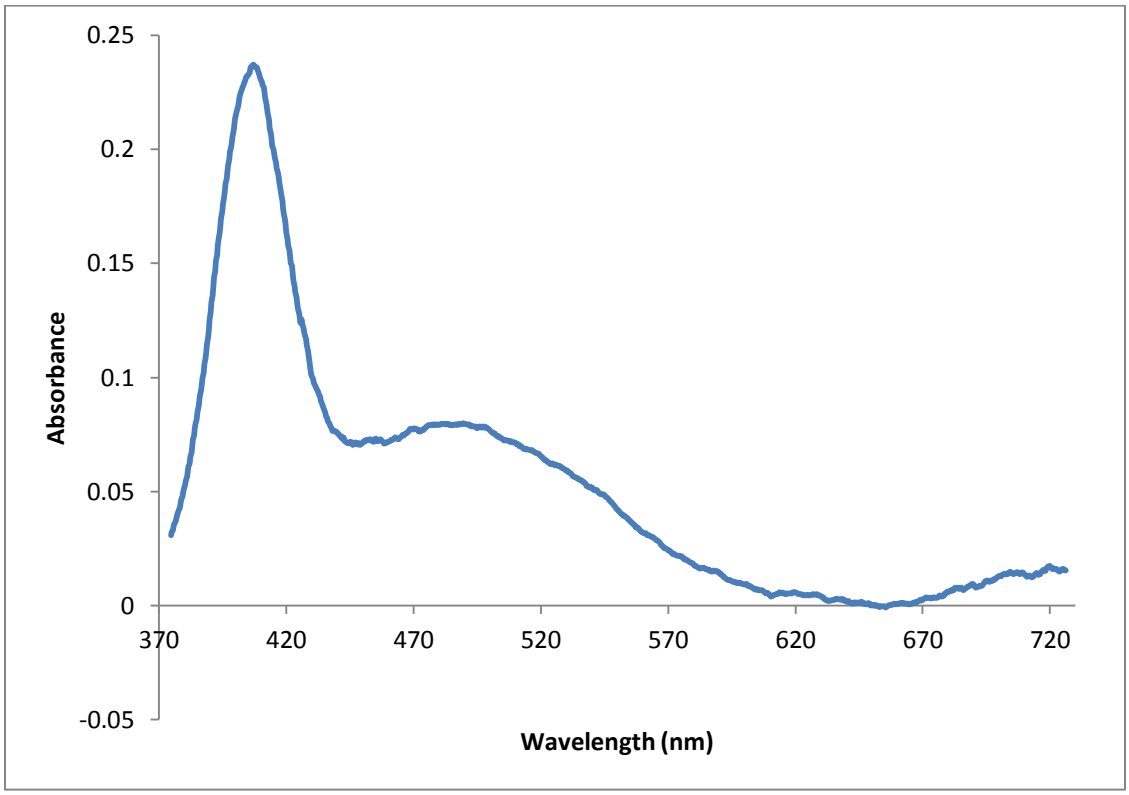

Figure 2.18. ATR absorbance spectra after NP4 NQN (0.2 mg/mL) was adsorbed to a GOPS modified coverslip (see section 2.c.4 for silane modification procedure) for 1 h 22 min in 5 mM MES buffer, pH 6.02. The flow cell was then rinsed with 10 mL of the same buffer. Three spectra were averaged, and a 10 point running average was also performed to smooth the spectra.

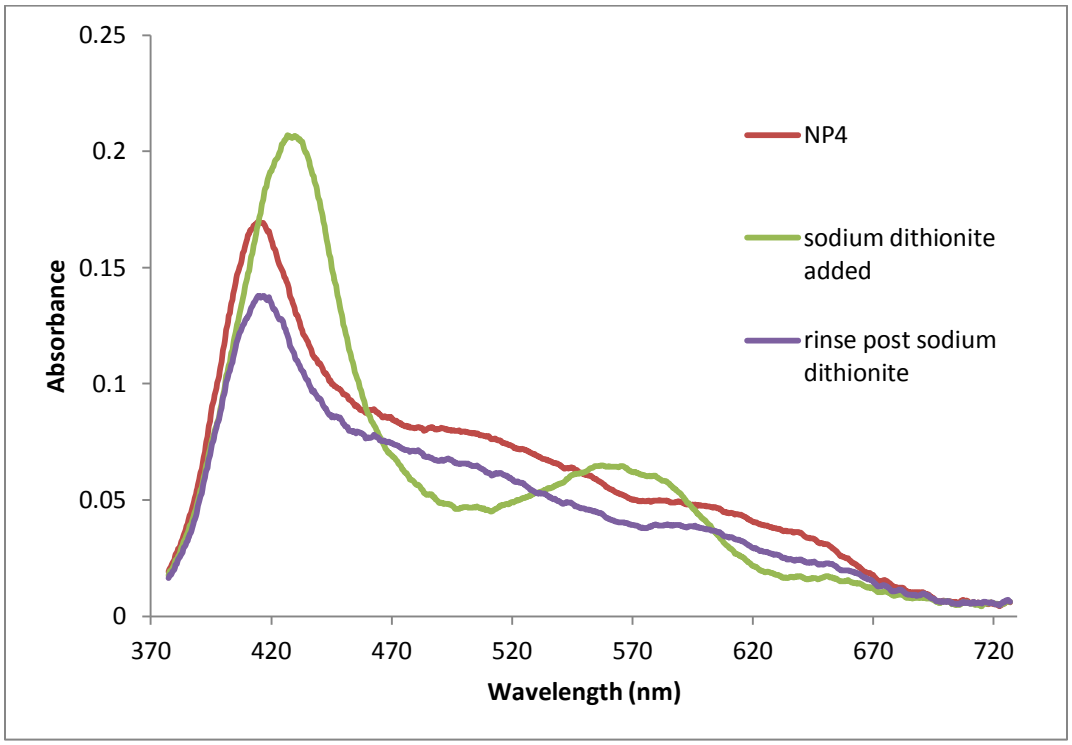

Figure 2.19. ATR absorbance spectra after NP4 NQN (0.2 mg/mL) was adsorbed onto a piranha cleaned coverslip using 5 mM MES buffer, pH 6.5, for 42 min. The flow cell was then rinsed with 15 mL of the same buffer. Sodium dithionite (0.8 mL of 0.4 mg/mL) was injected and the spectrum was collected after 1 min. The flow cell was then rinsed with 15 mL of the same buffer and the spectrum was collected again. All spectra presented were averaged from 5 spectra, and a 10 point running average.

be oxidized to release the bound NO by way of weaker NO binding, and hence the unligated state could be recovered. While ambitious, the reduced form of NP4 NQN was not required to construct an NO sensor using the protein. Therefore the focus of the work was shifted back to working with the ferric form of the protein.

2.c.10 NP4 NQN NO binding study

It was decided that pH 5 was the most optimal for the sensor because the K_d was smallest and therefore the sensor would be most sensitive at this pH. Also the protein adsorbed well to piranha cleaned glass at this pH.

All buffers were deaerated prior to experiment. DEA/NO solution were prepared at 100x in 10 mM NaOH in 1.8 mL tubes with only a small amount of headspace. Each DEA/NO solution was diluted in buffer from the stock solution in 10 mM NaOH immediately prior to injection, then given 1 min to decompose to NO. The short time allotment of DEA/NO degradation to NO was appropriate here because DEA/NO releases NO within seconds at pH 5.[23] The addition of 1:100 DEA/NO to 5 mM sodium acetate buffer, pH 5.00, caused an increase of the pH by 0.17 units due to the 10 mM NaOH solvent, although the pH of the solution is still reported herein to be 5.00.

To compensate for the low concentration of ligand in solution compared to the protein on the surface (6 pmol/cm^2), the DEA/NO solution was flowed through the ATR cell. NO has a diffusion constant of 3300 $\mu m^2/s$,[14] which is large for a diffusion constant, but the height of the flow cell is 1 mm. At low concentrations of NO a ligand depletion

layer could form yielding a condition where the system is not at equilibrium. The furthest a molecule of NO would have to travel in the flow cell would be 1 mm to reach the surface to bind with the protein. Under these conditions the time for NO to reach the surface would be:

$$d^2 = 2Dt \qquad \text{(eq. 2.1)}$$

Where d is the mean square distance, D is the diffusion constant (3300 $\mu m^2/s$),[14] and t is time in seconds. This equation neglects friction, which for small, uncharged species, is appropriate. Thus, 150 s would be the time required for NO to travel the largest possible distance, the height of the ATR cell (1 mm), and reach the sensor surface. To eliminate this potential source of error, the NO solution was flowed through to effectively eliminate the depletion of NO from the surface of the ATR substrate. This was performed manually with a syringe.

The binding assay was performed by injecting increasing concentrations of DEA/NO through the flow cell starting with 50 mL of 5 nM DEA/NO at a rate of 7 - 10 mL/min. After 50 mL of solution was flowed through the ATR cell, 1 min was allowed to pass before spectra were collected. The flow of ligand compensated for the relatively low ligand concentration in solution to avoid the possible formation of a ligand depletion layer just above the surface of the ATR substrate. This was followed by an injections of 20 mL of 12 nM DEA/NO at a rate of 3.3 to 10 mL/min. Then 10 mL of 25 nM DEA/NO was injected, followed by 10 mL of 50 nM, both at 5 mL/min. After which 3

mL of 75 nM and 100 nM DEA/NO solutions, and 2 mL of each 150 nM , 200 nM, 250 nM, 300 nM, 450 nM, 600 nM, 1.2 μM, 5 μM, 25 μM DEA/NO were injected at a rate of 2 – 3 mL/min. After each injection, one min was allowed for diffusion, binding and equilibration before spectra were taken. The rate of NO binding to NP4 is near diffusion limited so equilibration is very fast. The flow cell was then rinsed with 20 mL of 5 mM Tris buffer pH 7.50, to release all bound NO. The sensor was then re-equilibrated with 20 mL of 5 mM sodium acetate buffer, pH 5.00. This procedure was repeated two more times. A minimum of 100 spectra were averaged for each acquisition, and a 10 point running average was applied to the spectra.

DEA/NO, a nitric oxide (NO) donor, was flowed through the sensor in increasing concentrations. At pH 5, DEA/NO releases NO within seconds.[23] It was assumed that the extinction coefficient at 250 nm was 8 $mM^{-1}cm^{-1}$, and stock DEA/NO concentrations were quantified with that value. The extinction coefficient at 250 nm has been reported to be as low as 6.5 $mM^{-1}cm^{-1}$,[22] and if this were the case then the concentration of DEA/NO and therefore NO would be 19% overestimated. This would have the effect of lowering the detection limit reported herein by 19%. The other assumption made is that 1.5 moles of NO were released per mole of DEA/NO. This value could be as high as 1.8 moles of NO per mole of DEA/NO. If 1.8 is the actual value it would have the effect of underestimating the amount of DEA/NO by 30%. This would have the effect of raising the detection limit reported herein by 30%.

The surface coverage of NP4 NQN was calculated to be 6 $pmol/cm^2$, assuming a two-phase approximation (i.e. the refractive index does not change due to the adsorption

of the protein) and the same extinction coefficient as a solution phase isotropic value of 141,400 $M^{-1}cm^{-1}$ at 404 nm,[64] as described by Saavedra and Reichert.[76] The small number quantity of protein on the surface allows for the determination of K_d values by simple titration. A true adsorption isotherm was never performed to determine if the surface was indeed saturated with protein. However, two different concentrations of NP4 NQN was adsorbed to the surface at pH 5.00 in 5 mM sodium acetate buffer, at 0.2 mg/mL (Figure 2.17) and 1.4 mg/mL (Figure 2.20). The 7-fold increase in concentration yielded an ~2 fold increase in absorbance, 0.19 to 0.39 at the Soret maximum. The absorbance value of 0.39 was determined to be sufficient to conduct the following experiments. This does not prove that the absorbance could not have been increased further with yet higher concentrations of protein.

The nitrophorin 4 (NP4) Soret band shifts from its unligated λ_{max} at 404 nm to its NO bound λ_{max} at 416 nm (Figures 2.20-2.25), the difference spectra are shown in Figures 2.26-2.29, respectively. Three trials on the same sensor were performed. The binding curve generated demonstrates the lowest concentration detected at 18 nM NO and was linear up to 225 nM NO Figures 2.29 and 2.30). The dissociation constant of NO to NP4 NQN in the sensor was found to be 160 +/- 20 nM. The sensor was demonstrated to be reversible and reusable. The sensor was rinsed with 5mM Tris, pH 7.50, and the unligated Soret peak was recovered. The binding assay was repeated a total of three times on the same sensor. The binding curve behaved in a very similar manner each time decreasing slightly with each series presumably from protein being flushed off, since it was not covalently attached. The data in Figures 2.29 and 2.30 are the average of

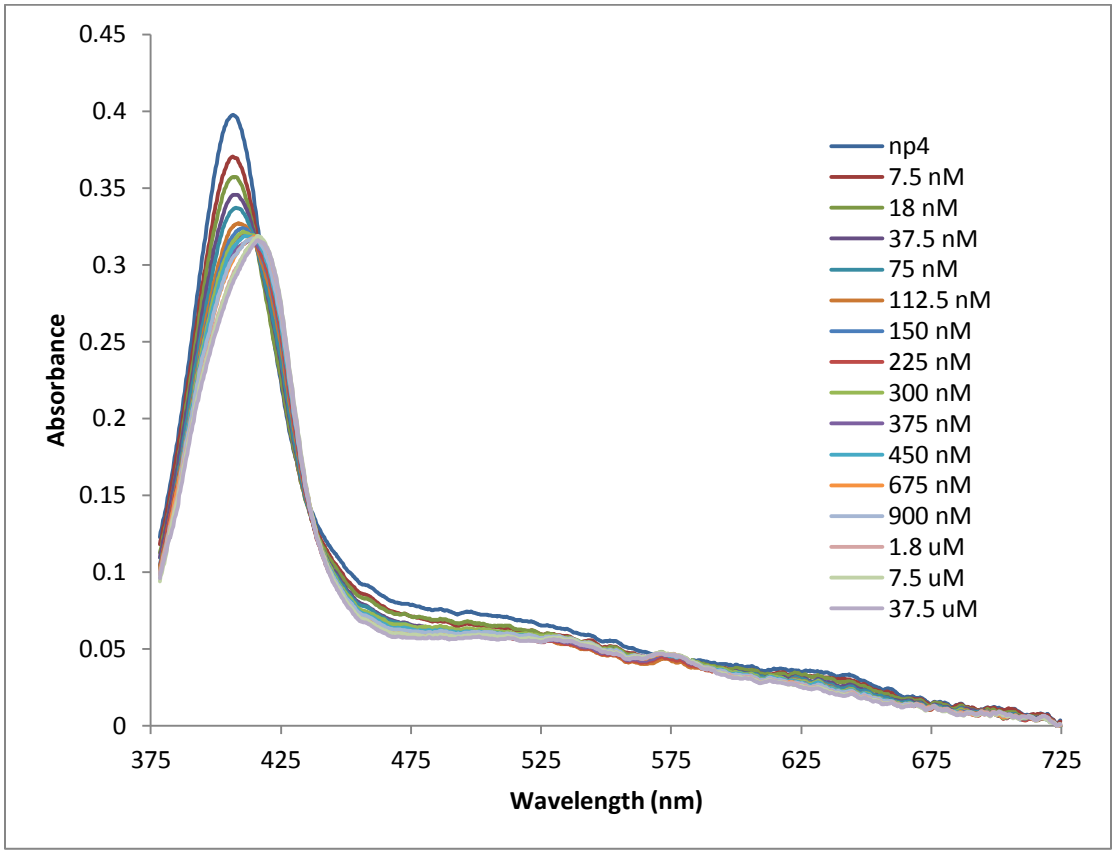

Figure 2.20. ATR absorbance spectra of binding assay of NO sensor, trial 1. 5 mM sodium acetate buffer, pH 5.00, was used.

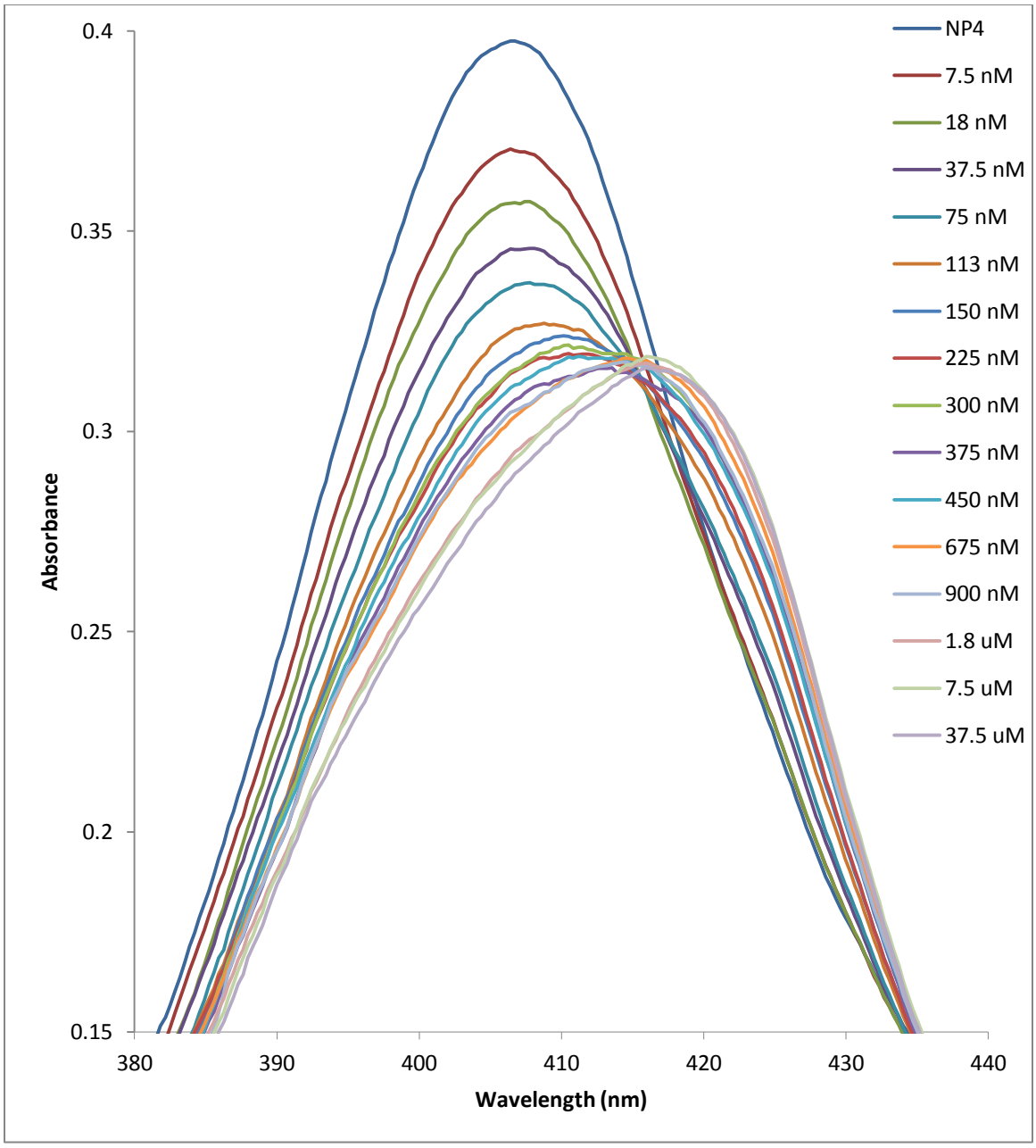

Figure 2.21. Enlarged view of the Soret region in Figure 2.20.

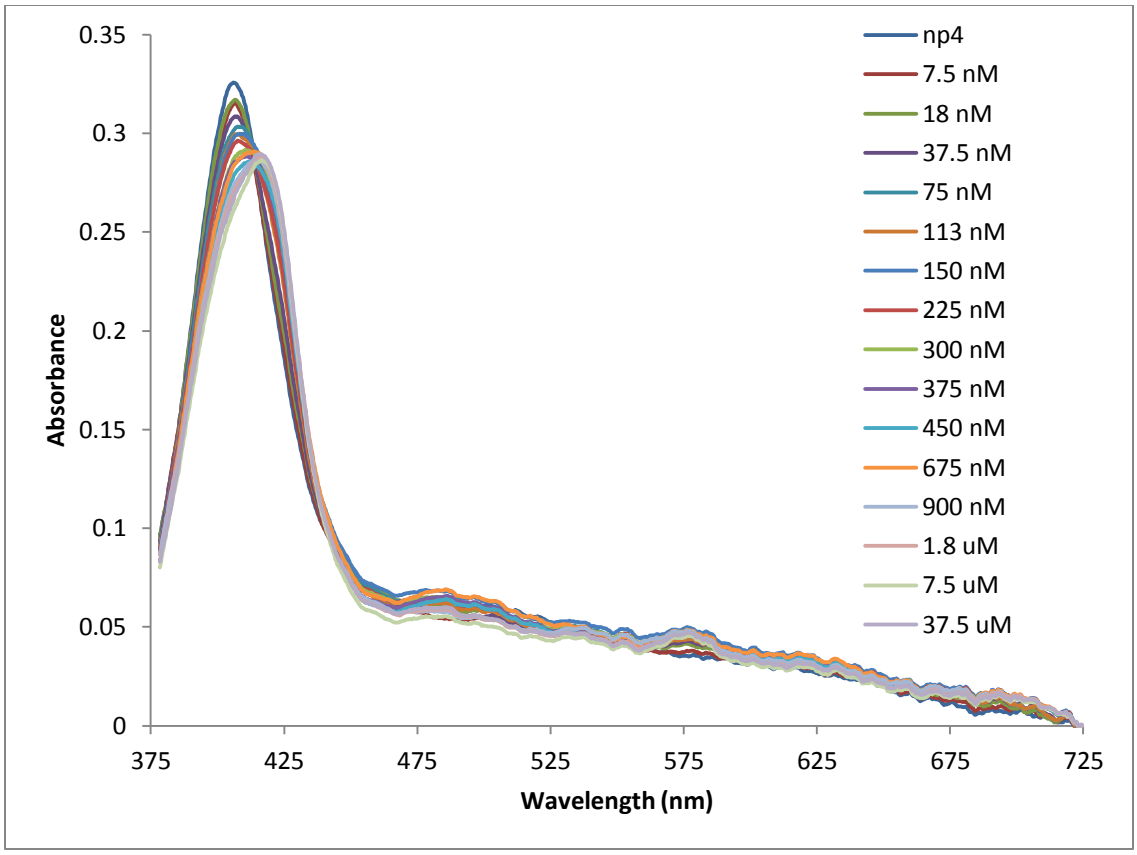

Figure 2.22. ATR absorbance spectra of trial 2 of binding assay of NO to the same sensor as Figure 2.18. 5 mM sodium acetate buffer, pH 5.00, was used.

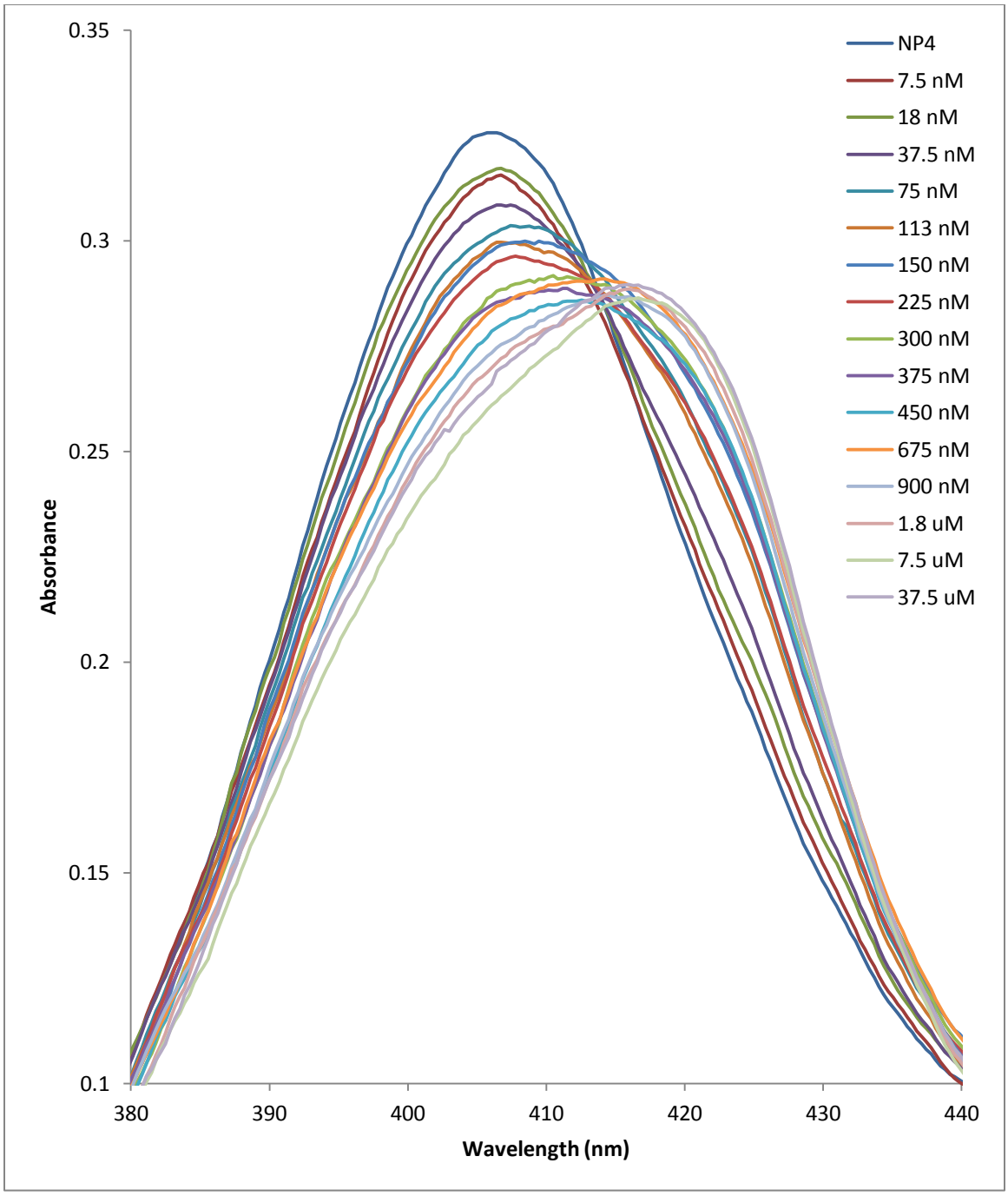

Figure 2.23. Enlarged view of the Soret region in Figure 2.22.

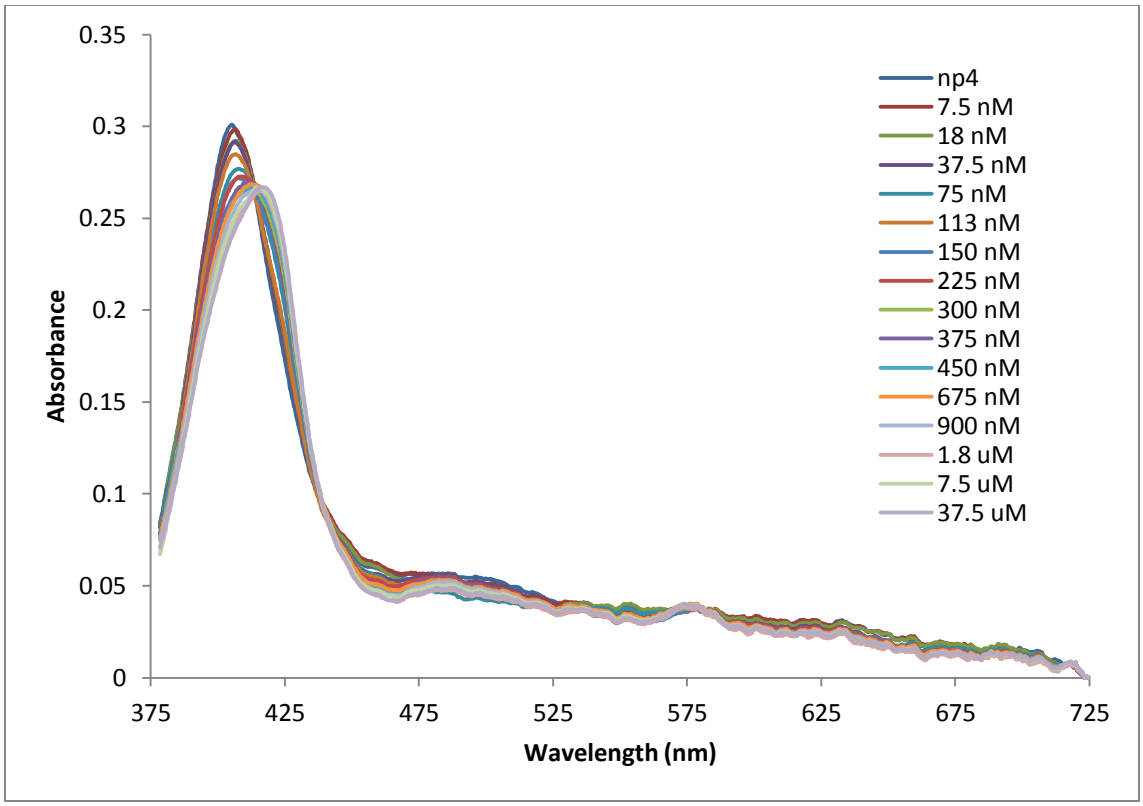

Figure 2.24. ATR absorbance spectra of binding assay of NO to the same sensor as Figures 2.18 – 2.23, trial 3. 5 mM sodium acetate buffer, pH 5.00, was used.

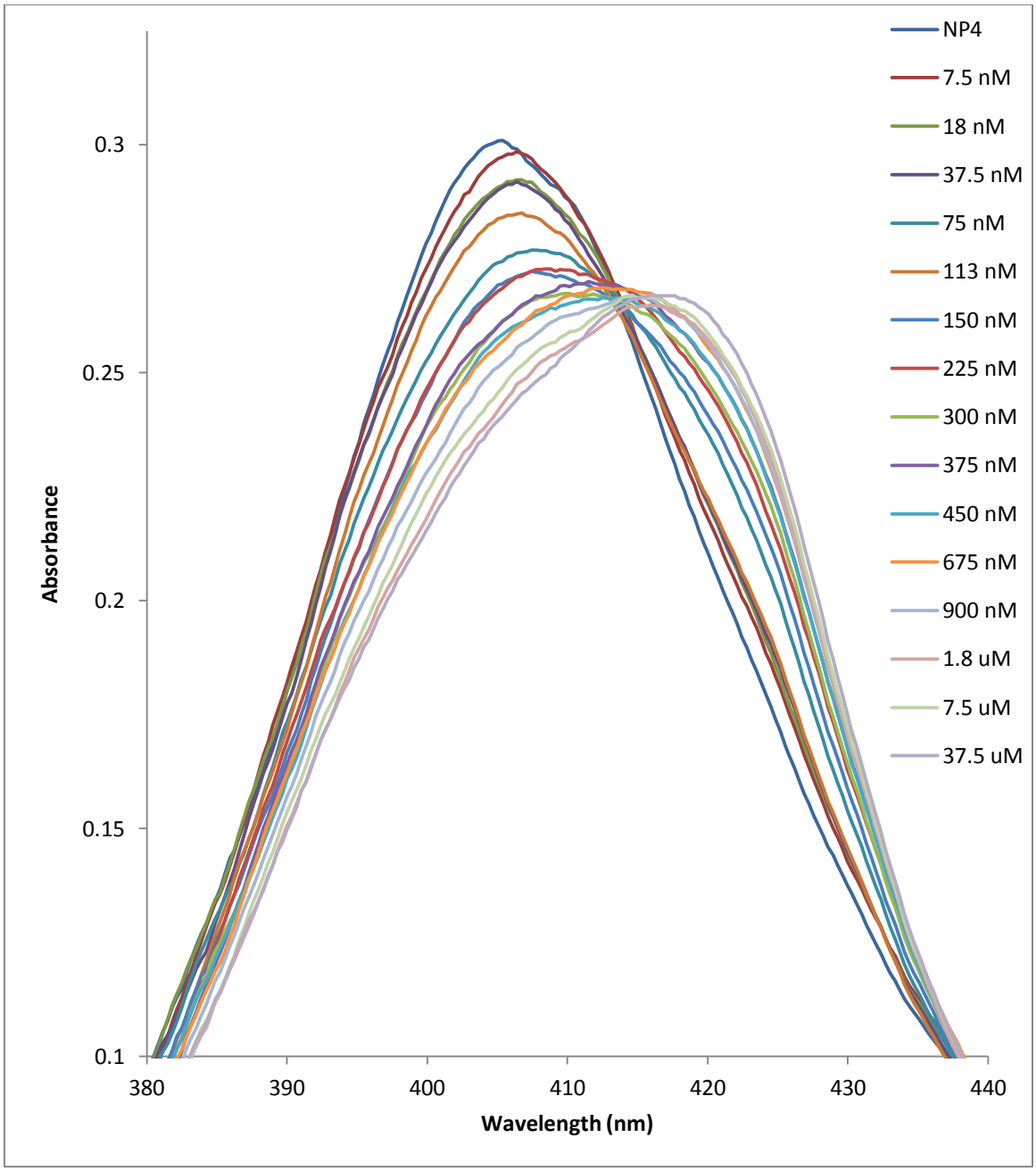

Figure 2.25. Enlarged view of the Soret region in Figure 2.24.

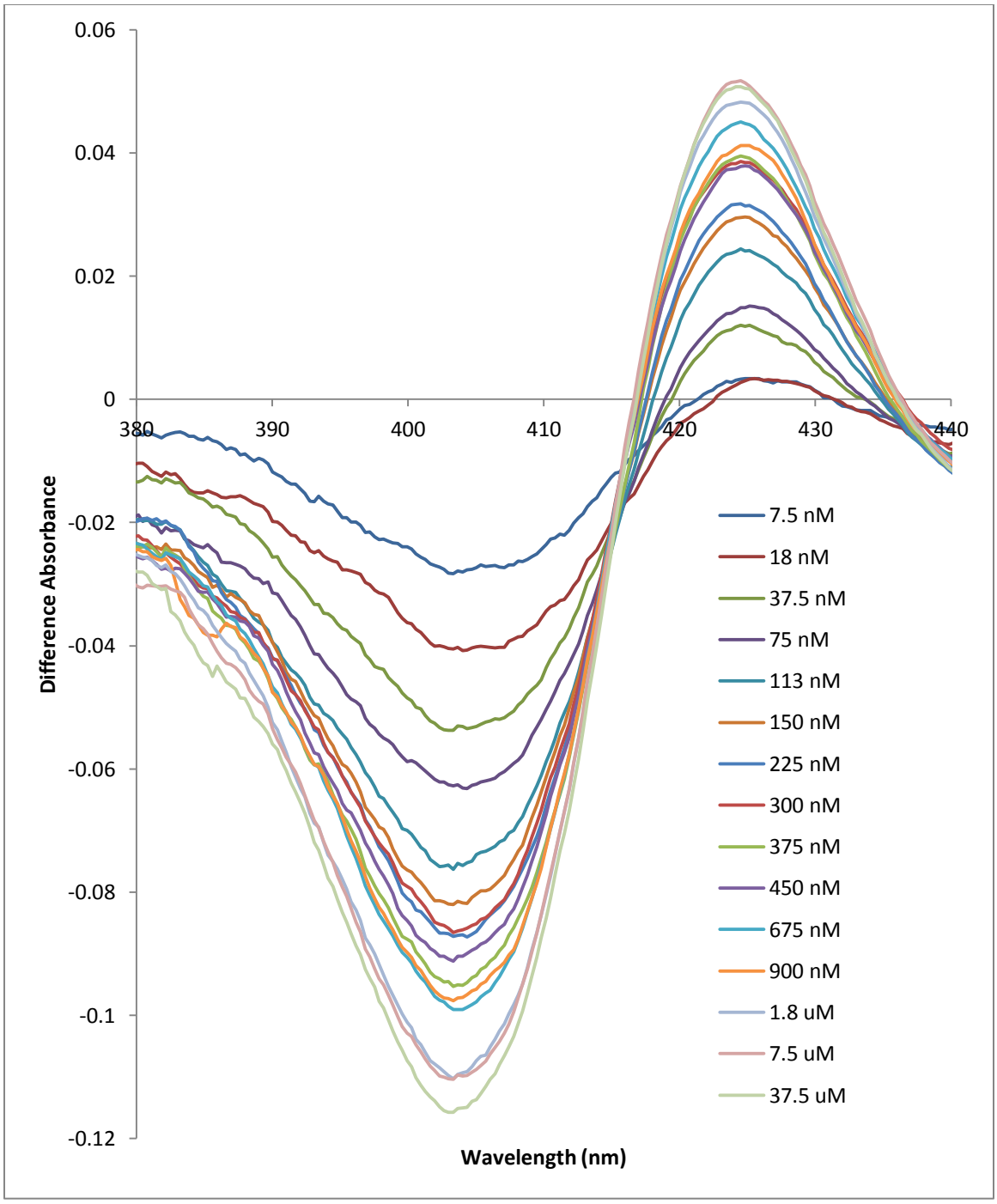

Figure 2.26. Trial 1 (Figure 2.18) difference absorbance spectra, 5 mM sodium acetate buffer, pH 5.00, was used.

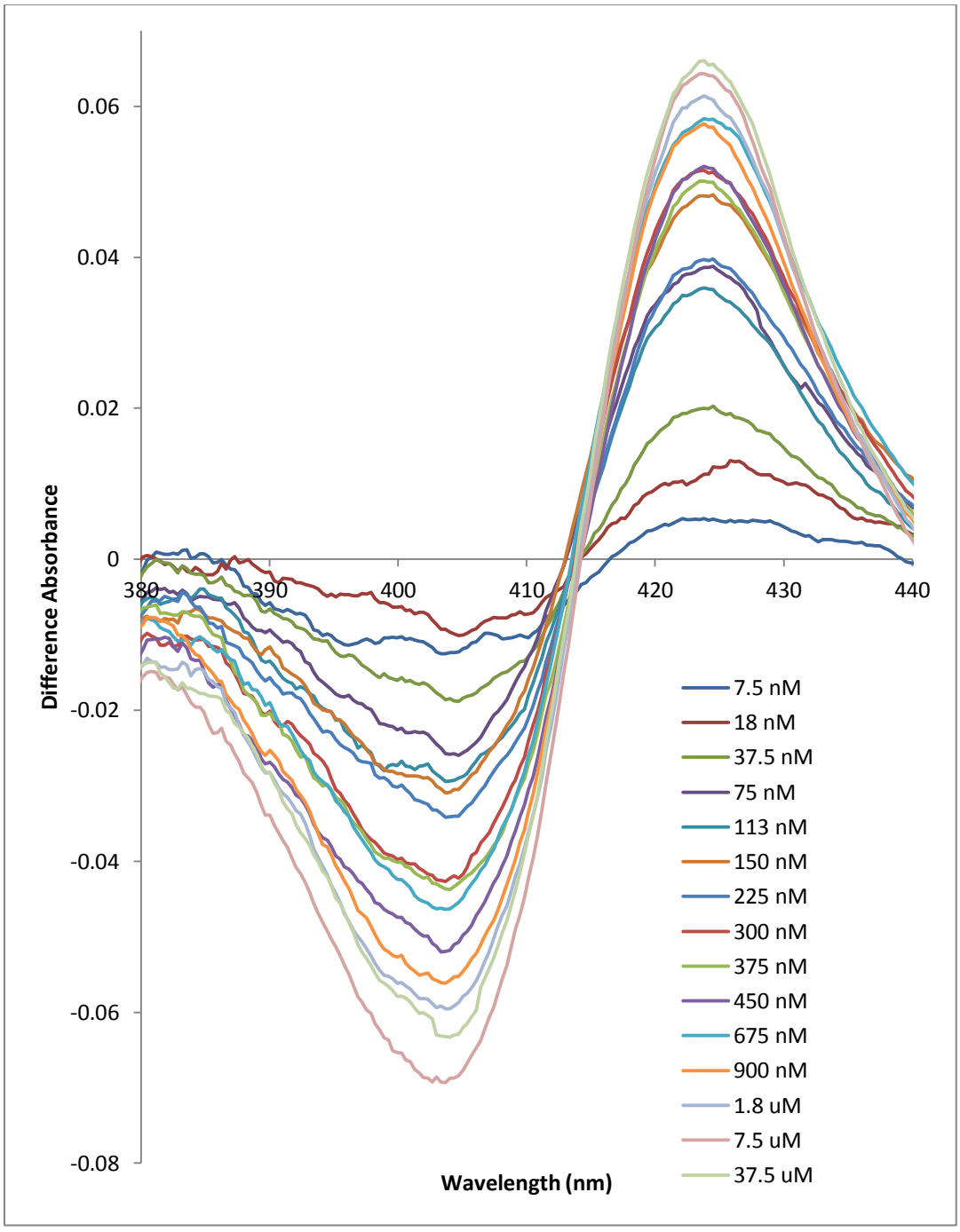

Figure 2.27. Trial 2 (Figure 2.20) difference absorbance spectra, 5 mM sodium acetate buffer, pH 5.00, was used.

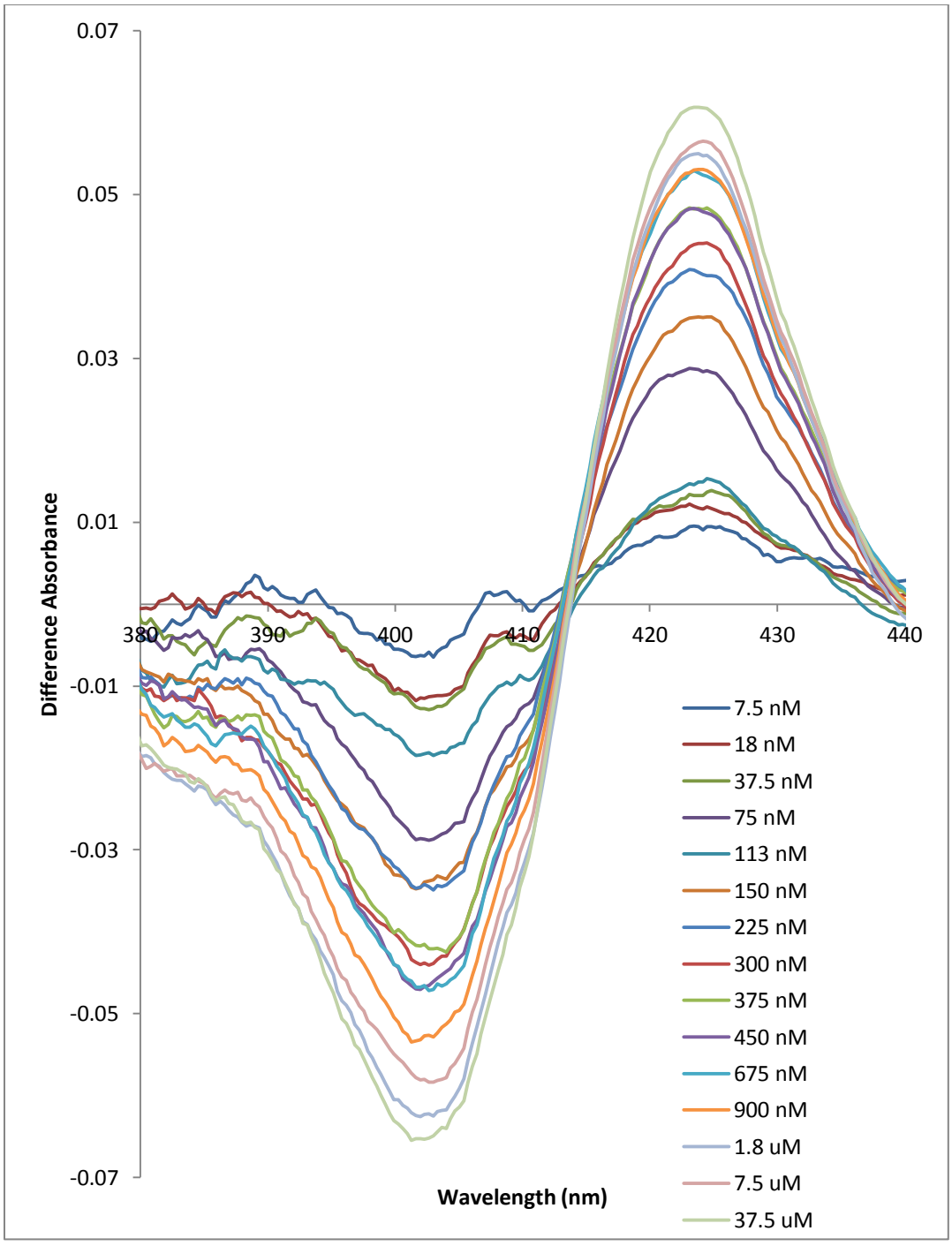

Figure 2.28. Trial 3 (Figure 2.22) difference absorbance spectra, 5 mM sodium acetate buffer, pH 5.00, was used.

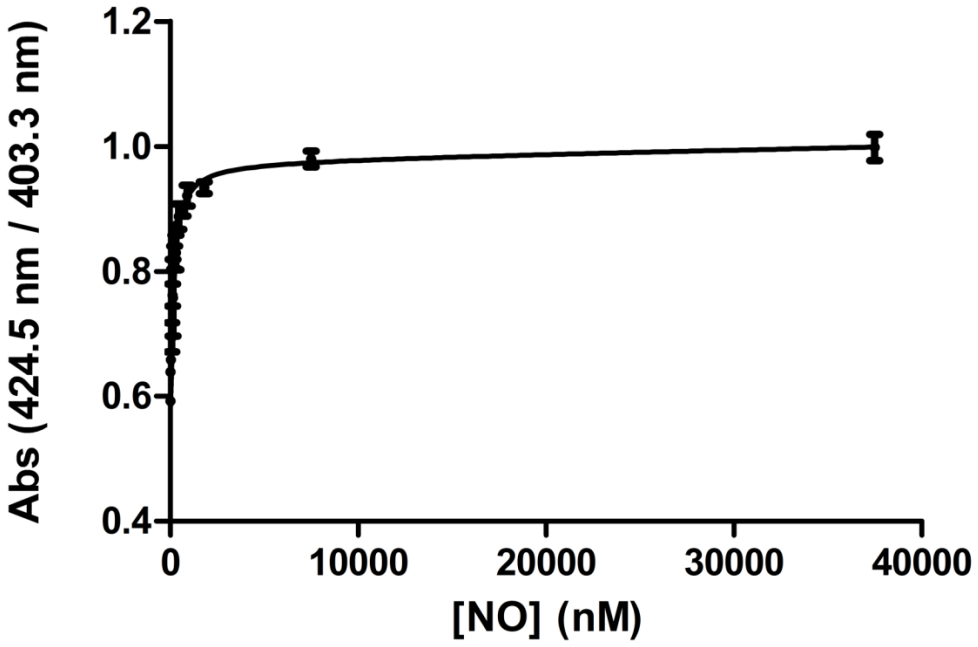

Figure 2.29. Binding curve of the NO sensor using NP4 NQN on an ATR waveguide platform. 1.5 molar equivalent NO to DEA/NO. 5 mM sodium acetate, pH 5.00, was used.

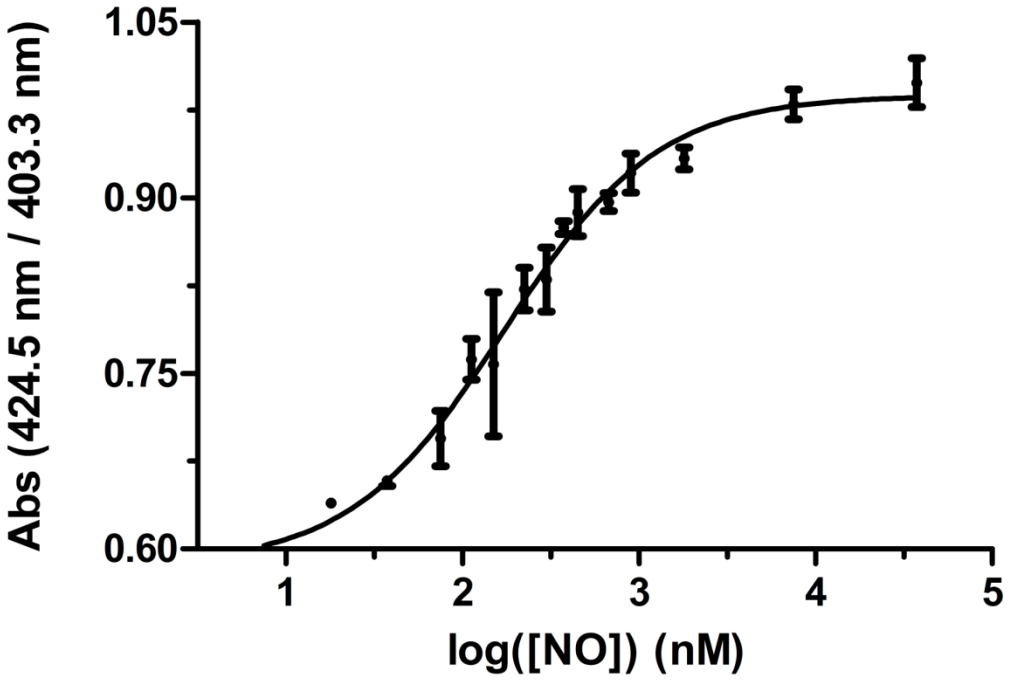

Figure 2.30. Binding curve of the NO sensor using NP4 NQN on an ATR waveguide platform on a log scale. 1.5 molar equivalent NO to DEA/NO. 5 mM sodium acetate, pH 5.00, was used.

these three trials, and the error bars represent the standard deviation. The linear portion of the binding curve can be seen in Figure 2.31.

The dissociation constant changed from 85 ± 3 nM in solution to 160 ± 20 nM bound to the surface of the ATR substrate. This is a decrease of ~ 50% of its binding strength, signifying a perturbation of the protein due to adsorption on the surface. The typical argument of ligand inaccessibility to the binding site is unlikely because an uncharged, diatomic ligand such as NO would likely be able to diffuse directly through the protein matrix. The most likely cause of the decreased activity upon adsorption are steric effects caused by the adsorption process on the heme pocket. Nitrophorins are very sensitive to the steric environment of the heme pocket, and small changes can result in large changed in K_d. Regardless of the decrease in binding efficacy, it remains that NP4 NQN is still active while adsorbed to the surface, which allows for its use as an effective NO sensor.

Another way to investigate the state of the protein is by examining the Soret band. Changes in the full-width half-max, i.e. the width of the band at half its maximal absorption, is indicative of changes in the chromophore. The solution full-width half-max of the unligated Soret band was 384 nm to 416 nm (32 nm) with a maximum at 403 nm (Figure 2.3). The adsorbed full-width half-max of the unligated protein is 386 nm to 428 nm (42 nm) with a maximum at 406 nm (Figure 2.20). As for the NO ligated Soret bands the solution full-width half-max was from 399 nm to 430 nm (31 nm) with a maximum at 419 nm, whereas the adsorbed protein full-width half-max was from 387 nm to 434 nm (47 nm) with a maximum at 416 nm. Hence there is broadening and a red shift

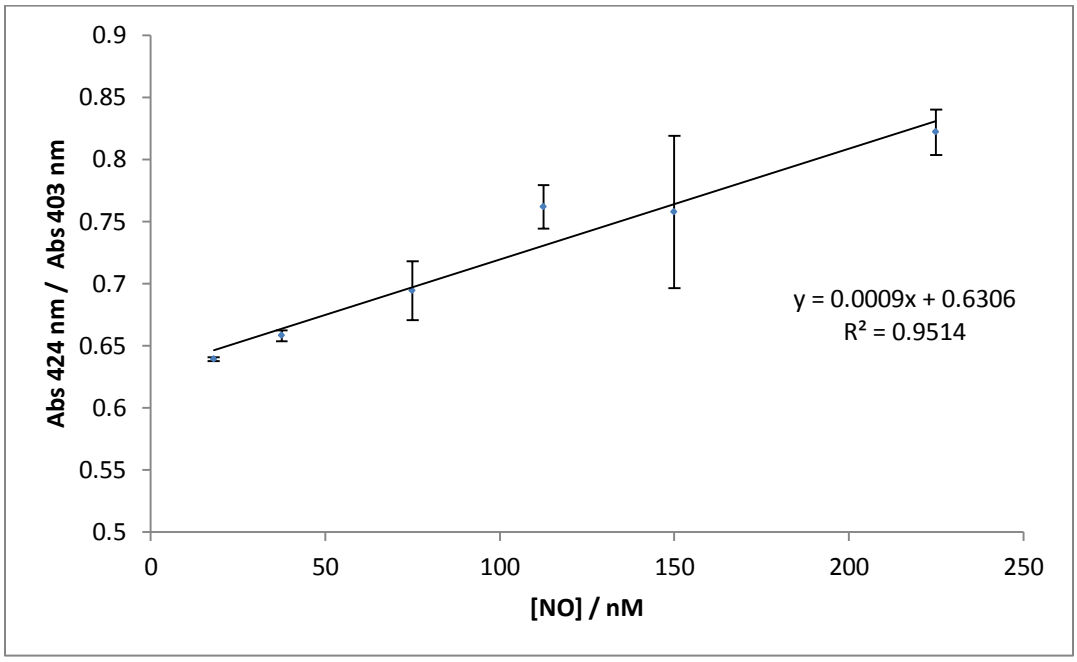

Figure 2.31. Linear portion of calibration curve from NO binding assay. 1.5 molar equivalent NO to DEA/NO.

in the unligated Soret band upon adsorption and it does not shift as much upon NO binding, while also being broader. This may be caused by a change in the rotational and/or vibrational states of the chromophore. Again, this is attributed to steric changes in the heme pocket caused by adsorption.

To compare the sensor among different conditions and experiments ratios of change in absorbance of the Soret band were calculated. The absorbance at the wavelength of maximal positive change in the spectrum was divided by the absorbance at the wavelength of maximal negative change. For example in the binding curve just described, the wavelength of maximal positive change was 424 nm, and the wavelength of maximal negative change was 403 nm, as identified in the difference spectra (Figures 2.25 – 2.28). For trial one, the unligated absorbance was 0.228 AU at 424 nm, and 0.390 AU at 403 nm, and their ratio is 0.586. The average ratio of the two absorbance values of the three trials at these two wavelengths was 0.59 for the unligated spectra, and was 0.82 for the concentration 225 nM NO (Table 2.1). Thus there was a 39% increase in the ratio of the wavelengths of maximal positive and negative change with the addition of 225 nM NO during the binding experiment. This concentration was chosen as the highest concentration in the linear portion of the binding curve to compare the ratio change among different experiments as described in subsequent sections.

2.c.11. Addressing possible interferents

To determine if the sensor would have interference from nitrite, nitrate or HNO,

Table 2.1. Summary of binding experiments. Ratios are those of the absorbance at maximal positive shift wavelength over the absorbance at maximal negative shift wavelength.

Experiment	Solution contents	λ of maximal negative shift (nm)	λ of maximal positive shift (nm)	Post injection ratio[1]	Pre injection ratio[1]	Ratio change of post inj. over pre inj.[2]
Binding Curve	225 nM NO in deaerated buffer	403	424	0.82 ± 0.02	0.59 ± 0.01	1.39 ± 0.03
Nitrate / Nitrite	1 μM NO_2^- 100 μM NO_3^-	403	424	0.44	0.44	1.00
HNO interference	5.6 μM Angeli's salt	393	420	0.58	0.51	1.13
Biological system	225 nM NO in buffer	396	417	0.57 ± 0.02	0.39 ± 0.03	1.44 ± 0.11
	225 nM NO in BSA solution	396	417	0.61 ± 0.03	0.46 ± 0.03	1.33 ± 0.11
	225 nM NO in Cell culture media	396	417	0.66 ± 0.06	0.58 ± 0.07	1.14 ± 0.17

[1]Ratio of absorbance at λ of maximal positive shift over absorbance at λ of maximal negative shift. [2]Ratio of the post injection ratio over the pre injection ratio.

each was injected into the sensor. Additionally degraded DEA/NO was tested for interference to ensure that the signal was from NO and not a by-product of the donor molecule.

For the nitrate and nitrite study, NP4 NQN (1.4 mg/mL) was injected in 5 mM sodium acetate buffer pH 5.00 into the flow cell and allowed to bind for 16 min on a piranha cleaned coverslip. 0.9 mL of a solution containing 100 μM nitrate and 1 μM nitrite in 5 mM sodium acetate pH 5.00 buffer was injected into the flow cell at a rate of 2-3 mL/min. A 1:100 spike of 10 mM NaOH was used in the buffer to provide consistency with experiments using DEA/NO and Angeli's salt, which raised the pH by 0.17 units. Spectra were acquired for 60 min (100 spectra for every time point, and 10 point running averaged).

During the HNO study, NP4 NQN (1.4 mg/mL) in 5 mM sodium acetate buffer, pH 5.00, was injected and adsorbed to a piranha cleaned coverslip for 17 min. The flow cell was then rinsed with 20 mL of the same buffer. Angeli's salt (2 mL of 540 nM) was injected into the flow cell in 5 mM sodium acetate buffer pH 5.00, spectra were collected for 15 min (100 spectra for each time point, and a 10 point running average was applied). The cell was rinsed with same buffer and injected 2 mL of 540 nM Angeli's salt injected in same buffer again and monitored for 22 min. This was repeated one additional time (data not shown). The flow cell was then rinsed with 10 mL of buffer followed by injection of 2 mL of 5.4 μM Angeli's salt in the same buffer. Spectra were collected for 15 min. All injections of Angeli's salt were at a rate of 2-3 mL/min.

Possible interferents for the assay include HNO, nitrite and nitrate. We demonstrate for the first time to our knowledge the reaction between HNO and nitrophorin. The addition of HNO did cause a small shift in the Soret band at 540 nM Angeli's salt (Figures 2.32, 2.33, Table 2.1). It has been shown that ferric proteins are reduced to ferrous and bind NO when reacted with HNO,[84] which is likely the case here. However 5.4 μM Angeli's salt did cause a marked shift in the Soret band (Figures 2.34, 2.35). There was a change in the ratio of maximal shifts of 13% (Table 2.1). This indicates a possible interferent for the assay, although it is not known with certainty if HNO exists endogenously. If HNO is present it is likely to be in much lower concentrations than those examined, and would then present little to no actual interference.

Nitrite at 1 μM, and nitrate at 100 μM, which is at least 2 times fasting plasma levels,[31] did cause a small decrease in the overall absorbance of the Soret peak, but not a shift (Figure 2.36). The ratio of change in the nitrite/nitrate interference experiment was identical before and after the injection of 100 μM nitrate and 1 μM nitrite (Table 2.1). The lack of interference is significant because nitrite is an interferent in many other methods of NO detection. Degraded DEA/NO (in solution) was also tested for binding to NP4 NQN as a control in a cuvet and shown not affect the spectrum (Figure 2.37, Table 2.1).

2.c.12. Assessing the sensor in the presence of oxygen

To address the possibility that the binding assay could be affected by the presence

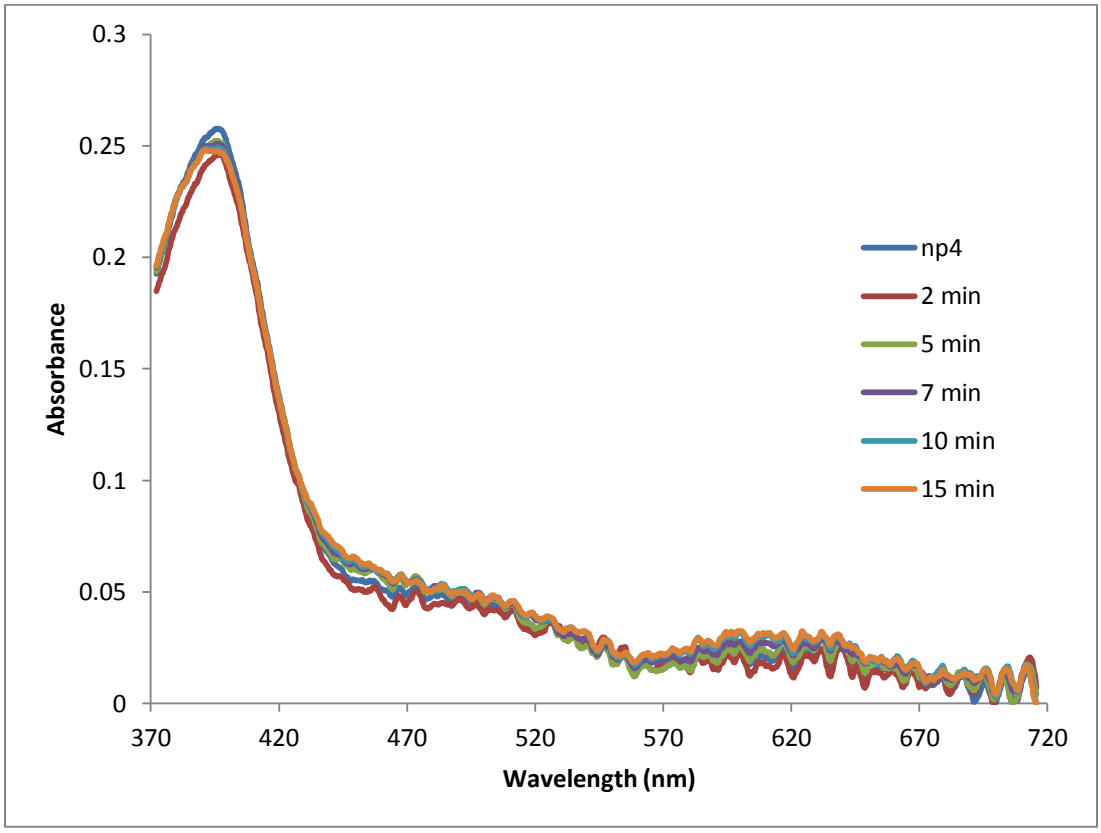

Figure 2.32. ATR absorbance spectra after the addition of 540 nM Angeli's salt (AS) the NP4 NQN sensor in 5 mM sodium acetate buffer, pH 5.00. Time-points post injection of AS.

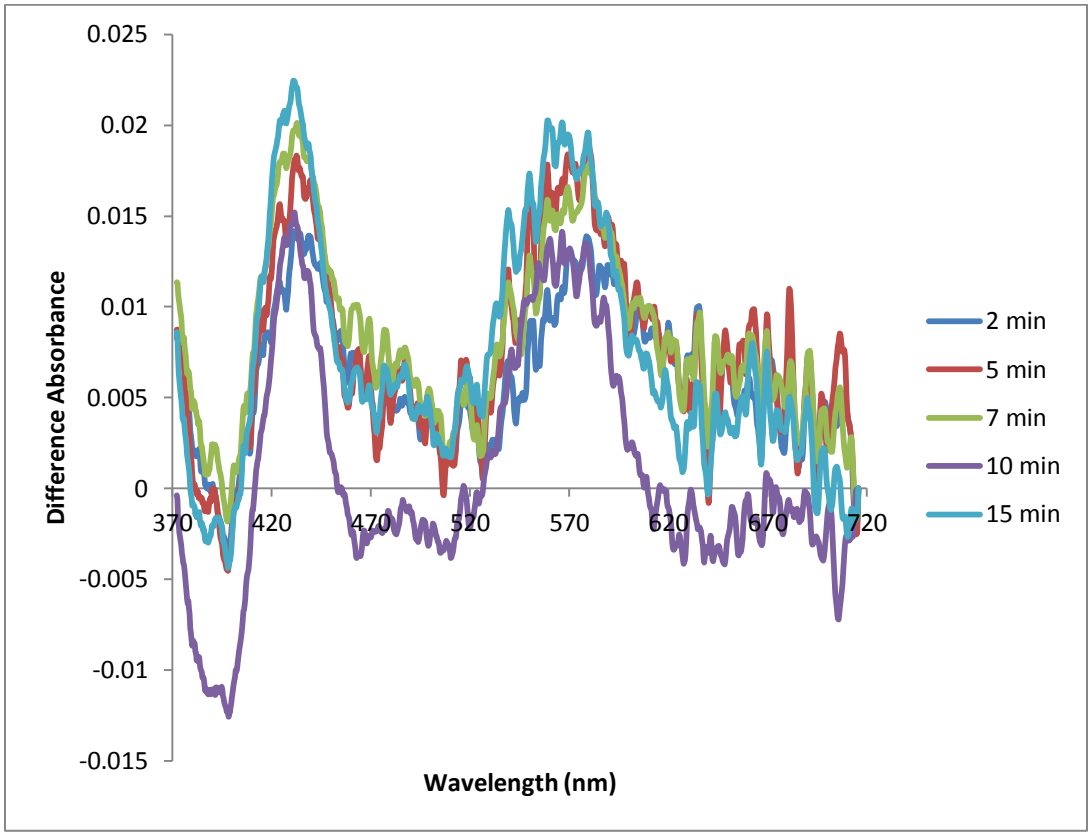

Figure 2.33. Difference absorbance spectra of 540 nM Angeli's salt (Figure 2.32).

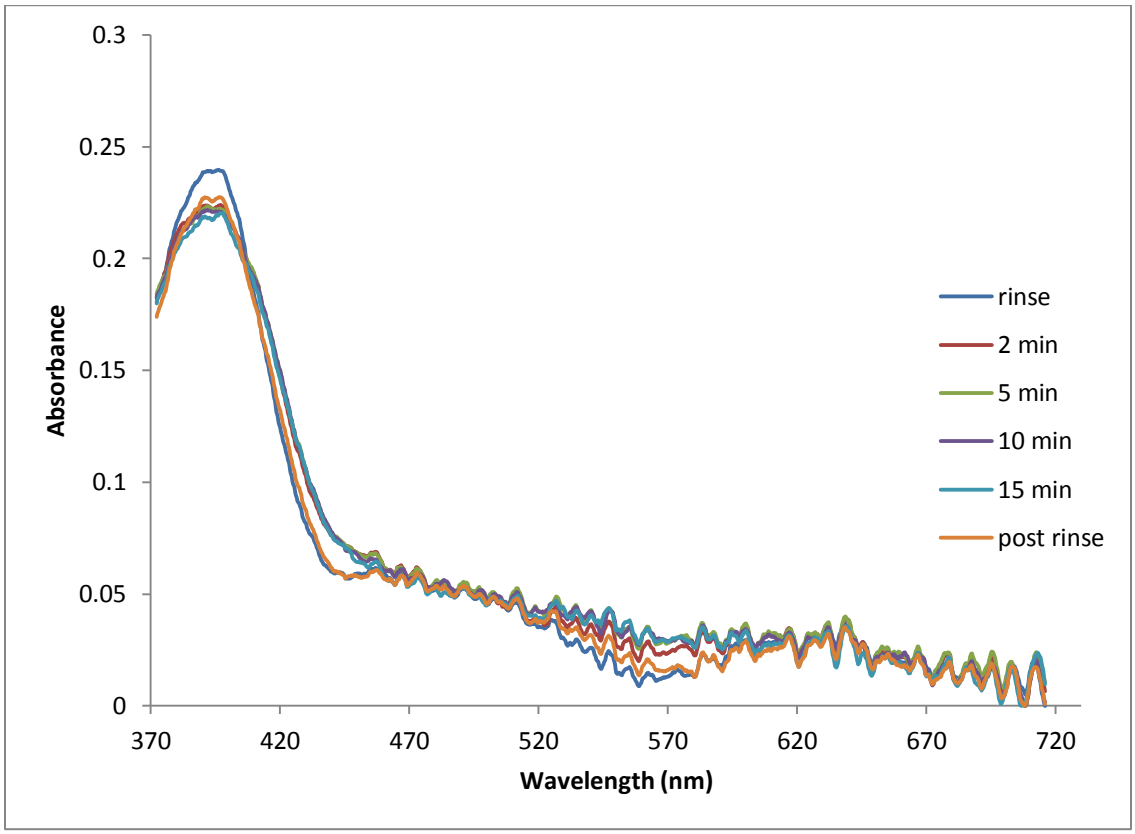

Figure 2.34. ATR absorbance spectra after the addition of 5.4 μM Angeli's salt (AS) to the NP4 NQN sensor, in 5 mM sodium acetate buffer, pH 5.00. Time-points post injection of AS.

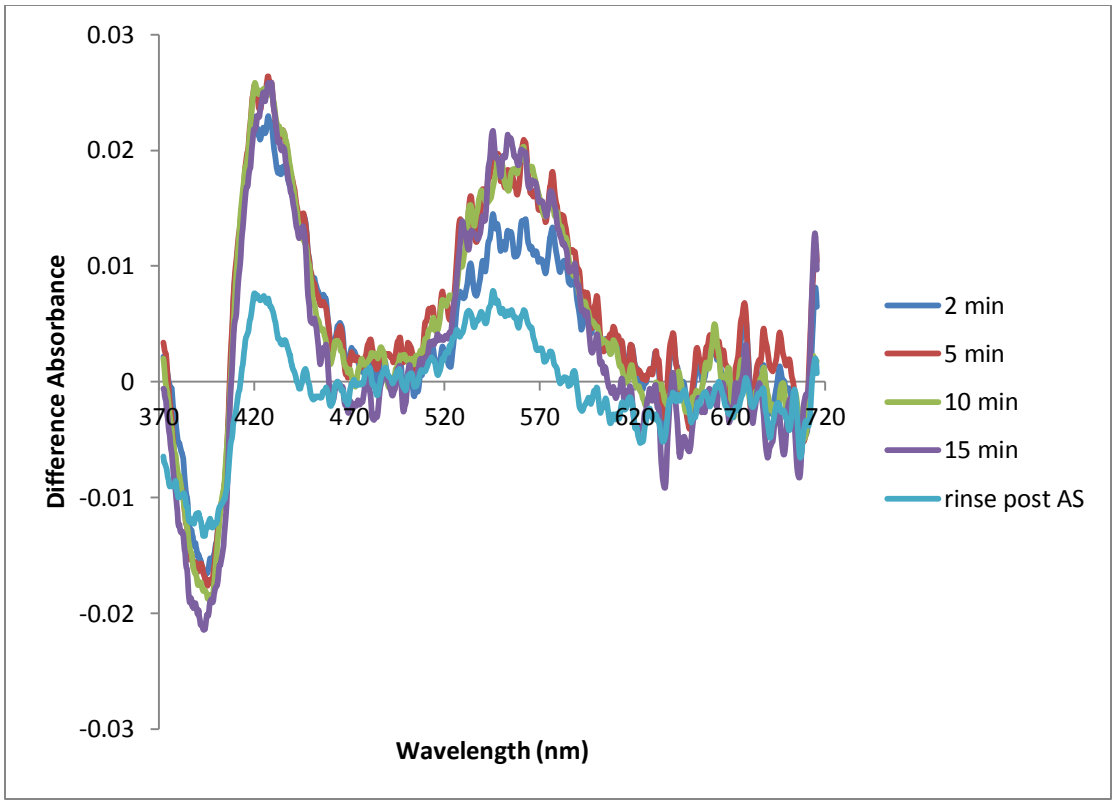

Figure 2.35. Difference absorbance spectra post injection of 5.4 μM Angeli's salt (Figure 2.34).

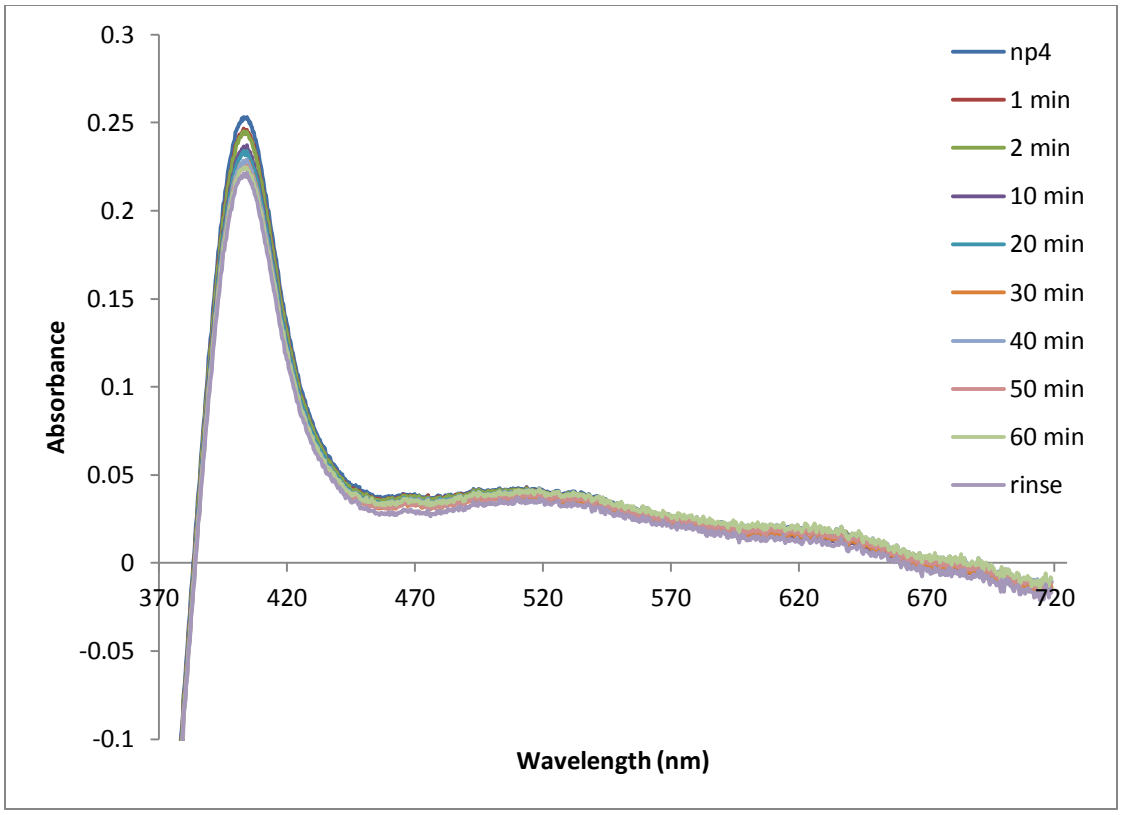

Figure 2.36. ATR absorbance spectra after a solution of 100 μM nitrate, 1 μM nitrite, in 5 mM sodium acetate buffer, pH 5.00, was injected into the NP4 NQN sensor. Time points are post injection.

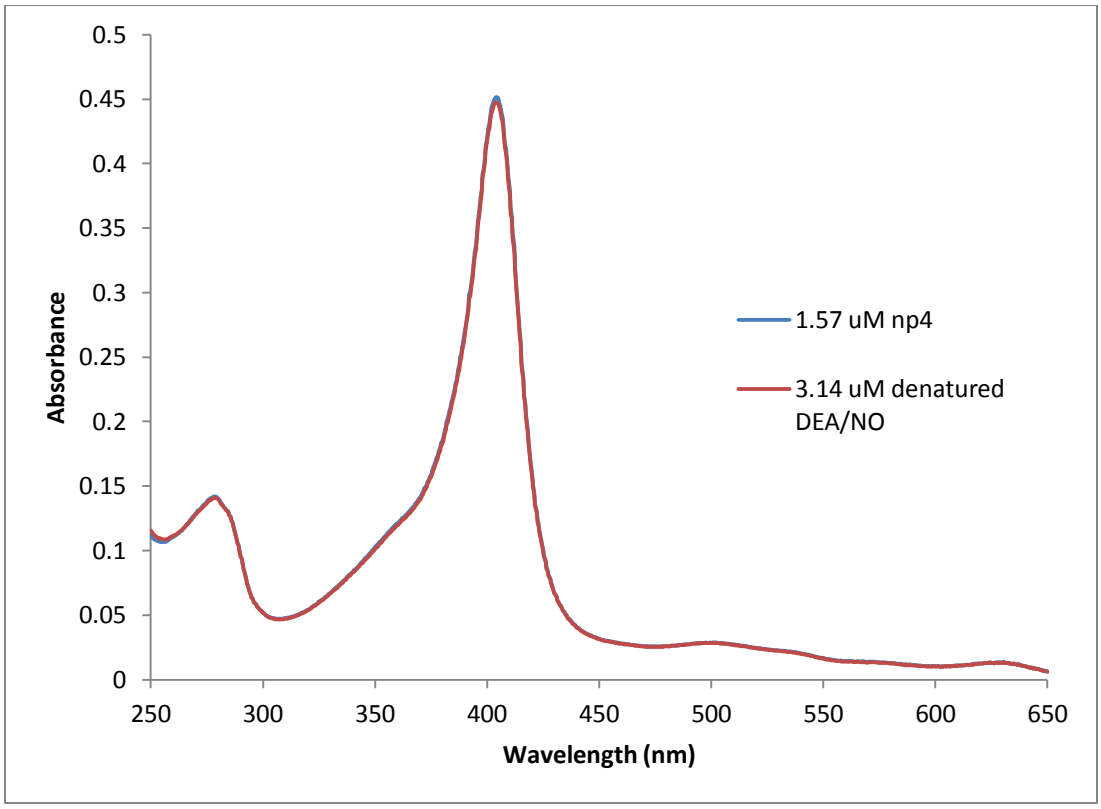

Figure 2.37. Solution spectra of NP4 NQN with the addition of degraded DEA/NO, in solution.

of oxygen in the buffer, a 225 nM NO solution was flowed through deaerated (Figures 2.38 and 2.39) and non-deaerated buffers (Figures 2.40 and 2.41), three times each. NP4 NQN (1.4 mg/mL) was injected and adsorbed to a piranha cleaned coverslip for 18 min. The flow cell was then rinsed with 20 mL of deaerated 5 mM sodium acetate buffer, pH 5.00. 2 mL of 225 nM NO was injected into the flow cell in non-deaerated 5 mM sodium acetate pH 5.00 buffer at a rate of 2-3 mL/min. After each injection one min was allowed for equilibration before the spectra were taken. Spectra were acquired and averaged (100), and a 10 point running average was performed. The flow cell was then rinsed with 20 mL of 5 mM Tris, pH 7.5, to remove the bound NO and regenerate the sensor. Then the flow cell was rinsed with 20 mL of deaerated 5 mM sodium acetate buffer, pH 5.00, followed by 2 mL of 225 nM NO in the same buffer at a rate of 2-3 mL/min. This was repeated two more times.

There was no difference observed between the two buffers, and the ratios of the percent change were identical within the error of the experiment (Table 2.2). There was a concern because NO reacts with oxygen. The fact that there is no discernible difference between the two solutions is not entirely surprising because the half-life of NO at this concentration is ~3700 s in aerated buffer.[15] This is important because when the sensor is used with biological samples it will always contain oxygen. The deaerated solutions were used to get an absolute limit of detection with no other known interferences present in solution.

These results are plagued by a large absorption band centered at 515 nm. The nature of this band is unknown but was observed occasionally with sGC as well. It is

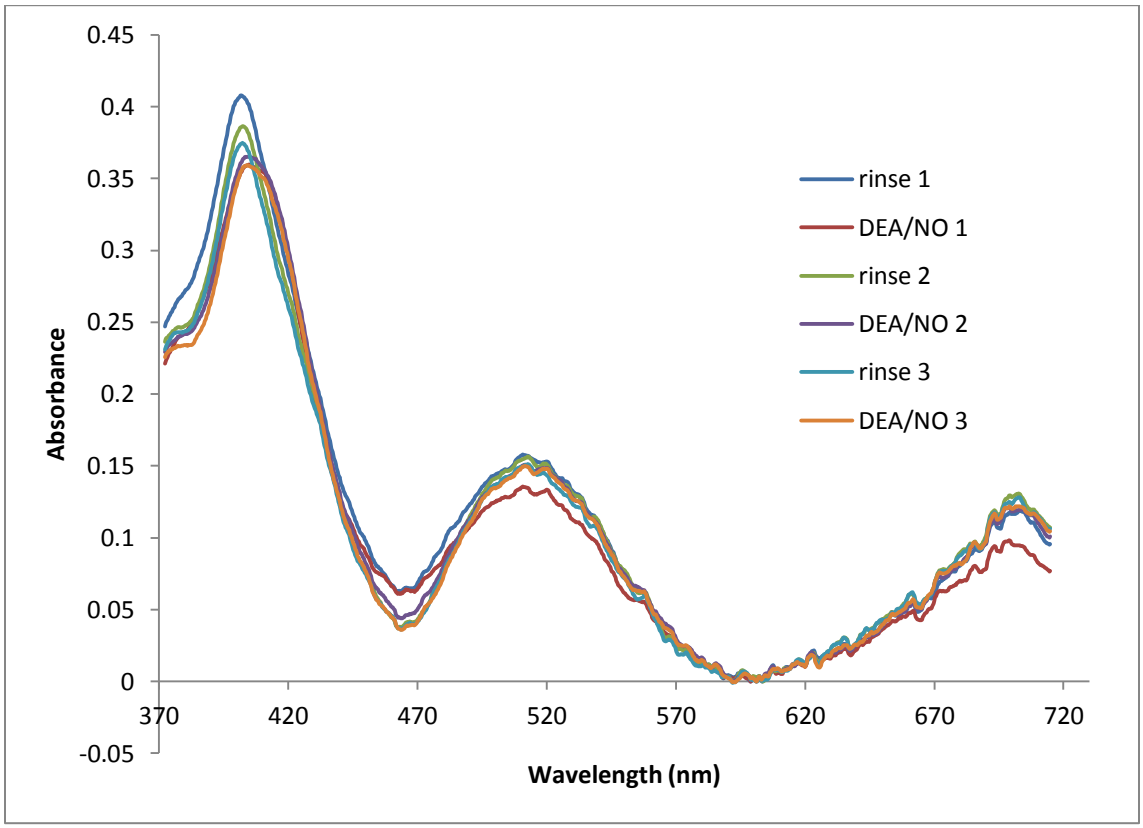

Figure 2.38. ATR spectra of three trials of 150 nM DEA/NO injected into sensor using deaerated 5 mM sodium acetate buffer, pH 5.00.

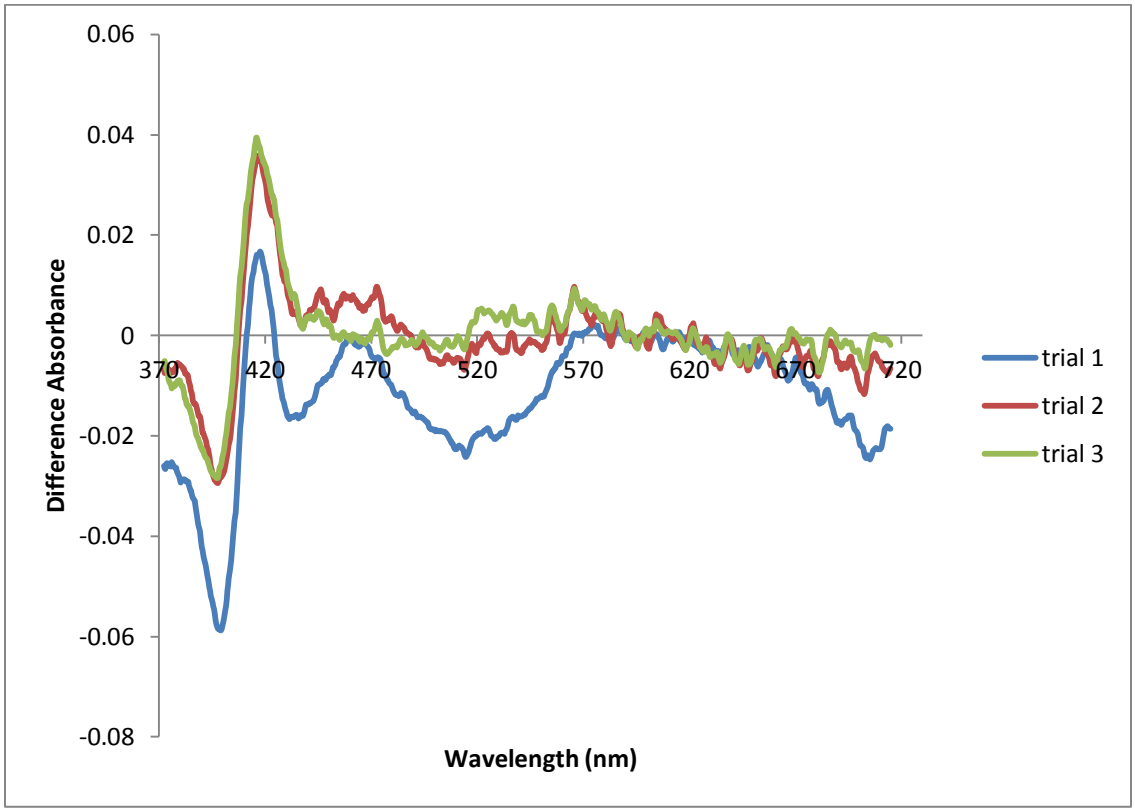

Figure 2.39. Difference absorbance spectra from Figure 2.38.

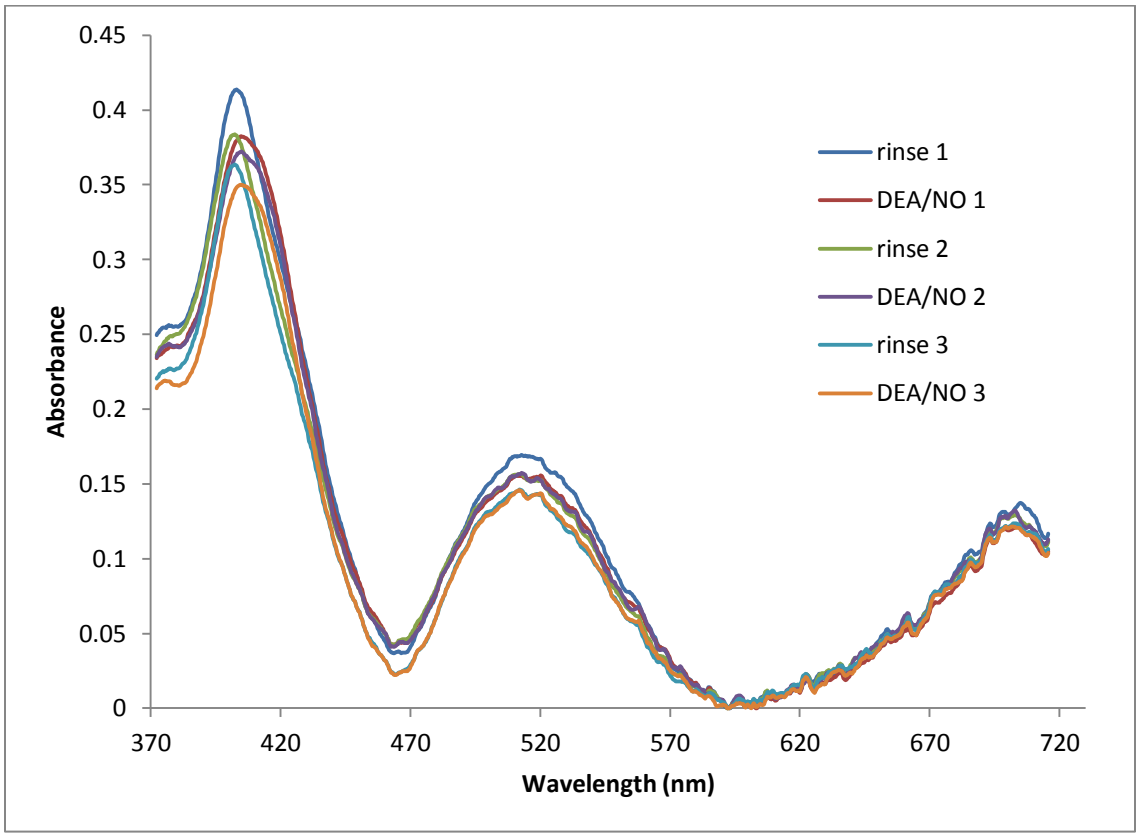

Figure 2.40. ATR spectra of three trials of 150 nM DEA/NO injected into the NO sensor in non-deaerated 5 mM sodium acetate buffer, pH 5.00.

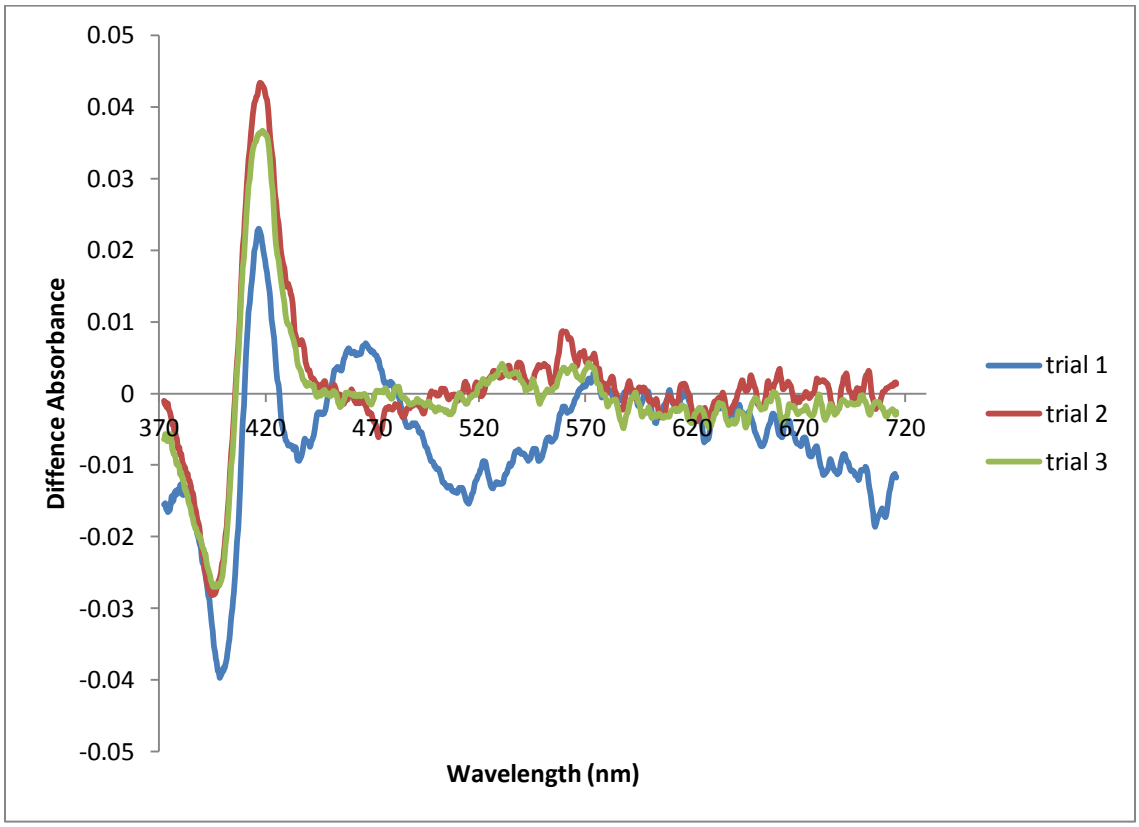

Figure 2.41. Difference absorbance spectra from Figure 2.40.

Table 2.2. Results from deaerated experiment and binding assay. Ratios are based on the absorbance at the maximal positive shift wavelength divided by the absorbance at the maximal negative shift wavelength.

Experiment	Solution contents	λ of maximal negative shift (nm)	λ of maximal positive shift (nm)	Post injection of 150 nM DEA/NO ratio[1]	Pre injection ratio[1]	Ratio of post inj. over pre inj.[2]
Binding Curve	225 nM NO in deaerated buffer	403	424	0.82 ± 0.02	0.59 ± 0.01	1.39 ± 0.03
Effect of buffer	225 nM NO in deaerated buffer	398	416	0.988 ± 0.001	0.80 ± 0.01	1.23 ± 0.03
	225 nM NO in non-deaerated buffer	398	416	1.00 ± 0.01	0.82 ± 0.02	1.22 ± 0.03

[1]Ratio of the absorbance at the wavelength of maximal positive shift over the absorbance at the wavelength of maximal negative shift. [2]Ratio of the post injection ratio of absorbances divided by the pre injection ratio of absorbances.

such a prominent band at such an unexpected place in the spectrum that it is presumed that it represents some type of chemical change in the chromophore of the protein. Data generated in this section must be repeated before conclusions are clear. Nonetheless, NO was clearly demonstrated to bind to NP4 NQN in this state. However, there was not as much of a change in the Soret as compared to the binding experiment or results presented in the following section. In fact the shift in the Soret band was reduced by almost 50% as compared to the binding assay, as indicated by the ratios of the pre and post NO shift (Table 2.2). The possible interference of oxygen was addressed below, where the control of the BSA and cell culture solutions was not deaerated, and had the same shift in the Soret band as in the deoxygenated buffer during the binding experiment (Table 2.1).

2.c.13. NO detection in BSA and cell culture solutions

The sensor was utilized in a manner consistent with a representative biological sample. This included a highly concentrated BSA solution approximating tissue perfusate, and cell culture solution containing 10% fetal bovine serum, representing cell culture measurements.

2 mL of 40 mg/mL BSA solution in 5 mM sodium acetate pH 5.00 buffer for 20 min to block the surface. The flow cell was then rinsed with 20 mL of 5 mM Tris pH 7.50 buffer followed by 20 mL of 5 mM sodium acetate buffer pH 5.00. 2 mL of 225 nM NO in 5 mM sodium acetate buffer pH 5.00 was then injected. The flow cell was rinsed with 20 mL of 5 mM Tris pH 7.50 followed by 20 mL of 5 mM sodium acetate buffer pH 5.00. This was repeated 2 more times. Then 2 mL of 225 nM NO in 5 mM sodium

acetate pH 5.00 buffer that contained 40 mg/mL BSA was injected following the same procedure three times. Finally, 2 mL of 225 nM NO was injected in modified DMEM cell culture media (Gibco; high glucose, no phenol red, sodium pyruvate or glutamine), adjusted to pH 5.00, and containing 10 % fetal bovine serum. Three trials were performed. One minute was allowed prior to injection of DEA/NO solution. Injections were at a rate of 2-3 mL/min. One min was allowed for NO equilibration after injection prior to spectral acquisition. 100 spectra were averaged, and a 10 point running average was used to smooth the spectra.

A 225 nM NO solution in 40 mg/mL BSA, 5 mM acetate buffer, pH 5.00, was used to test if the presence of serum concentrations of BSA would interfere with the sensor's ability to detect NO (Figures 2.42 and 2.43). This was repeated a total of three times and compared to 5 mM sodium acetate buffer pH 5.00 alone (Figures 2.44 and 2.45). BSA produced slightly less change than did NO in acetate buffer but the change was still evident (Table 2.1). This is not surprising because the presence of BSA causes a break in the reaction pathway between NO and nitrogen dioxide and therefore increases the half-life of NO in solution.[15] This would indicate the utility of the sensor in tissue perfusate or serum NO quantification applications where the vast majority of the soluble protein is serum albumin. One min was allowed to pass after DEA/NO was injected before spectra were acquired. Spectra were averaged (100 for each acquisition) and a 10 point running average was applied.

As a final test of the utility of the sensor, modified DMEM cell culture media containing 10% FBS (pH adjusted to 5.00) was spiked with 150 nM DEA/NO and

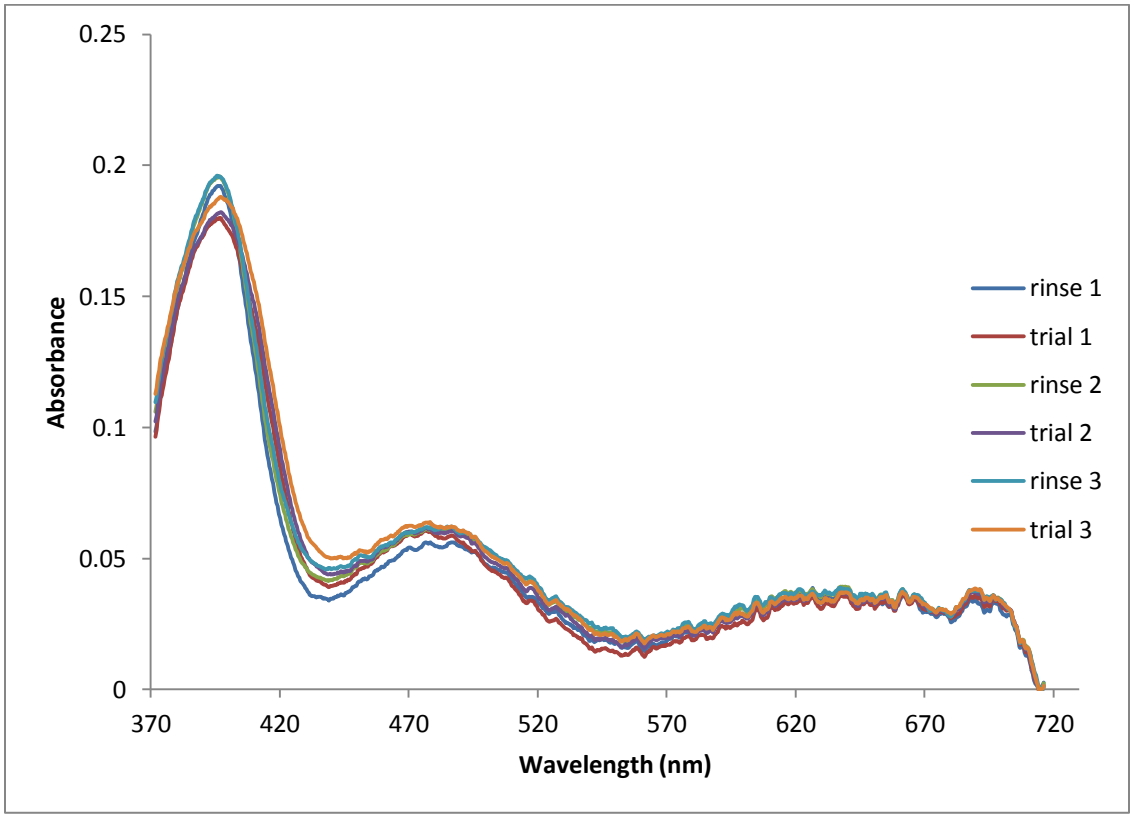

Figure 2.42. ATR absorbance spectra of three trial of 225 nM NO in 40 mg/mL BSA, 5 mM sodium acetate buffer, pH 5.00, was injected into the NO sensor.

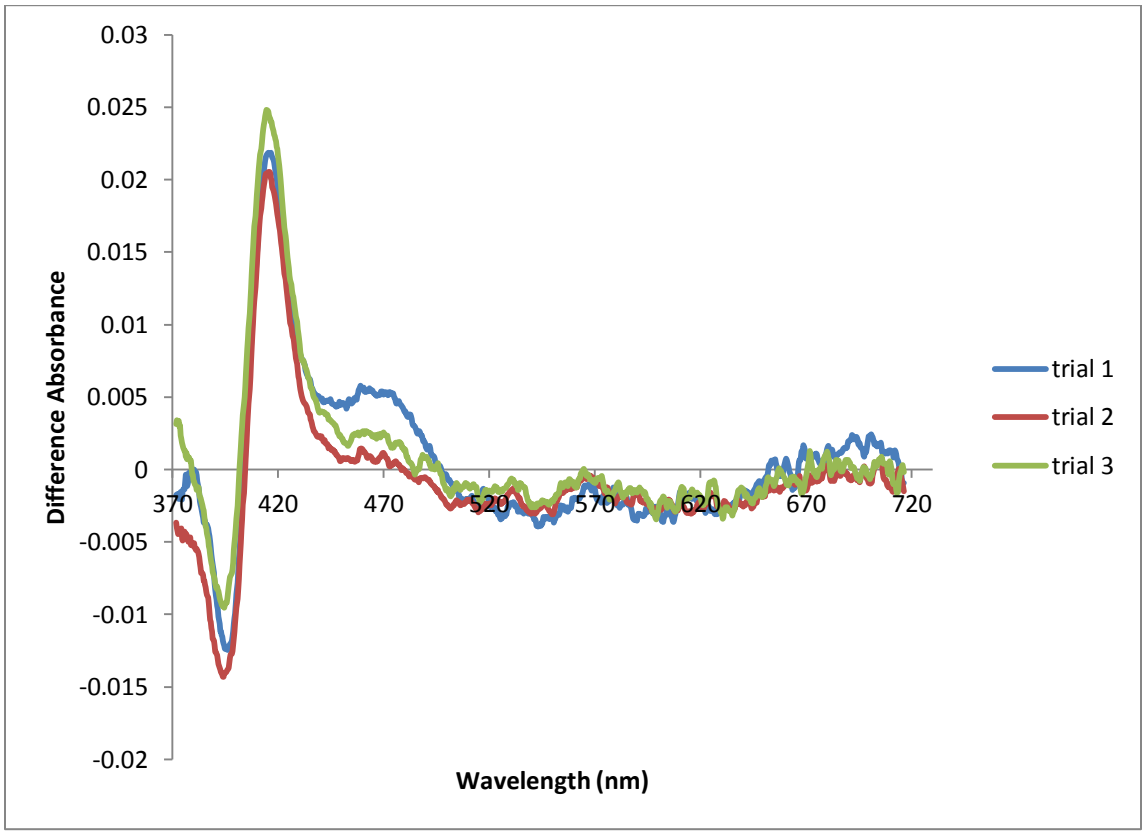

Figure 2.43. Difference absorbance spectra from Figure 2.42.

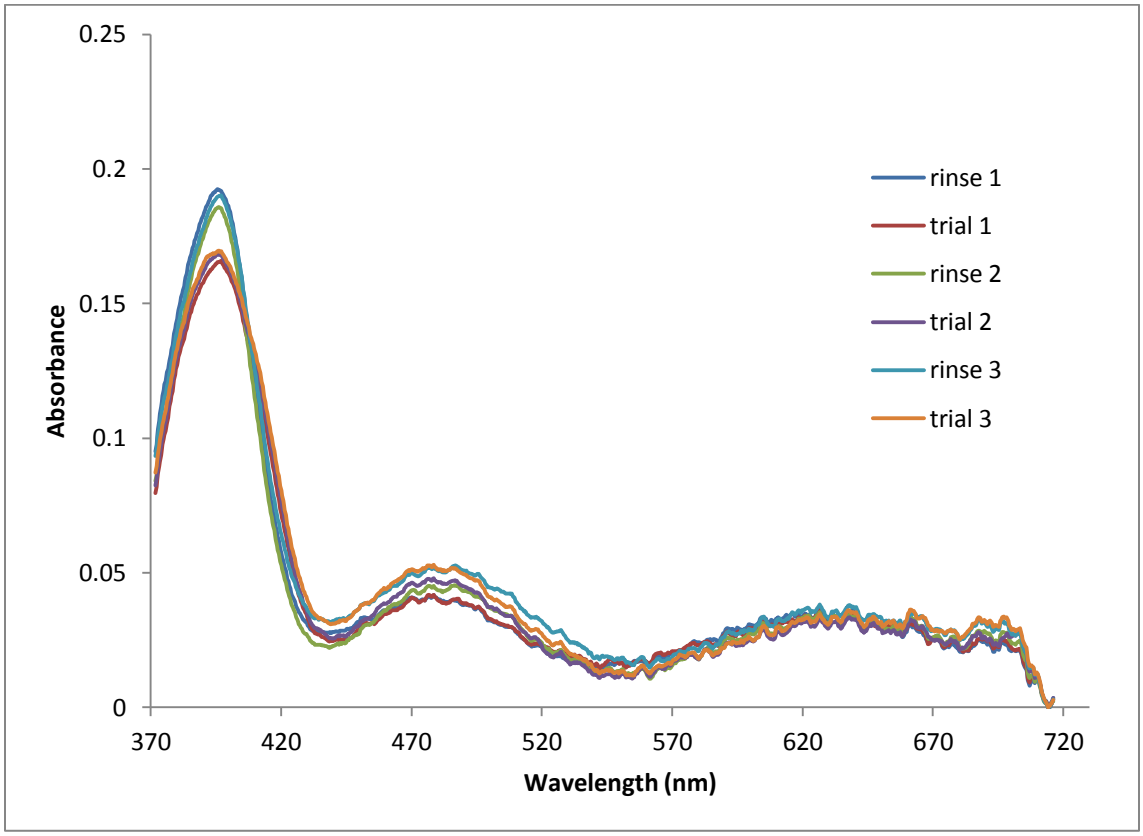

Figure 2.44. ATR spectra of three trials of 225 nM NO in 5 mM sodium acetate buffer, pH 5.00, was injected into NO sensor.

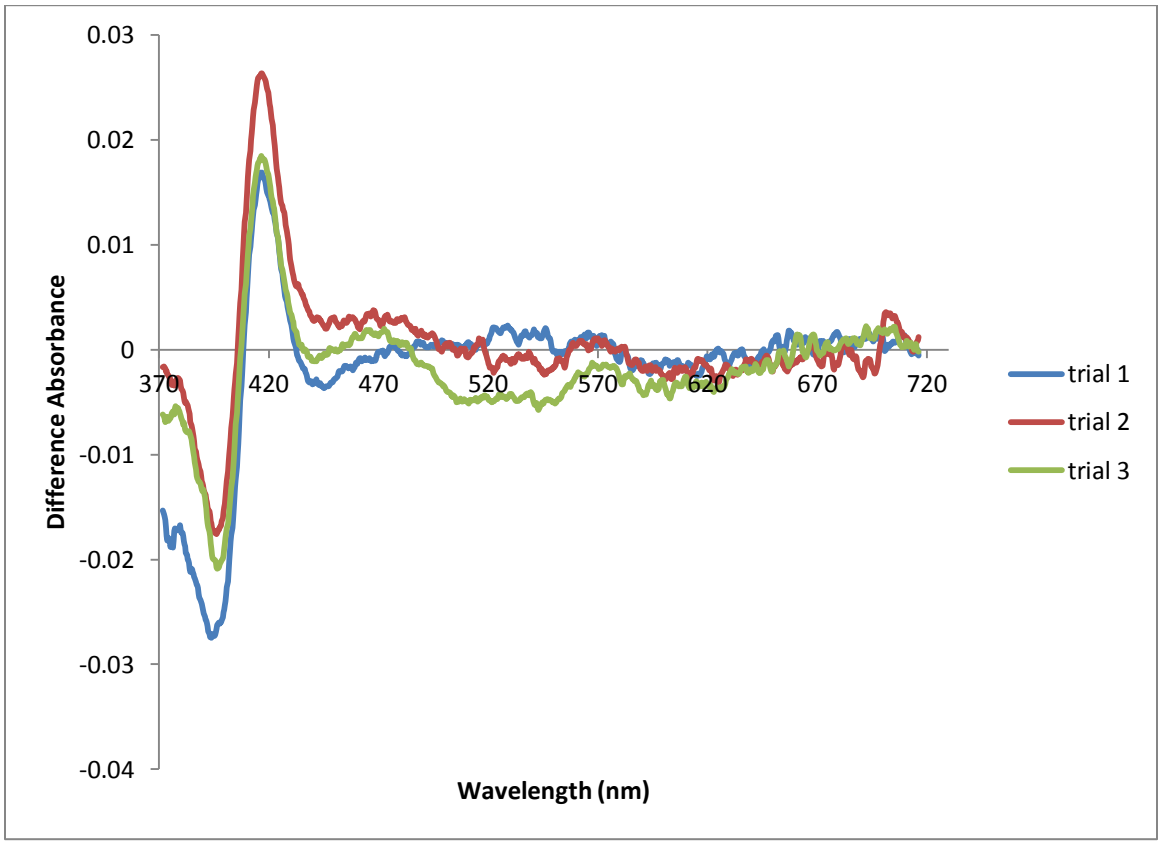

Figure 2.45. Difference absorbance spectra from Figure 2.44.

injected into the sensor. It was successful in detecting NO three consecutive times (Figures 2.46 and 2.47). The DEA/NO produced a significantly smaller shift than the control (Figures 2.44 and 2.45) but was still notable. This experiment demonstrates the sensors utility to detect NO in such complex mixtures as cell culture solutions.

The relatively high error (Table 2.1) is likely due to a slight change in the wavelength of maximal change with each trial shifting from 410 nm to 414 nm over the three trials, and the smaller change in absorbance than the buffer alone (Figures 44 and 45). Also of note, the first trial produced a ratio of the post and pre NO injection of 1.19, and the following trials had lower ratios that may indicate something is happening to the protein over time. There appears to be a shift in the spectra with each trial, with the absorbance increasing around 430 nm. This may indicate a reduction of the iron in the heme group as that is where Fe^{2+} heme would absorb. It could also be some other type of degradation of the protein. However, the sensor is clearly functioning, as indicated by the difference spectra in Figure 47, since there is still a significant change with the injection of each NO solution. The error associated with the cell culture media experiment is in line with the errors of the other two experiments done on this film, the BSA solution and the control, which also have errors that were on the same order as compared to previous experiments (Table 2.1). This indicates that there may be some mechanical or chemical instability with this particular protein film.

Also of note in this experiment is that the control buffer was not deoxygenated and still provided the same ratio of change in the Soret as deoxygenated buffer (Table 2.1), indicating oxygen has no effect on the sensor.

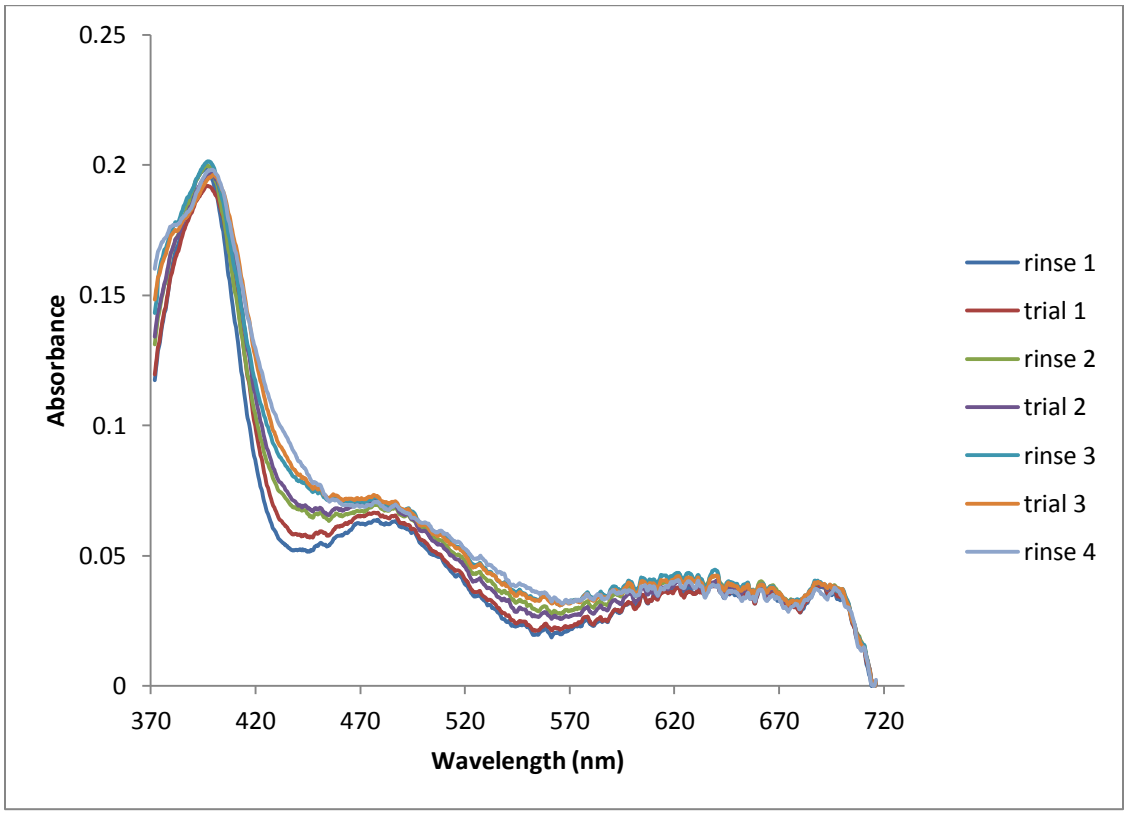

Figure 2.46. ATR absorbance spectra of three trials of 225 nM NO in DMEM cell culture media containing 10% fetal bovine serum was injected into the NO sensor.

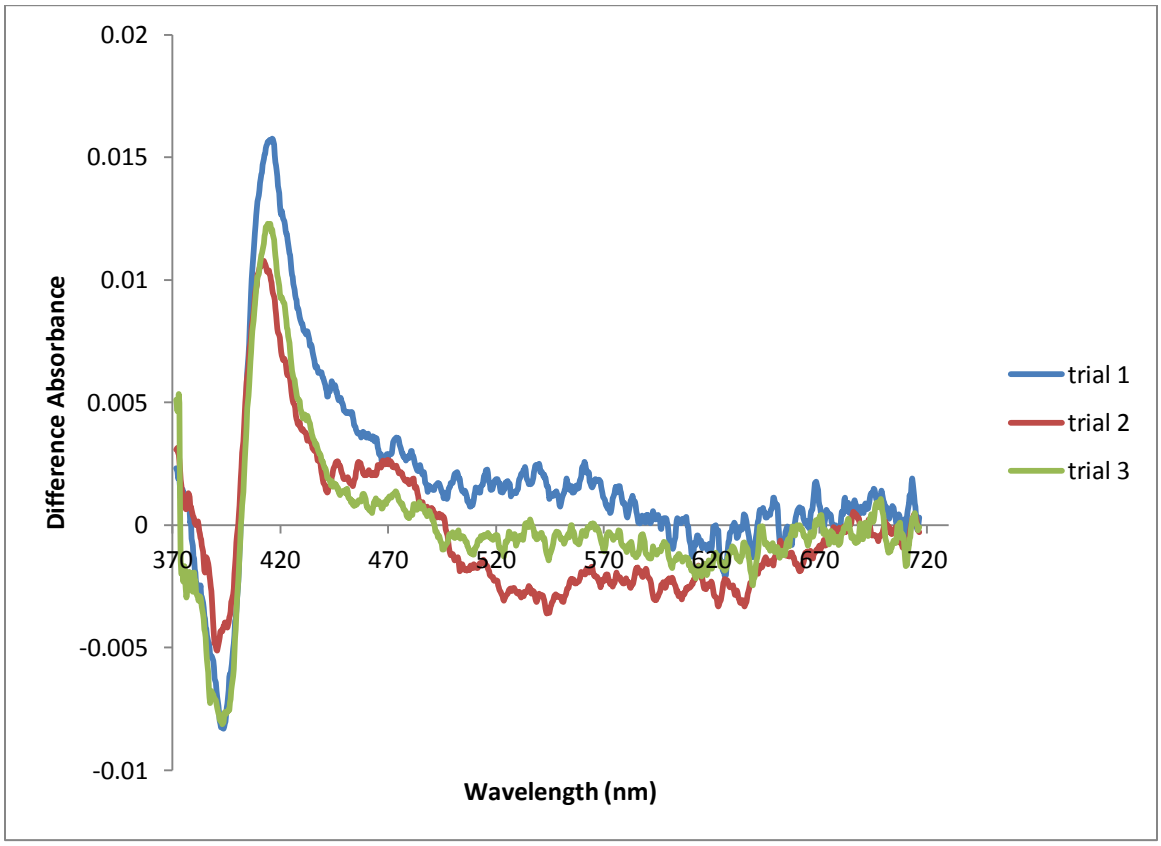

Figure 2.47. Difference absorbance spectra from Figure 2.46.

2.d. Conclusions and future directions

This is a novel sensor in that it provides the direct detection of nitric oxide, rather than a product of nitric oxide degradation. The reusability is demonstrated and the stability is significant as shown, but presumably could be improved with covalent attachment of the protein to the surface of the coverslip. The detection limit demonstrated here is immediately applicable to certain biological applications, such as NO production from macrophages and possibly tissue perfusate experiments. Future investigations will address this issue as it applies directly to biological samples. If fouling of the sensor occurs due to the biological samples, the protein film could be encapsulated in a gas permeable polymer such as PEG or a fluorosilane.

The detection limit could also be lowered by possibly nearly 2 orders of magnitude by using NP2 or NP7 instead of NP4 NQN, where the binding constant of two former proteins is approximately 2 orders of magnitude lower than NP4 NQN at ~1 nM versus ~100 nM for the protein studied.[62] Using these proteins could potentially bring the detection limit down from 18 nM found in this study to 180 pM. Knipp and coworkers also showed that a mutant NP 7 Δ 1-3 has nearly the same binding at pH 7.5 as pH 5.0,[62] which could be employed in this sensor to operate at physiological pH. Also of note is the ferrous form of NP4, which has a K_d of ~50 fM.[85] This state was achieved upon reduction with sodium dithionite (Figure 2.15). Ferrous NP4 is unstable and would require continuous presence of reducing agent or to be adsorbed on a transparent conductive electrode and reduced electrochemically.

CHAPTER 3

TEM IMAGING OF SOLUBLE GUANYLATE CYCLASE FRAGMENTS

3.a. Introduction

3.a.1. Nitric oxide

Nitric oxide is used by animals to regulate processes as diverse as the cardiovascular system,[4] central nervous system[5] and immune response.[7] The primary receptor for NO is soluble guanylate cyclase (sGC),[13] which catalyzes the conversion of guanosine triphosphate to cyclic guanosine monophosphate (cGMP).[86] Upon binding NO, the activity of sGC increases by nearly 200 fold over basal levels.[77] cGMP is responsible for many of the downstream physiological effects of NO.[86]

3.a.2. Soluble guanylate cyclase

Despite much effort in crystallizing sGC by the Montfort group and many others, the full three dimensional structure of sGC remains unknown. sGC is an ~150 kDa heterodimer of two similar subunits, known as α and β.[13] There is a ferrous heme group on the β subunit, which is the known binding site of NO. sGC is also known to bind CO in vitro as well as a synthetic allosteric regulator YC-1, and BAY 41-2271.[87-89] The binding of CO increases catalytic activity nominally, ~5 times above basal levels. YC-1 binding has been shown to increase the catalytic activity of the CO ligated enzyme to approximately that when NO is ligated.[88, 90]

Both α and β subunits of sGC contain an N-terminal H-NOX (Heme-Nitric oxide/OXygen) domain, PAS (periodic circadian protein, aryl hydrocarbon receptor nuclear translocater protein, single-minded protein; Per-Arnt-Sim) domain, coiled-coil region and C-terminal catalytic domain, based on homology models.[13] Domain structures predicted from homologous protein structures, mostly from bacteria. Domain organization is unknown. Parts of the protein structure have been solved from using protein for a variety of organisms, but much remains to be known about the structure and mechanism. Our lab has developed an *E. coli* expression system for sGC from the insect *Manduca sexta* (msGC). Many of these constructs are ~90 kDa and contain the HNOX, PAS and coiled-coil regions on α and β subunits, thus they are missing the α and β cyclase domains and henceforth are no longer catalytically active. However, these constructs do maintain their affinity for NO, CO and the synthetic ligand YC-1, and therefore can be studied spectroscopically.[13, 77]

We have imaged fragments of msGC in an effort to create a three-dimensional reconstruction of msGC using electron microscopy. The goal was to begin understanding overall shape and domain arrangement of the molecule, and describe any noticeable differences upon NO binding. The reconstructed protein with addition and deletion of each domain would yield a domain configuration of sGC that would be within the capabilities of this study. Also, three dimensional reconstruction of the protein with and without NO bound could characterize the conformational changes that occur during ligand binding. These findings could shed light on the mechanism of NO action on sGC,

and this could be further expanded to YC-1 and other allosteric regulators of sGC, which would lead to a better understanding of how sGC works.

3.a.3. Solving the structure of proteins with transmission electron microscopy

Transmission electron microscopy (TEM or EM) has gained much interest in the structural biology community.[91] It has advantages over x-ray crystallography, in that only small quantities of protein are required, and there is no requirement for crystallization. Typically the concentration of protein solutions for crystallography are in the millimolar concentration range, whereas in EM samples nanomolar concentrations are typically used. While atomic resolution structures are routinely obtained with x-ray crystallography, EM is only now approaching near atomic resolution in certain cases.[92] More realistic EM reconstruction resolutions from single particles are between 8 and 25 angstroms, depending on the method used. In addition to the sample size advantage EM can also aid in the ability to solve structures for proteins that are unable to form crystals, or for large macromolecular assemblies, which are too large to solve by x-ray crystallography. One disadvantage is the necessity for protein purity when using EM,[93] unlike crystallography which is not necessarily as sensitive. If there are impurities in the EM images, assuming they adsorb to the grids, which is also a separation step, they could be averaged in with the particles of interest in the reconstruction. Attempts at crystallizing full length sGC have been unsuccessful, therefore we attempted to reconstruct the three dimensional shape of the protein using EM.

3.a.4. Transmission electron microscopy – protein preparation considerations

Transmission electron microscopy has been used to image proteins and construct three dimensional models. Negative stain EM utilizes a heavy metal stain that provides contrast to the background while minimally adsorbing to the protein itself. This is the opposite of positive stain in which the molecule itself is stained, and the background is left unmodified. Negative stain EM provides the most dramatic image contrast, which easily allows the molecule to be visually inspected. Its main use however is to prevent structural collapse after the protein is dried.[93]

Proteins are susceptible to radiation damage and their exposure to electrons when preforming EM must be limited or mitigated in some manner.[93] A very common method of protecting the protein during EM is to apply a stain that absorbs or scatters the electrons, protecting the fragile molecule.[93] Proteins scatter electrons poorly because they are nearly entirely made up of light atoms. They are also prone to dehydration in the vacuum applied in the microscope.[93] Heavy metal stains also aid in maintaining the protein structure upon dehydration.[93] For these reasons it is often the starting point of any three dimensional reconstruction.

The protein of interest must be adsorbed to a thin carbon coated grid during the negative stain EM method. Adsorption of the protein may only be possible after surface modification of the carbon coated grid. Treatment of the surface with magnesium acetate yields a positively charged hydrophilic grid.[94] Treatment of the carbon coated grids with glow discharge yields a negatively charged hydrophilic surface.[94] Grids are then embedded with stain, typically uranyl acetate, uranyl formate or phosphotungtanic acid.

Uranyl formate is the preferred stain due to its fine grain size, allowing for higher resolution.[93] Images are then collected and averaged to greatly increase the signal to noise of the particle images. These images may then be used to reconstruct the three dimensional shape of the protein if certain conditions are met.

Another EM technique which has been used for the imaging of proteins is Cryo-EM. Cryo-EM is a technique where the sample is frozen in liquid ethane, which produces vitreous ice, and the protein sample is imaged without stain. This provides the best resolution possible of macromolecular structure determination using EM because there are no stain clusters to muddle the protein image. There are also hybrid methods that use staining during the cryo-EM procedure to increase the contrast. However, negative stain EM is commonly employed because smaller molecules can be imaged due to the higher contrast it provides. That is aside from the requirement of an expensive cryo-EM microscope and sample preparation equipment.

The cryo-EM method freezes the sample in a small drop of solution on a carbon coated grid using a plunge freezer in liquid ethane. Since the solution freezes nearly instantaneously it does not have a chance to for crystalline ice and is glassy in structure instead, termed vitreous ice.[93] Stain can be used during this procedure to increase contrast at the expense of resolution. The particles are isotropically oriented because they are not adsorbed to the grid necessarily, but frozen in solution. Many tens to hundreds of thousands of particles are imaged and analyzed for the reconstructions due to the low contrast. Current refinements are on the order of 5-10 angstrom for the finest work. This is in comparison to negative stain EM where the highest resolution is on the order of 20-

25 angstroms. The lower size limitation for cryo-EM is several hundred kDa,[91] which may allow imaging of sGC since it is ~150 kDa, but the material is unavailable. The constructs of sGC we were using were on the order of 90 kDa, which is on the order of the lower limit of negative stain EM. The size limitation of methods was the main motivation for using negative stain EM over cryo-EM.

The work of Agard and colleagues provided an excellent example of EM reconstruction of a similar size protein.[95, 96] Specifically, the Agard group reconstructed Hsp90, which is about the same size as NT-13. A reconstruction of this size gave us confidence for undertaking such an ambitious project. However, Agard had to his advantage of having a crystal structure to work with for Hsp90 and symmetry in the molecule, which greatly enhances the ability to reconstruct the protein from the TEM images.

3.a.5. EM image reconstruction

The three dimensional reconstruction of a protein by the so-called single particle method can be performed multiple ways. This approach assumes the particle is on the grid in different orientations. In general, images of particles are organized into classes, which are different projections of the molecule. The classes are then averaged. The transformed class averages are then used to build an initial model in Fourier space using a common-lines routine (as in the EMAN routine).[97] The common-lines method uses the two dimensional projections of the class averages in Fourier space and places them through the origin of a three dimensional Fourier volume, forming a common line

between the projections of the molecule. When enough projections are averaged into the molecule it can be inversely transformed and the molecule is reconstructed. This inverse transform in then compared against the class averages to ensure the reconstruction is an accurate representation of the particles. The procedure is implemented in a iterative manner until it is self-consistent between the projections of the reconstructed molecule and the actual class average projections.

3.b. Materials and methods

3.b.1. Grid preparation

Freshly deposited carbon (~5 nm thickness) was deposited on freshly cleaved mica substrates (Ted Pella) using an Edwards Turbo Molecular Pumped Vacuum Evaporator E306A. The carbon was adhered to 400 mesh Cu grids (Pelco) by cutting a small piece of the carbon coated mica and immersing it carbon side up at an angle of ~60^{o} from horizontal in a small boat of water. A grid shiny side up was used to scoop a small piece of floating carbon onto the grid, being careful that the carbon did not wrap around the other side of the grid. The carbon coated grid was glow discharged carbon side up for 20 s using a Hummer 6 Sputtering Device (evacuated and purged twice with argon), and used the same day.

3.b.2. Protein adsorption and staining procedure

Heterodimeric *Manduca sexta* (Ms) sGC-NT constructs were expressed in *E. coli* using the pET-Duet-1 plasmid. The constructs were designed by Bradley Fritz (NT-13,

NT-14 (with Mark Lee)) and Andrzej Weichsel (NT-19, and full-length Ms sGC), please see recent publications for protein preparation details.[13, 80] Protein was diluted to 10 nM with the indicated buffer. 0.75% uranyl formate was prepared by dissolving 18.75 mg of uranyl formate in 2.5 mL boiling water, stirred for 5 min and covered with aluminum foil to keep dark. 50 μL of 2.5 M NaOH was then added and the yellow color of the solution darkened. The solution was then stirred in the dark for an additional 5 min in the dark before being filtered through a 0.2 μm syringe filter into a black tube and used within 24 h. The grids were placed (always carbon side down) on a drop of protein solution for 2 min and then blotted on the edge with filter paper. The grids were then briefly suspended on a drop of water twice and blotted on the edge each time. The grids were then suspended on a drop of 0.75% Uranyl Formate stain for 20-60 seconds, blotted on the edge with filter paper and suspended a second time for 20 seconds followed by a final blotting with filter paper.

3.b.3. EM imaging

Transmission electron micrographs were obtained on a Philips CM-12 at 80 kV or 100 kV. All the images shown were obtained on an AMT 1k x 1k camera. Images were typically acquired at a defocus of 1-5 μm.

3.c. Results and discussion

3.c.1. Development of protein adsorption conditions

In order to take EM images of proteins for three dimensional reconstruction a method must first be developed to adsorb the protein to the TEM grid. First, we examined whether NT-13 could be adsorbed to uncoated carbon coated grids. The protein was diluted to 10 nM in phosphate buffer and stained with the standard method. Despite attempting numerous conditions, this approach was never successful and self-consistent particle sets were never observed. Untreated carbon coated grids are hydrophobic and therefore some proteins do not readily adsorb since solvent exposed residues tend to be hydrophilic. To overcome this difficulty, the carbon coated grids were treated with magnesium acetate in order to impart a positively charged hydrophilic surface, or alternatively were glow-discharged to yield a negatively charged hydrophilic surface. Glow discharge treatment of carbon coated grids, a treatment where the grids are exposed to plasma, is very common when adsorbing proteins. Grids that were glow discharged and then treated with magnesium acetate treated yield protein adsorption. Glow discharged grids also produced conditions where proteins were adsorbed and apparent in the images (particles of expected size), this was the method of choice moving forward. Details of these experiments are presented in subsequent sections. In order to determine if the particles observed were merely artifacts a method for a positive control was developed.

3.c.2. Negative stain electron microscopy of GroEL as a control

A positive control was developed to ensure that the procedure and microscopy conditions used were capable of imaging proteins, and particles observed for the sGC

fragments imaged were not just artifacts. Negative controls were performed throughout these experiments and no features were observed like the particles documented herein. However, a positive control provided direct evidence of protein adsorption and validation of staining and imaging conditions. As a control heat shock protein (hsp60) was imaged, albeit by accident. A protein preparation intending to grow full length sGC by Andrzej Weichsel was diluted to 10 nM in 250 mM ammonium acetate, pH 7.5. Carbon coated grids were glow discharge treated and incubated on a drop of the protein solution for 2 min, then blotted dry on the edge of the grid. The grids were then rinsed twice with water and blotted dry with filter paper each time. The grids were then incubated on freshly prepared 0.75% uranyl formate for 60 seconds twice, blotted dry on the edge each time. Negative controls were obtained by using all the same steps except instead of incubating on a drop of protein they were incubated on a drop of buffer.

A typical negative control micrograph is shown in Figure 3.1. The carbon is apparent in the image but the only features seen are defects in the carbon. The positive control GroEL was immediately recognized on the grids under the electron microscope (Figure 3.2). Upon close examination it appeared there may be a mixture of GroEL and GroEL/GroES complex (see Figure 3.3). GroEL has a square shape on its side and a circular shape on the ends with 7 subunits making up the circle.[98] Figure 3.4 shows a cryo-EM micrograph and class averages of GroEL.[98] The GroEL/GroES complex is shaped like a cone on one end in the side view of GroEL, this is observed in some but not all of the particles. Whether our images are of GroEL or the complex GroEL/GroES is largely unimportant. Regardless, this was a good confirmation that we were in fact able

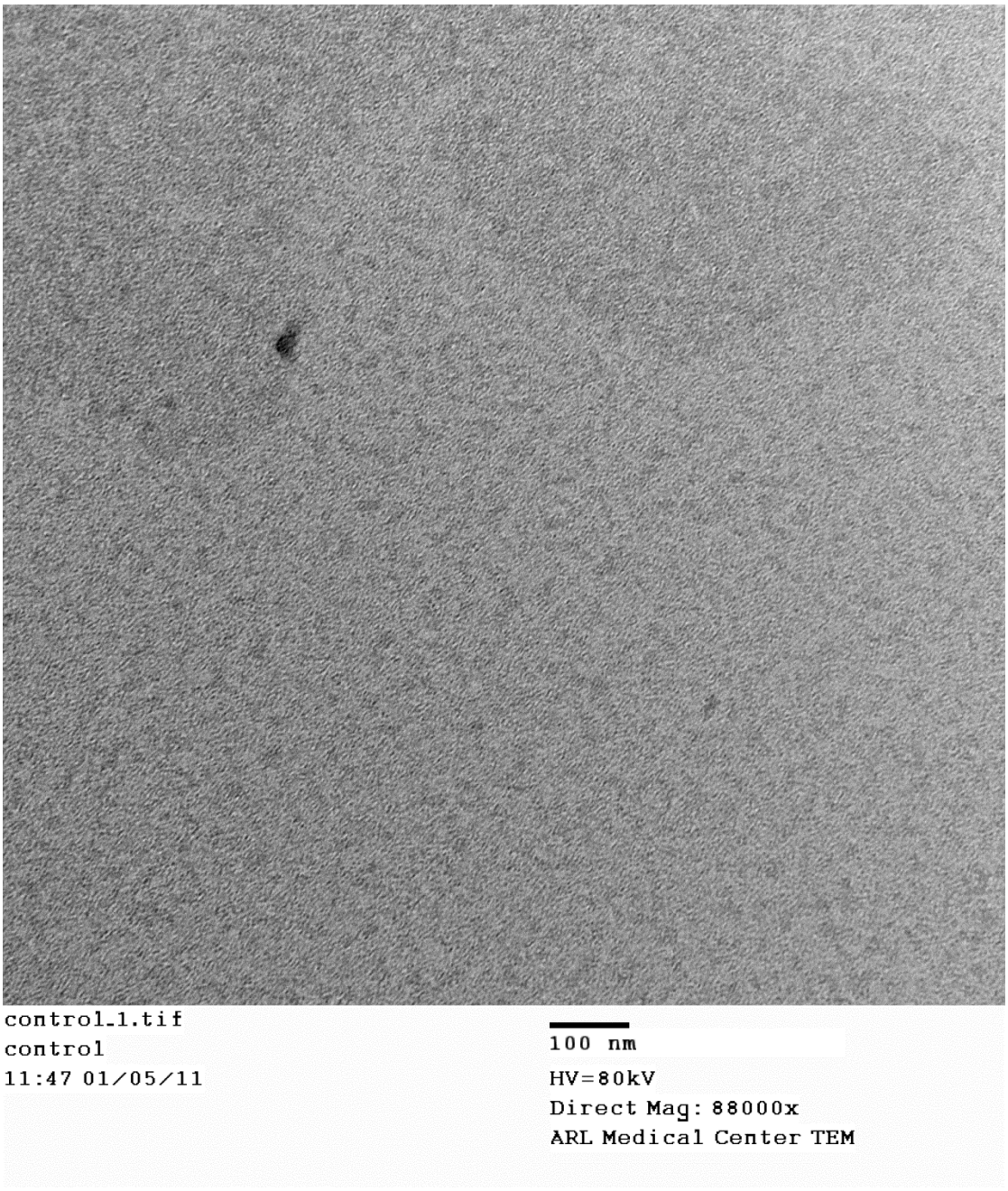

Figure 3.1. A typical negative control (glow discharged and stained with uranyl formate) micrograph.

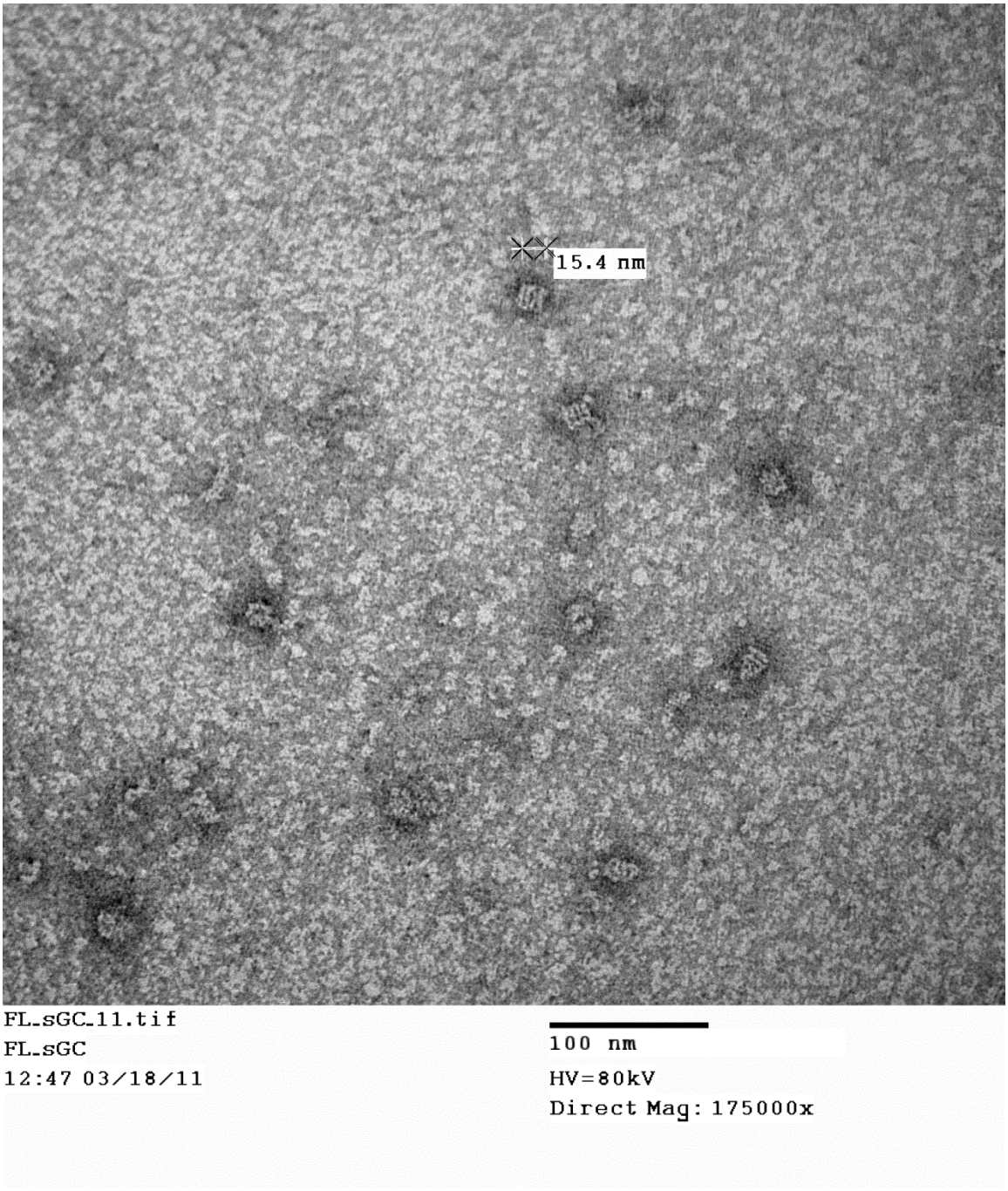

Figure 3.2. TEM of GroEL particles and possibly GroEL/GroES complex particles. See text for details.

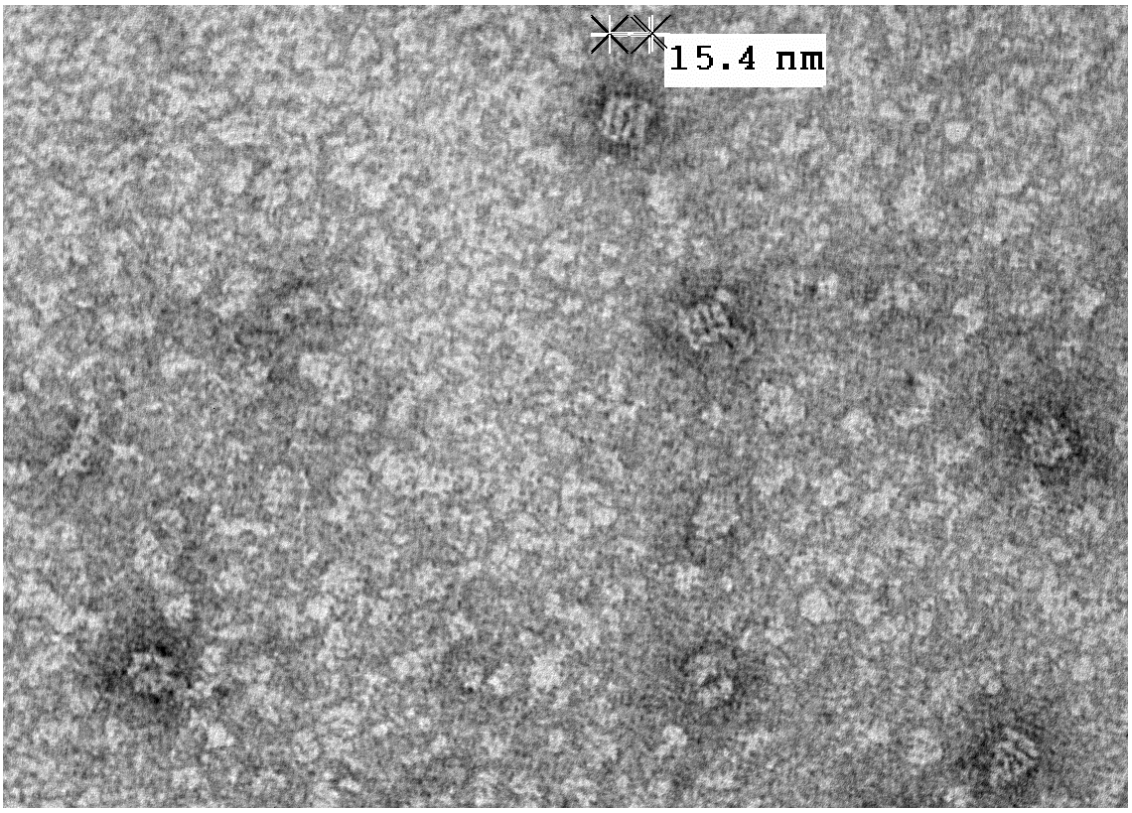

Figure 3.3. Magnified image of TEM in Figure 1 showing GroEL particles and possibly GroEL/GroES complex particles. See text for details.

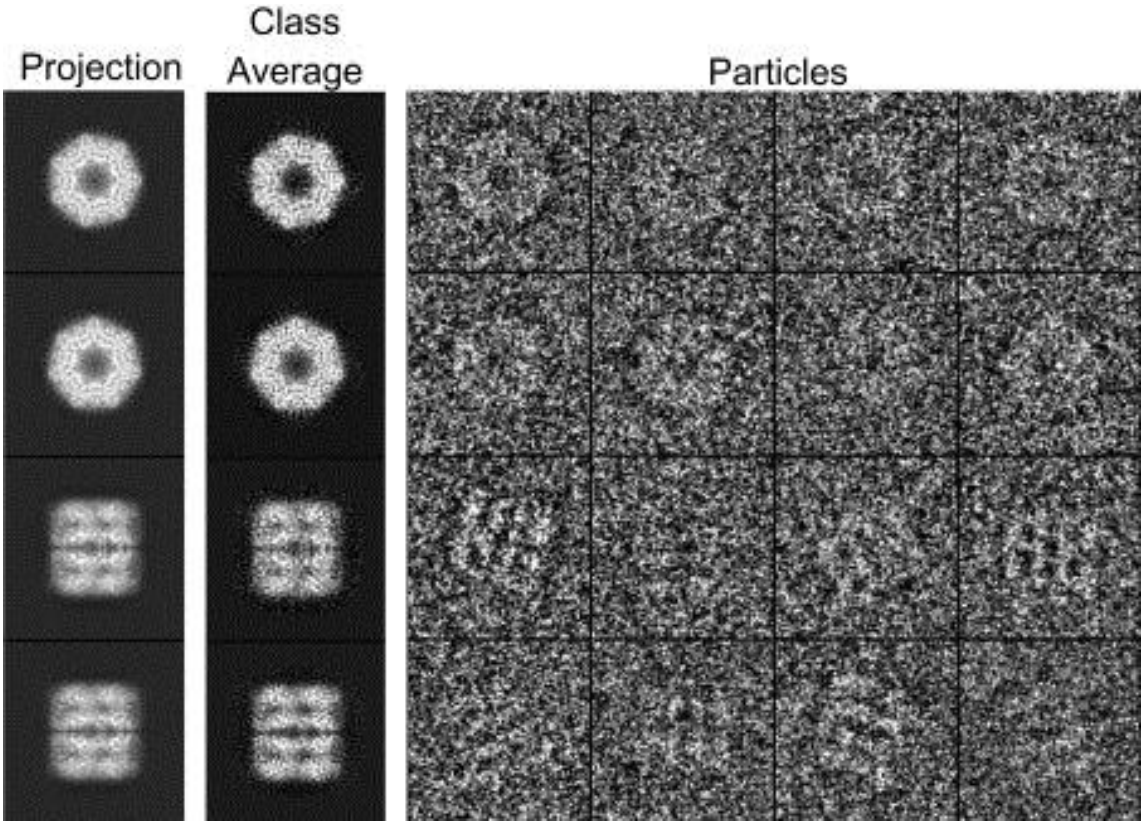

Figure 3.4. Cryo-EM images and averaged images of GroEL. Reprinted with permission from reference 98. Copyright 2004 Elsevier.

to image proteins using EM on the grids with our standard protocol developed for imaging sGC fragments. The goal moving forward was to get a homogenous particle set.

3.c.3. Initial imaging results of sGC fragment NT-13

The initial images of sGC were obtained using 5 mM sodium phosphate buffer pH 7.5. This was used until it came to our attention in the literature that it can be incompatible with uranyl formate producing precipitates. Although no precipitates were ever observed it didn't prove to provide good imaging conditions.

In the initial method used to obtain images, the grids were glow discharged for 20 seconds and incubated in 5 mM magnesium acetate for 2 min to impart a hydrophilic positive charge. The grids were then incubated on a drop of 10 nM Ms sGC NT-13 (which contains residues α 49-450, β 1-380) in 5 mM sodium phosphate buffer, pH 7.5, and then blotted dry on the edge with filter paper. The grids were then rinsed on a drop of water twice and blotted dry on the edge with filter paper after each rinse. The grids were then incubated in 0.75% uranyl formate for 45 and blotted dry with filter paper.

Figure 3.5 is a micrograph of NT-13 using 5 mM sodium phosphate buffer. It can be seen that there are particle like outlines in the approximate size range we were expecting, which was about ~14 nm x ~8 nm x ~9 nm, based on small angle x-ray scattering data from our group (Fritz *et. al.* Molecular Model of Soluble Guanylyl Cyclase Determined by Small-Angle X-ray Scattering and Chemical Cross-Linking, in review). However, these micrographs leave much to be desired; they are negative stain images with a dark background and light particles, and not of sufficient quality for image

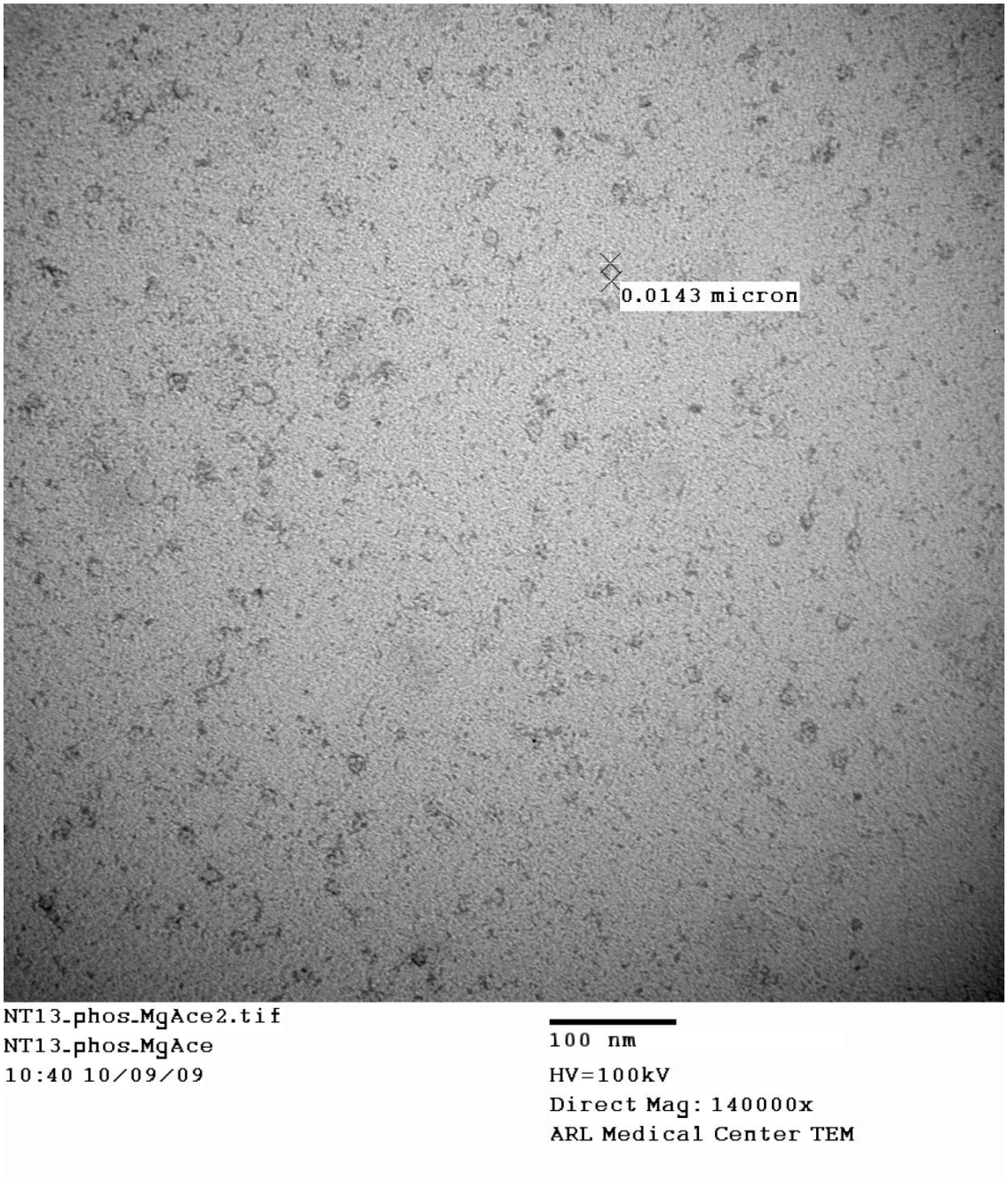

Figure 3.5. NT-13 imaged in 5 mM sodium phosphate buffer, on a glow discharged carbon coated grid treated with 5mM magnesium acetate, stained with uranyl formate.

reconstruction.

3.c.4. Alternative fragments of soluble guanylate cyclase for imaging

In an attempt to provide a more favorable interaction for adsorption between the protein and the carbon coated grid, we turned to another protein construct termed Ms sGC NT-14 was used. NT-14 contained residues α 49-471-GST, β 1-401, which is the NT-13 fragment of sGC with the addition of a glutathione S-transferase (GST) tag.

Carbon coated grids were glow discharged for 20 seconds. They were then incubated in 10 nM NT-14 in 5 mM sodium phosphate buffer pH 7.5 for 2 min. No magnesium acetate treatment was used. The grids were then blotted on the edge with filter paper and rinsed in a drop of water twice, and blotted after each rinse. The grids were then stained for 45 seconds in 0.75% uranyl formate, and blotted dry a final time. It was thought that the GST tag may have a significant enough interaction with the carbon coated grid to facilitate adsorption. This protein is about 22 kDa larger, and was designed to yield better purity, better yield and improved crystallization. None of these goals were realized, but it did in fact aid in adhering the protein to the carbon coated grids. NT-14 was able to be best imaged on glow-discharged carbon coated grids, a negative hydrophilic surface. These images were much more in line with traditional negatively stained micrographs with dark contrast around the particles and particles being light in contrast (Figure 3.6). However, the particles are heterogeneous in shape and size. Our focus shifted to a better buffer system to image with and back to fragments of sGC without large purification/solubilization tags such as GST.

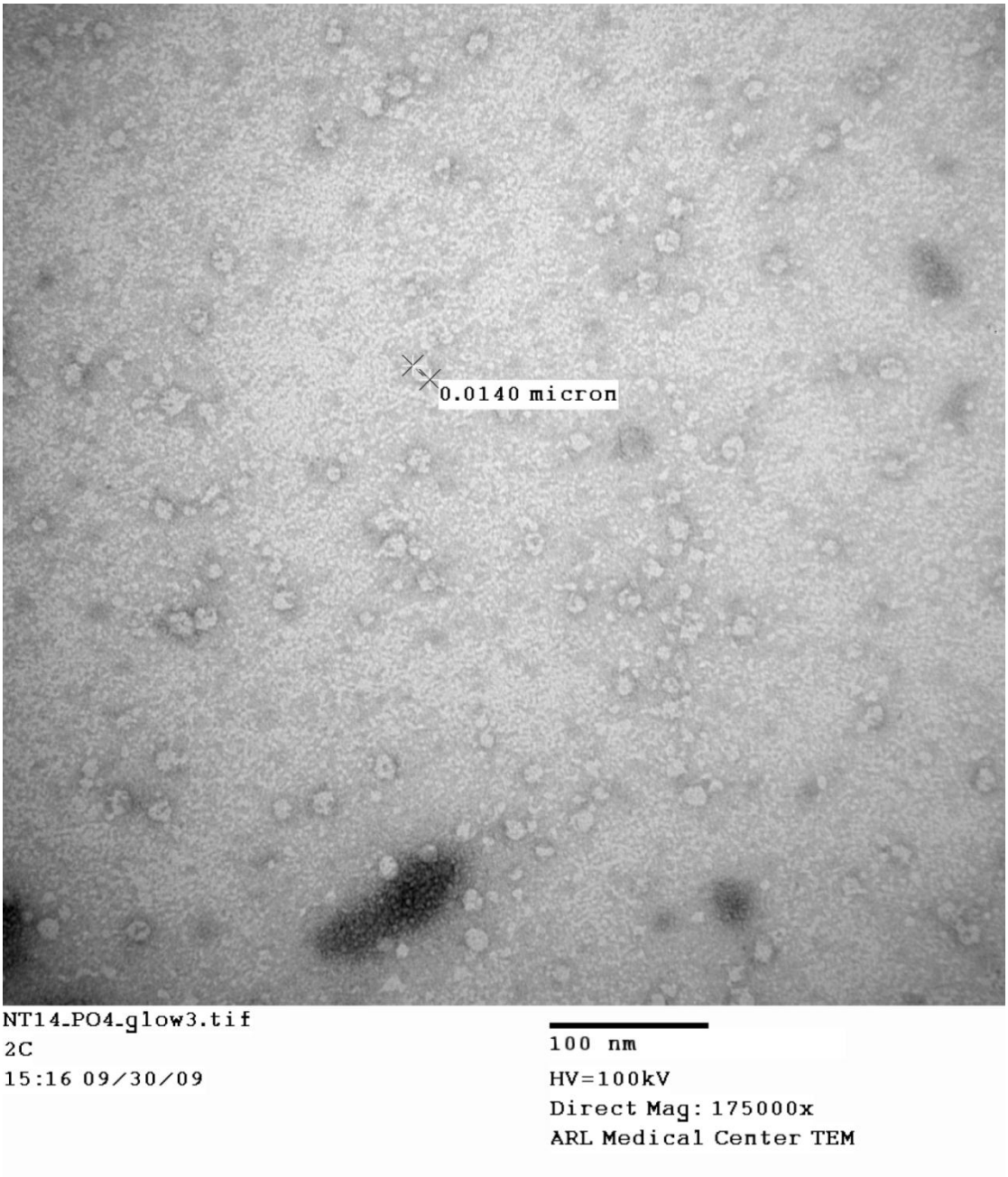

Figure 3.6. NT-14 imaged in 5 mM sodium phosphate buffer, on a glow discharged carbon coated grid, stained with uranyl formate.

3.c.5. Improvement of the imaging buffer system and staining protocol

Ammonium acetate was used in an effort to find conditions that yielded good images without a large tag on the sGC fragment. Ammonium acetate is a preferred buffer in EM due to its ability to sublime under vacuum. Carbon coated grids were glow discharged for 30 seconds. They were then suspended on a drop of 10 nM NT-13 in 250 mM ammonium acetate buffer, pH 7.25, for 2 min. The grids were then blotted dry on the edge with filter paper and rinsed twice on a drop of water, and blotted after each rinse. The grids were then stained by suspending on a drop of 0.75% uranyl formate for 2 min twice, wicking dry each time. It was observed that staining twice produced more a more uniform stain background.

These images were drastically improved in terms of overall appearance, quality of staining and particle shape/size distribution (see Figure 3.7). These conditions produced convincing protein particles, although they were still heterogeneous in shape and appeared to suffer from aggregation. Naturally different views of the same object projected in two dimensions could produce starkly different shapes, what was observed was beyond dimensions physically possible for the same object. Particles on the order of 5 nm to 20 nm were observed.

The circular shaped particles on the order of 20 nm would preclude that they would have a least two sides that are 20 nm if imaged for another angle. Imaging particles that were on the order of 5 nm x 5 nm yield the 20 nm particles impossible. That is, assuming the object does in fact have a definite shape and is monodisperse.

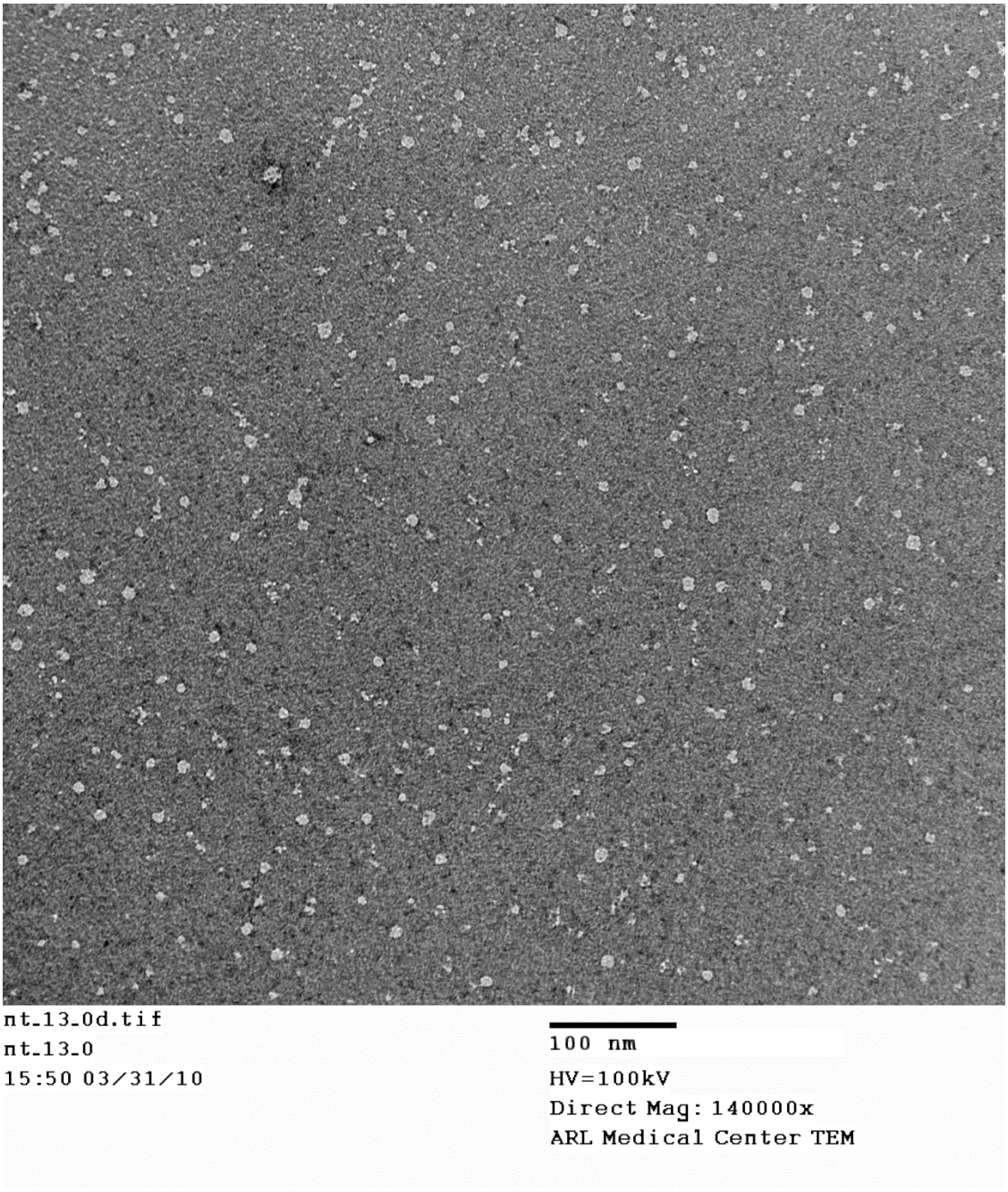

Figure 3.7. TEM of NT-13 in 250 nM ammonium acetate buffer, stained with uranyl formate, see text for details.

From this point forward we searched for ways to eliminate this heterogeneity, assuming it was imparted to the protein upon adsorption/drying/staining on the grid, and not inherent to the molecule itself. The heterogeneity could also be the result of protein impurities as well. There are groups that are attempting to perform three-dimensional reconstructions from single particles that heterogeneous but this is well beyond our expertise.

3.c.6. NT-19, a highly pure sGC fragment

In order to rid the images of heterogeneity though due to impurities, a highly purified construct of sGC was used. A final construct was imaged, NT-19, which contained the residues α 49-450-strep, β 1-380. This was the most pure protein sample of the truncated *Manduca sexta* sGC proteins produced in our lab, by Andrzej Weichsel. A strep tag allowed use of a strep tag column, which allowed for the increased purity greatly. It was also found to be monodisperse by dynamic light scattering.

Glow discharged treated carbon coated were suspended on a drop of 10 nM NT-19 in 250 mM ammonium acetate pH 7.25 for 2 min. The grids were then suspended on a drop of water briefly to rinse, twice, and dried by wicking with filter paper after each water treatment. The grids were then stained with 0.75% uranyl formate for 60 seconds twice, wicked dry on the edge each time with filter paper. This amount of time for staining works as well as 120 seconds.

Unfortunately, these images also did not yield homogenous particles. The purity of NT-19 and it's monodispersity, led me to believe that it was not necessarily the impurities imparting the heterogeneity in the particle images. It is known to aggregate,

and this is my hypothesis as to the heterogeneity. However, it cannot ever be proven that the conditions for imaging have imparted the structures observed in the images, and in reality this can never actually be proven based on these data alone.

Figure 3.8 is a typical micrograph of NT-19 using glow-discharged grids, uranyl formate as a stain. The particles are more homogenous under these conditions than any other examined in this work. However, there still exists indisputable heterogeneity in the particle size and shapes.

3.c.7. Alternative buffers, stains and additives

It was thought that the lack of salt in the deposition buffer may have led to the heterogeneous structures observed. Therefore we tried including salts in the buffers but this did not solve the homogeneity problem. We tried switching buffers to HEPES, and varied the concentration of the buffer as well as adding salt to the buffer. All these conditions proved not to mitigate the heterogeneity of the particles. The addition of sugars, which has been shown to aid in maintaining the native structure of proteins upon drying, we added to the buffer and no improvement was noted.

The buffer conditions examined were 5mM HEPES pH 7.5, 50 mM HEPES 10 nM NaCl pH 7.5, 250 mM HEPES pH 7.5 50 mM NaCl, 250 mM Amonium acetate pH 7.25 10 mM $MgCl_2$, Amonium acetate pH 7.25 10 mM $CaCl_2$, Amonium acetate pH 7.25 510 mM NaCl, Amonium acetate pH 7.25 1010 mM NaCl, 30 mM HEPES 6mM 13.7 mM maltose, Amonium acetate pH 7.256% glycerol, 30mM HEPES pH 7.5 10%glycerol 6mMNaCl, 30mM HEPES pH 7.5 10%sucrose 6mMNaCl. None of these efforts

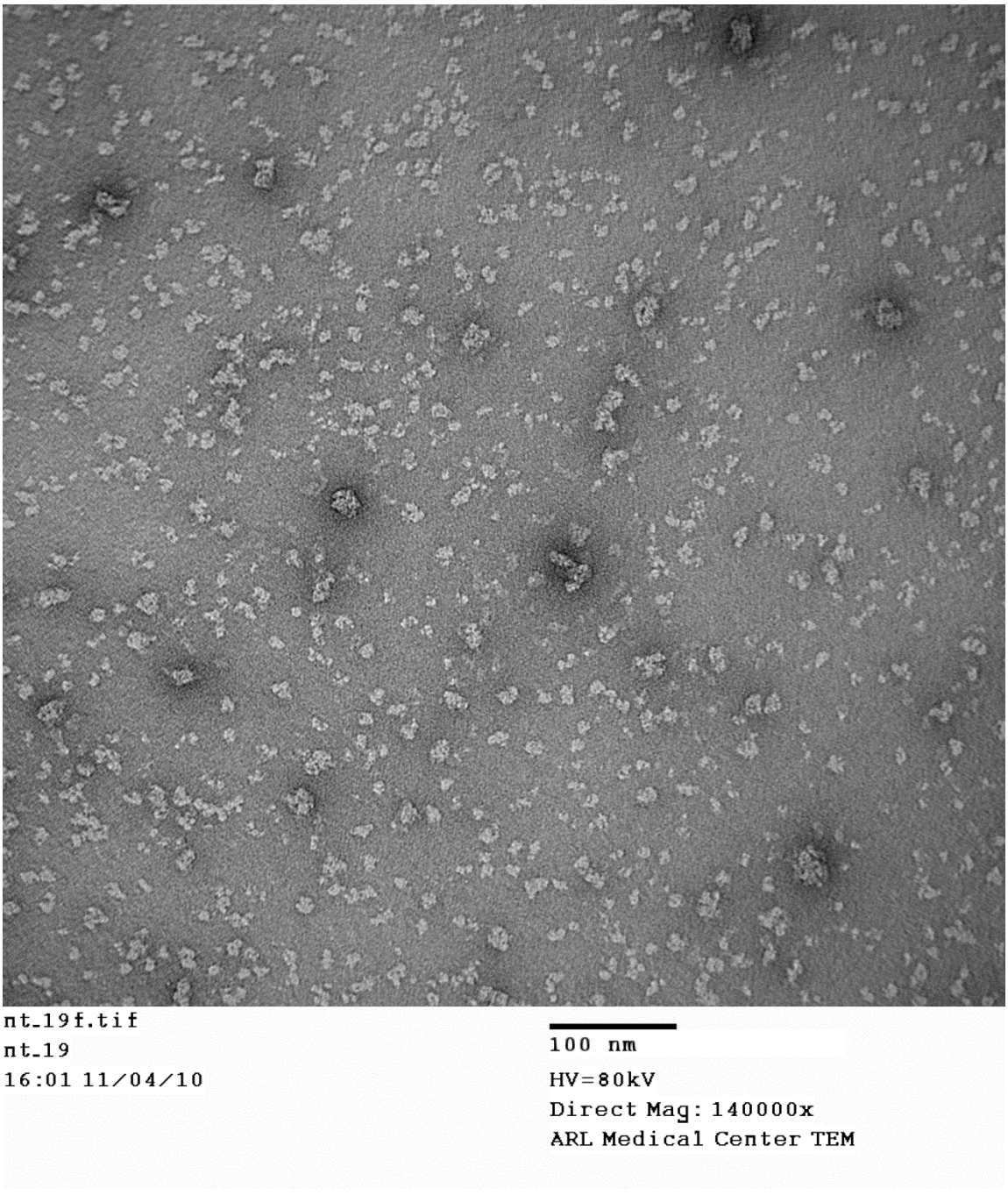

Figure 3.8. NT-19 imaged on carbon coated glow-discharged grids stained with uranyl formate, see text for details.

produced convincingly homogenous particles of NT-19.

3.d. Conclusions and Future Directions

The heterogeneity of the particles was the major issue with these experiments. All reconstructions performed with the data in this chapter (using EMAN2)[99] were believed to be unreliable and not presented, due to the inclusion of non-homogenous particles. The most likely cause of the heterogeneity is aggregation on the surface, which may be due to the drying or staining procedure. Thus, sample preparation must be optimized further. Trehalose is a sugar known to preserve native protein structure upon drying and should be investigated for use in subsequent experiments.[100] Also if cryo-EM was used on the full length protein, and/or negative stain cryo-EM, it could possibly solve these issues and may provide the best possible chance of successful imaging.

CHAPTER 4

PARTICLE SIZE DEPENDENCE OF SENSITIVITY ENHANCEMENT USING SILICA COLLOIDAL CRYSTALS AS MICROARRAY PLATFORMS

4.a. Introduction

4.a.1. Biomarker discovery

Biomarker discovery has slowed in recent years with respect to identification and validation. Protein concentration in blood plasma spans 11 orders of magnitude[101] and as a result researchers need to identify new techniques in order to expand the range of protein concentrations available for quantitation.[102, 103] Currently, mass spectrometry can reach well into the low range of protein concentration[104, 105] but there exists many complications with this method including low throughput, expensive instrumentation, cumbersome sample preparation and poor quantitation.

The application of protein microarrays to biomarker analysis has become an increasingly important method of protein analysis.[106-109] These assays typically involve a surface bound antibody that captures a fluorescently labeled protein. Microarrays have several advantages over traditional methods such as 2D PAGE and HPLC such as high throughput and low reagent consumption.[110] However, microarrays can be limited by poor reproducibility and lack of sensitivity.[102, 103, 110, 111]

4.a.2. Protein microarrays

Currently there are several methodologies for increasing the sensitivity of protein microarrays. Rolling-circle amplified protein microarrays achieve greater sensitivity by coupling a secondary antibody to circular DNA that is then amplified to which complementary DNA with fluorescent probes hybridize.[102, 103] This approach seems promising but a simpler, more convenient approach would be more adaptable. Waveguides have also been used,[111] but the instrumentation required can be inconvenient or cost prohibitive. A silicon wafer with controlled silicon oxide layer that produces constructive interference of fluorescence emission and excitation light, producing a signal enhancement of five to ten-fold has been described,[110] but the authors use a polymer coating that is unconventional and the general applicability of the surface treatment to other systems has not been documented.

Protein microarray substrates have evolved to include slide surfaces modified with nitrocellulose, hydrogels, polylysine, and functionalized silane coated glass slides.[112-115] The binding affinity of proteins to the different substrate coatings can vary, as well as the activity of the protein.

4.a.3. Silica colloidal crystals

This research included herein is based on increasing the sensitivity (i.e. lowering the detection limit) of protein microarrays utilizing silica colloidal crystals. These have been used in the photonics industry for years for their excellent optical properties. The surface chemistry of silica has been well documented in the literature, which makes it an ideal material for a microarray substrate. Recently, it has been shown that silica colloidal

crystals can be used to enhance the fluorescence signal of a streptavidin-biotin assay.[116] These assays exploit the additional surface area that the colloidal crystal provides as compared to flat glass slides. The material enhances the dynamic range of the assay, lowers the detection limit and shortens the time needed for binding.

An improvement to the fabrication of silica colloidal crystals was developed via an innovative spin coating technique, which does not require chemical modification of the slides prior to spin coating[117] or polymers that prohibit the spheres from close packing, as do other spin coating methods.[118] This spin coating innovation drastically enhances the speed at which colloidal crystals can be deposited, from seconds to min as opposed to the traditional vertical deposition method, which typically takes days. In addition, the traditional vertical deposition method produces an undesirable thickness gradient due to the solvent evaporation. This gradient is eliminated with the innovative spin coating technique.

The research herein utilized silica colloidal crystals modified with glycidoxypropyltrimethoxy silane (GOPS) as a novel reverse protein microarray platform. The model system used bovine serum albumin (BSA) and its FITC labeled antibody to demonstrate variation in sensitivity as a function of silica colloid particle size, which was compared to GOPS coated flat slides.

4.b. Materials and methods:

Silica colloids of various sizes (Fiber Optic Center) were calcined at 600 ^{o}C for 6 h two times, sonicated in acetone and then dried between calcinations steps, to prevent

the silica colloidal crystals from cracking.[119] The particle size standard deviation was reported to be less than 10% from the manufacturer. Slides were rinsed thoroughly with water (3.5 MΩ) and boiled in 50 vol% nitric acid (EMD) for 2 h. They were then thoroughly rinsed with water (18.2 MΩ) and dried in a centrifuge (Eppendorph 5804). The silica slurries were sonicated for a minimum of 4 h and up to 18 h in an ultrasonic bath (VWR 150T) to disperse the suspensions. It is critical that the solution be completely dispersed prior to spin coating. Quartz slides (GM and Associates) were cut into 1" x 1" squares and mechanically cleaned with 2% Alconox solution by gentle rubbing. The slides were then spin coated (Brewer Scientific) with 200 μL of silica slurry according to the parameters described in Table 4.1. The slides were spun until the solvent evaporated. For volatile solvents (acetone and ethanol), as little as 30 s of spinning was needed, while for water, up to 300 s of spinning was necessary to for the solution to dry. Anecdotally, this spin coating process may be performed multiple times to increase the thickness of the colloidal crystal (data not shown). The slides were then sintered at 1050 ^{o}C (Thermo Electron Corp Box Furnace) for 8 h. The slides were rehydroxylated in piranha solution (3:1, sulfuric acid: 30% hydrogen peroxide) for 3 h and then rinsed thoroughly with water. The slides were then dipped into boiling methanol (HPLC grade, EMD) before being placed in toluene (EMD) with 2% glycidoxypropyltrimethoxy silane (Gelest) and refluxed for 18 h. The slides were then rinsed with hot toluene (EMD) and used the same day.

BSA (EMD), 5 mg/mL in 50 mM carbonate buffer pH 9.6 was spotted onto the slides using a contact pin (Whatman Microcaster). The slides were incubated at 44%

Table 4.1. Spin Coating Parameters

Particle diameter (nm)	wt % silica	solvent	acceleration	speed
290	20	ethanol	3000 rpm/s	5000 rpm
510	20	acetone	5000 rpm/s	3000 rpm
780	17.5	acetone	3000 rpm/s	3000 rpm
1250	30	water	100 rpm/s	650 rpm

humidity for 30 min. The slides were then blocked with 400 mM ethanolamine (Sigma-Aldrich) in 50 mM borate buffer (pH 8.7) for 100 min, while being gently shaken on an orbital shaker. The slides were incubated for 90 min with 0.001 mg/mL sheep antiBSA-FITC (Immunology Consultants Laboratory, Inc.) (Figure 4.1). The slides were then rinsed for 3 min 3 times in 50 mM borate buffer (pH 8.7) and dried in a centrifuge (Eppendorph 5804). The slides were the read immediately on an inverted epifluorescence microscope (Nikon Eclipse TE 2000-U), illuminated by a high-pressure mercury lamp (100 W, OSRAM). A 2X objective (Nikon Plan Apo WD 8.5) was used for all measurements. Integration times of 1 s were used for colloidal crystal microarrays and 10 s integration times were used for flat slides due to the small signal they produced (Princeton Instruments Photon Max 512) using a FITC filter cube (Nikon B-2E/C).

The fluoresce intensity of the spots were averaged for each spot. The background in the immediate vicinity of the spot was averaged for a similar size area as the spot, and subtracted from the spots fluorescence signal. Three colloidal crystal slides of each particle size and three flat slides, each with five spots, were fabricated and analyzed.

Scanning electron microscopy was performed on a Hitachi 4800 SEM. Slides were coated with platinum to reduce charging of the sample.

UV/Visible spectra were recorded on an Agilent 8453 spectrophotometer.

4.c. Results and Discussion

4.c.1. Spin coating parameters

The parameters used to fabricate the silica colloidal crystals by spin coating are

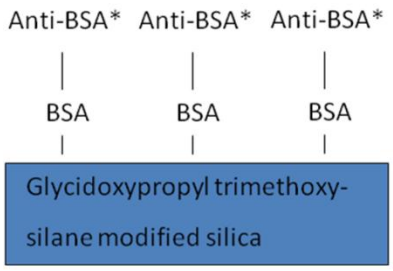

Figure 4.1. Schematic of BSA anti-BSA-FITC reverse phase protein microarray studied in this work. The GOPS modified silica surface was used on silica colloidal crystals as well as plain quartz slides.

presented in Table 4.1. These conditions were determined empirically. As can be seen in the Table, each particle size required different conditions. However, they all required high concentrations of silica in the slurry. The colloidal crystals were well ordered and uniform, as judged by scanning electron micrographs (Figure 4.2). Photographs of representative slides can be seen in Figure 4.3. The dime under the slide is for size comparison and clarity demonstration purposes. As can be seen, they are relatively clear, with some scattering for the larger particle sizes. The UV/Vis spectra of the slides can be seen in Figure 4.4. The crystals made from 290 nm colloids show a significantly greater transmission in the region where FITC is excited (495 nm). As shown first-order Bragg diffraction does not interfere with the excitation or emission light; however, the overtones are present to varying extents.

4.c.2. BSA anti-BSA microarray

A BSA anti-BSA-FITC reverse phase microarray was performed with silica colloidal crystals on a quartz substrate, and with plain quartz slides, to empirically evaluate the particle size dependence of the sensitivity enhancement gained by using colloidal crystals. To maintain a consistent surface chemistry and avoid differences in surface binding and activity between different surface chemistries we chose to use GOPS modified surfaces for both the colloidal crystals and the plain quartz slide.

As shown in Table 4.2, the microarrays made with silica colloidal crystals significantly outperformed those of flat slide substrates. The colloidal crystals made from 510 nm colloids produced the greatest fluorescence enhancement overall, with a 17-

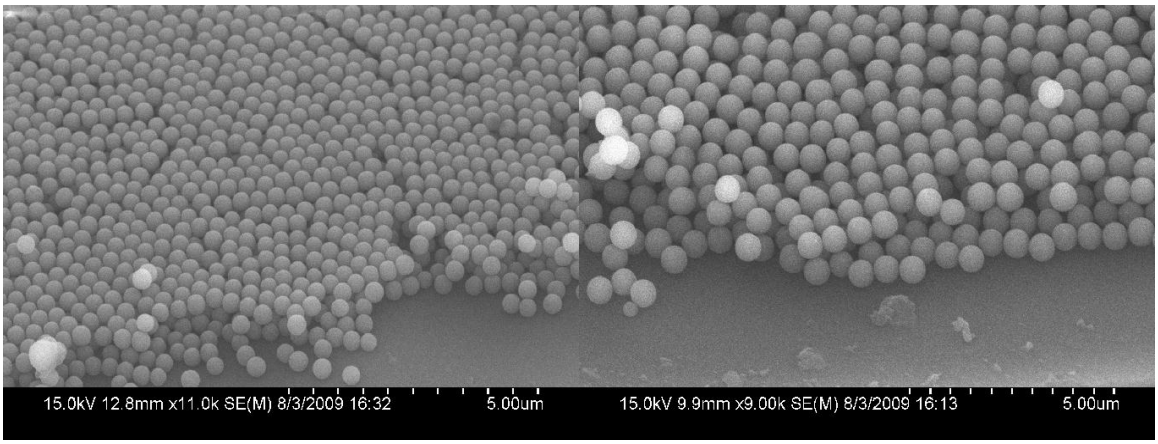

A B

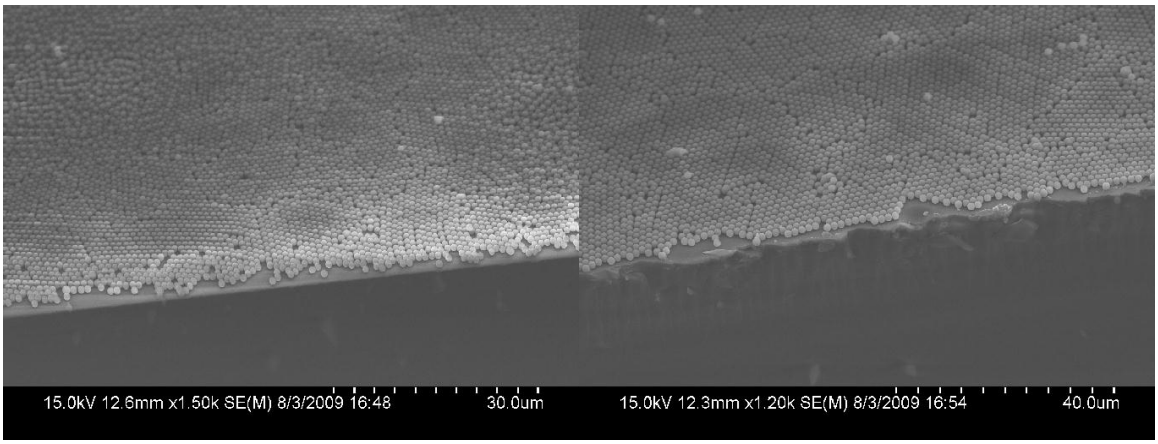

C D

Figure 4.2. SEM micrographs of colloidal crystal microarrays. Colloidal crystals made from 290, 510, 780 and 1250 nm colloids are shown in panels A-D, respectively. Slides were snapped in half and the cross sections were imaged.

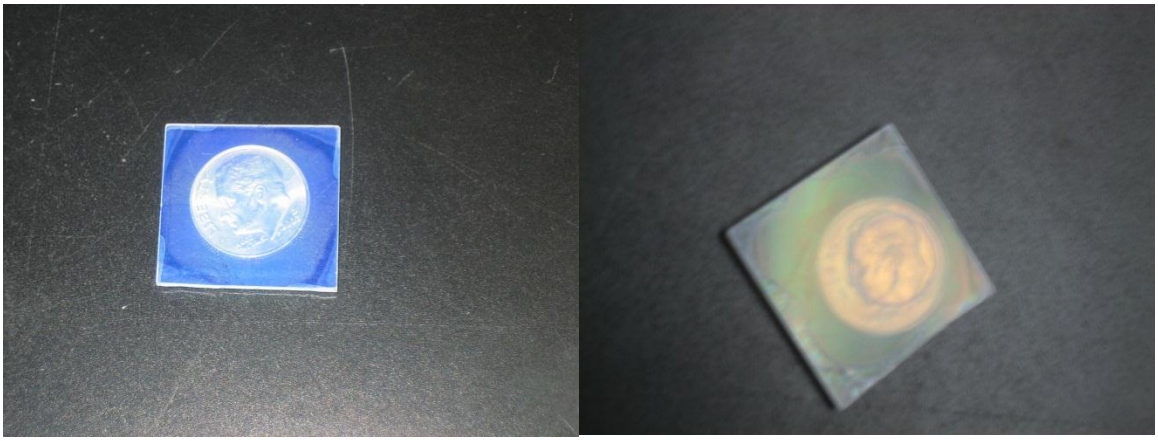

A B

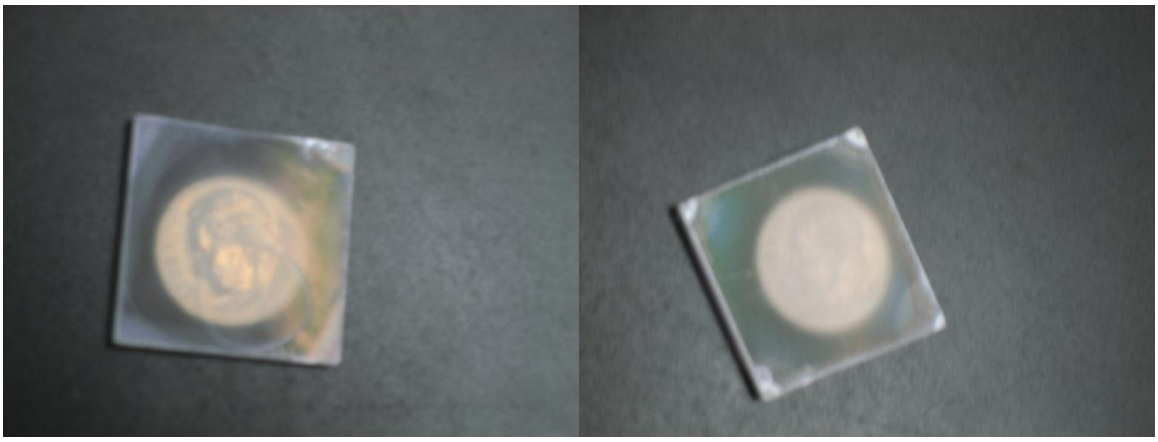

C D

Figure 4.3. Images of slides with silica colloidal crystals made from 290, 510, 780 and 1250 nm diameter silica colloids are shown in panels A-D, respectively. A dime was placed underneath the slides for size scale and to demonstrate relative transparency.

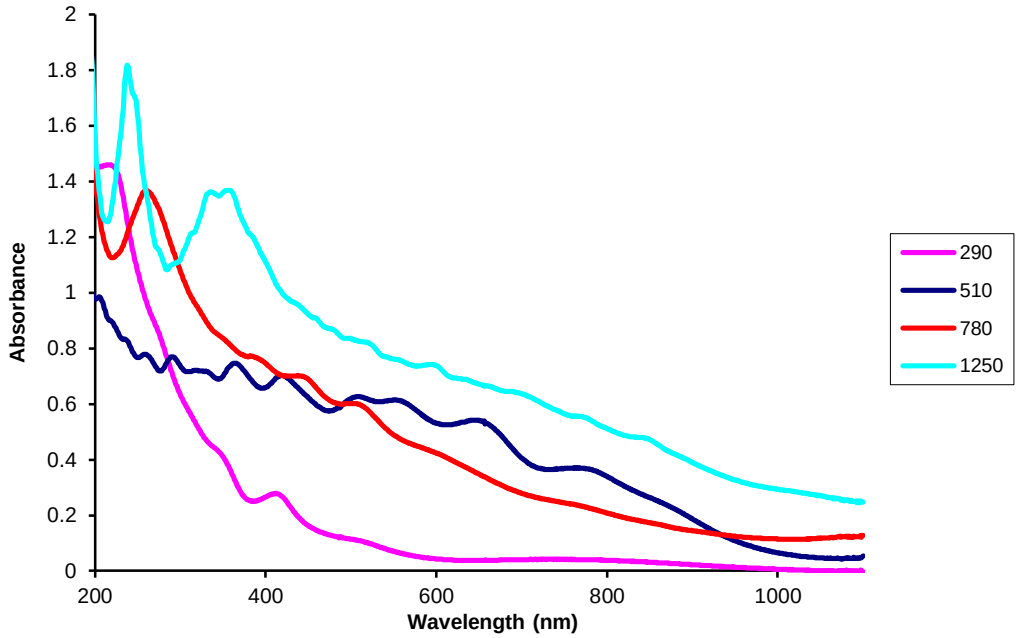

Figure 4.4. UV/Visible spectra of colloidal crystals.

Table 4.2. Results of microarrays with colloidal crystals and flat slides, both modified with glycidoxypropyltrimethoxysilane

Particle size (nm)	Background subtracted average fluorescence	Ratio increase in sensitivity over flat slides	Surface area enhancement over flat slide	number of colloid layers	Ratio increase over flat slides / thickness of crystal (μm^{-1}) [2]
flat	49 +/- 9	-	-	-	-
290	580 +/- 40	12 +/- 2	8.0	2	22
510	860 +/- 80	17 +/- 4	8.0	2	19
780	300 +/- 30	6 +/- 1	6.6	1.5[1]	7.5
1250	410 +/- 50	8 +/- 2	4.4	1	8.4

[1]The crystal had a partial second layer which was treated as a half layer, see figure 2 and 3. [2] The thickness was calculated based on the geometry of close-packed spheres.

fold increase in sensitivity compared to flat sides. Whereas the colloidal crystals made of 290 nm colloids provided the most fluorescence enhancement per unit of crystal thickness, with a 22-fold increase in sensitivity per micrometer of crystal thickness. The smaller particles provide more surface area per unit thickness but have a smaller pore size which may cause steric affects with large complexes. The reverse assay between BSA and anti-BSA-FITC is apparently not large enough to produce a significant affect. The smaller pores of the 290 nm colloids will impart greater steric hindrance on the complex. While the larger 780 nm and 1250 nm diameter colloids will provide a greater volume within the pores (which are 15% of the diameter of the particle size), the decrease in surface area is evidently not compensated for. The surface roughness of the colloids themselves is unknown but not thought to be a factor since it is likely to be much smaller than the size of the proteins.

It is interesting to note that the fluorescence increase is actually larger than the surface area enhancement. The interpretation is that the extra enhancement stems from an increase in the available volume that the curvatures that the particles provide. This increase is from 4 to 10 times that of a flat substrate assuming the complex between BSA and anti-BSA-FITC to be 20 nm in the direction normal to the surface. This size of the complex is estimated for the size of an IgG antibody which has a "Y" shape with the arm lengths of the "Y" of 8.9 nm and the base of the "Y" of 7.7 nm,[120] and BSA which is approximately a prolate ellipsoid of 14 nm X 4 nm.[121] This exemplifies an issue that was not encountered with biotin-streptavidin, which is a small molecule ligand-52.8 kDa protein system previously studied,[116] where the small size of the complex appeared to

play no role in the fluorescence enhancement, reaching the theoretical limit based on surface area. Therefore, the significantly larger BSA anti-BSA-FITC complex actually affected the enhancement significantly. It is thought that the steric limit of packing of the complex on the surface per unit area is reached much more quickly when there is no curvature on the surface. This volume around each particle in the crystal that the protein complex occupies will become even more important for larger complexes such as sandwich assays and when secondary antibodies are used. For these complexes, the optimal size particle will likely be larger than in the reverse microarray assay presented here.

There was a small amount of damage to the material by the contact pin used to deliver the BSA solution to the surface (figure 4.5A). This was not seen in all the spots and was less frequently observed in the microarrays made from 290 nm colloids. The crystals made with larger colloids appear to be less mechanically stable than those made with smaller colloids. In the fluorescence micrographs (figure 4.6) the damaged surface areas were small and are not thought to detract significantly to the total fluorescence signal of the spot, since these defects account for a small percentage of the microarray spot area. This damage may be avoidable by using non-contact printing methods such as piezo-electric printers.

The overall morphology of the spots on the colloidal crystals was relatively good. Haloes commonly found in microarray printing were observed (figure 6), though no comets or streaking were encountered. The spots were larger than those on flat slides, the crystal tended to wick the spotting solution through the pores by capillary action. It is

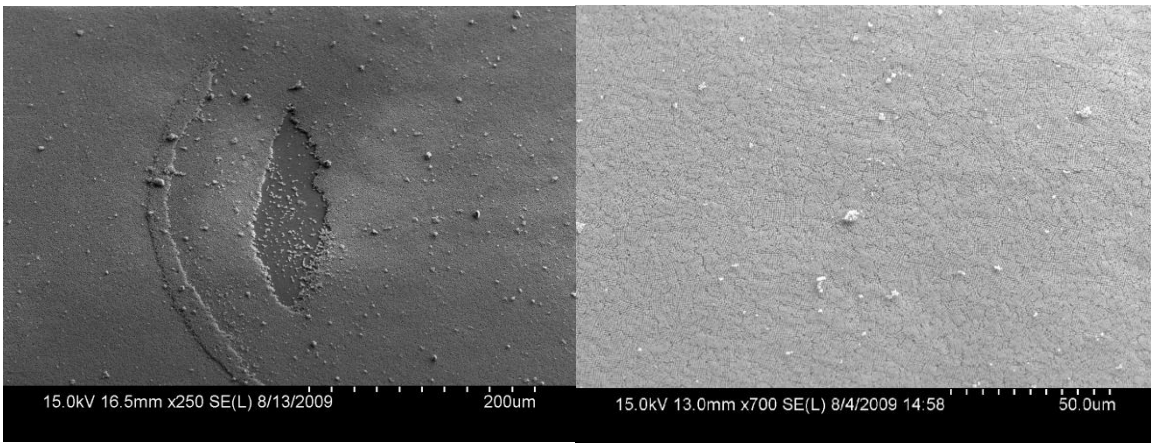

A B

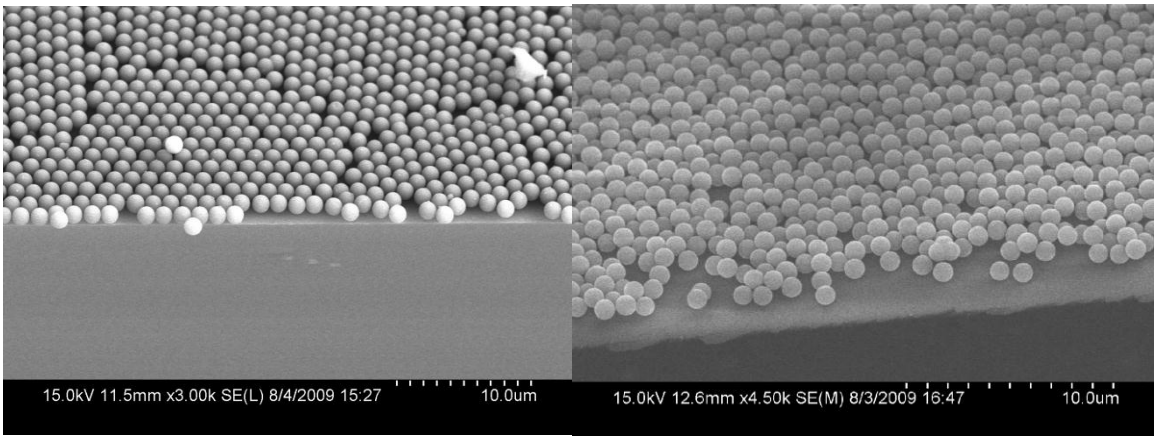

C D

Figure 4.5. A. Damage to surface by contact pin, 780 nm colloids. B. Surface showing no damage, 510 nm colloids. C. Hexagonal close-packed crystals seen in 1250 nm colloids. Partial second layer of particles seen in 780 nm colloidal crystals.

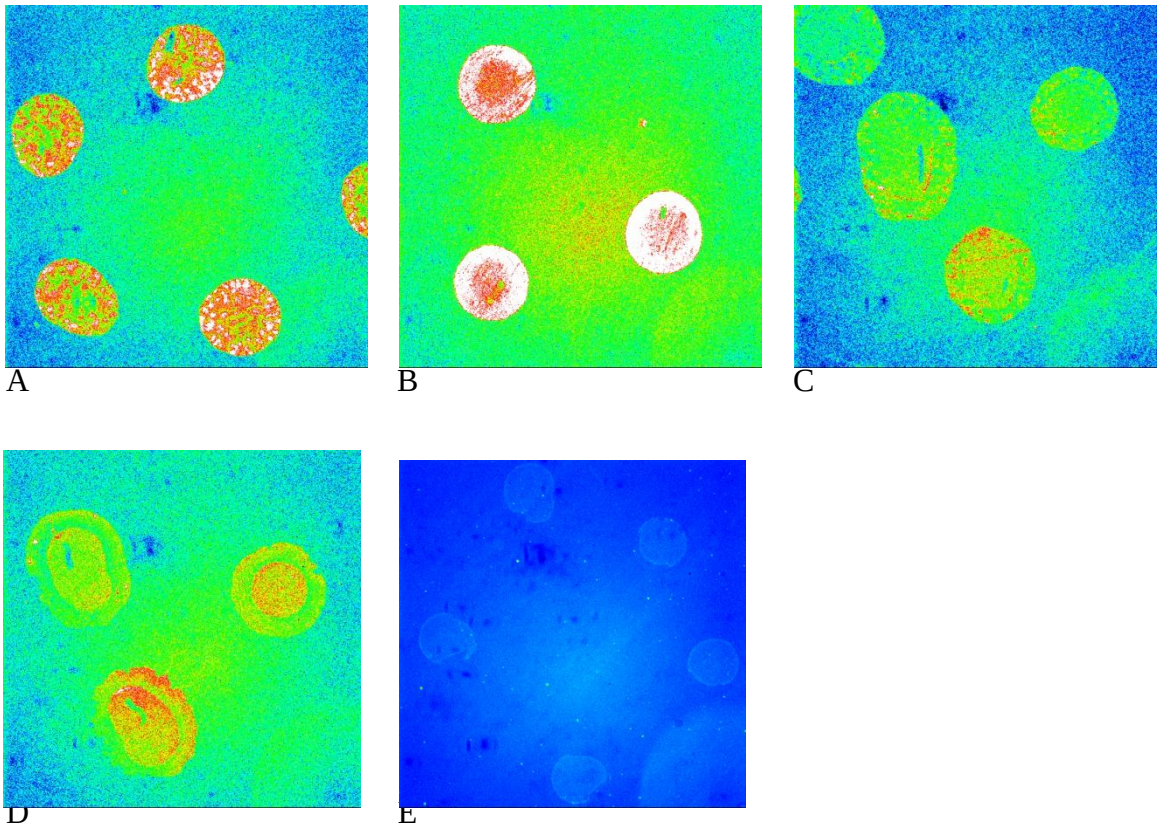

Figure 4.6. Fluorescence micrographs of the BSA anti-BSA-FITC reverse microarrays, crystals made of 290, 510, 780 and 1250 nm particles, A-D respectively; flat slide shown in E. The same intensity scale was used in A-D, E had a 10 times longer exposure so the intensity scale is 10 larger. Imaging are is 4.1 mm x 4.1 mm.

thought that by creating a more hydrophobic coating this may be largely controlled to increase the spot density on the microarray. Alternatively, smaller spotting volumes than the 4 nL deposited by the contact pins could be used to deliver less solution to the surface, yielding smaller spots.

The colloidal crystals made by the described method (Table 4.1) were very flat over areas large enough to perform microarrays (hundreds of mm^2, see figures 4. 2, 4.3 and 4.5). This was sufficient to perform the analysis presented here. This is important because it has already been shown that the thickness of the crystal is directly related to the fluorescence of the assay due to the increase surface area.[116] In the case of the crystals made of 1250 nm colloids, the method described produced extremely well oriented hexagonal close-packed crystals (see figures 4.2, 4.5). With the crystals made from 290, 510 and 780 nm colloids, there was a mixture of hexagonal close-packing and face-centered cubic structures. In the case of the 780 nm particles, the flatness was less than perfect and tended toward a second partial layer. The spin coating procedure adopted here has the advantage over previously reported methods in the use of hydrophilic slides, which eases the preparation of the slides prior to spin coating, and that no polymers need to be used during the process.[117, 118]

4.d. Conclusions and future directions:

A novel method for spin coating silica colloidal crystals was developed that yielded close-packed crystals. This approach created slides that were uniform enough in thickness and surface to be used for protein microarrays. A model reverse protein

microarray was performed modified with GOPS, using a BSA anti-BSA-FITC system. The particle size dependence of fluorescence enhancement of silica colloidal crystals using 290, 510, 780 and 1250 nm silica colloids was determined and compared to a flat slide. The crystal made of 510 nm colloids yielded the greatest fluorescence enhancement, which was 17-fold larger than that of the flat slide.

The enhancement of fluorescence is thickness dependent and therefore thicker crystals will produce even greater absolute enhancements of sensitivity. Since the protein complex becomes larger such as when secondary antibodies are used or in sandwich assays, the optimal particle size will be larger, even though the surface area decreases with larger particles. This is due to the steric hindrance within the pores of the crystal created by such large complexes. The spot size on the microarray should be able to be reduced by using a more hydrophobic coating or by decreasing the spotting volume. Damage caused by the contact pins used may be avoided by using other printing methods, such as a piezo-electric printer. These surfaces demonstrate an inexpensive, simple fabrication of microarray slides that lower the detection limit of conventional silane modified microarrays by 17-fold.

In future work the thickness of the best performer, the 510 nm colloidal crystal, could be varied to yield the most enhancement possible. Also it would be interesting to determine the kinetics of binding in the colloidal crystal. This could easily be done by monitoring the fluorescence on a microscope without agitation as a function of time. This could be done for various particle sizes to determine when pore size becomes a major factor limiting diffusion.

REFERENCES

1. Furchgott, R. F.; Zawadzki, J. V., The obligatory role of endothelial cells in the relaxation of arterial smooth muscle by acetylcholine. *Nature* **1980,** 288, (5789), 373-376.

2. Furchgott, R. F., Role of endothelium in responses of vascular smooth muscle. *Circulation Research* **1983,** 53, (5), 557-73.

3. Griffith, T. M.; Lewis, M. J.; Newby, A. C.; Henderson, A. H., Endothelium-derived relaxing factor. *Journal of the American College of Cardiology* **1988,** 12, (3), 797-806.

4. Lloyd-Jones, M. D., Donald M.; Bloch, M. D., Kenneth D., The vascular biology of nitric oxide and its role in atherogenesis. *Annual Review of Medicine* **1996,** 47, (1), 365-375.

5. Garthwaite, J.; Boulton, C. L., Nitric Oxide Signaling in the Central Nervous System. *Annual Review of Physiology* **1995,** 57, (1), 683-706.

6. Wink, D. A.; Mitchell, J. B., Chemical biology of nitric oxide: insights into regulatory, cytotoxic, and cytoprotective mechanisms of nitric oxide. *Free Radical Biology and Medicine* **1998,** 25, (4–5), 434-456.

7. Bogdan, C., Nitric oxide and the immune response. *Nat Immunol* **2001,** 2, (10), 907-916.

8. Xu, W.; Liu, L. Z.; Loizidou, M.; Ahmed, M.; Charles, I. G., The role of nitric oxide in cancer. *Cell Res* **2002,** 12, (5-6), 311-320.

9. Titheradge, M. A., Nitric oxide in septic shock. *Biochimica et Biophysica Acta (BBA) - Bioenergetics* **1999,** 1411, (2–3), 437-455.

10. Abramson, S., Nitric oxide in inflammation and pain associated with osteoarthritis. *Arthritis Research & Therapy* **2008,** 10, (Suppl 2), S2.

11. Alderton, W. K.; Cooper, C. E.; Knowles, R. G., Nitric oxide synthases: structure, function and inhibition. *Biochem. J.* **2001,** 357, (3), 593-615.

12. Zweier, J. L.; Li, H.; Samouilov, A.; Liu, X., Mechanisms of nitrite reduction to nitric oxide in the heart and vessel wall. *Nitric Oxide* **2010,** 22, (2), 83-90.

13. Hu, X.; Murata, L. B.; Weichsel, A.; Brailey, J. L.; Roberts, S. A.; Nighorn, A.; Montfort, W. R., Allostery in Recombinant Soluble Guanylyl Cyclase from Manduca sexta. *Journal of Biological Chemistry* **2008,** 283, (30), 20968-20977.

14. Malinski, T.; Taha, Z.; Grunfeld, S.; Patton, S.; Kapturczak, M.; Tomboulian, P., Diffusion of Nitric Oxide in the Aorta Wall Monitored in Situ by Porphyrinic Microsensors. *Biochemical and Biophysical Research Communications* **1993,** 193, (3), 1076-1082.

15. Beckman, J. S.; Koppenol, W. H., Nitric oxide, superoxide, and peroxynitrite: the good, the bad, and ugly. *American Journal of Physiology - Cell Physiology* **1996,** 271, (5), C1424-C1437.

16. Hetrick, E. M.; Schoenfisch, M. H., Analytical Chemistry of Nitric Oxide. *Annual Review of Analytical Chemistry* **2009,** 2, (1), 409-433.

17. Ford, P. C.; Wink, D. A.; Stanbury, D. M., Autoxidation kinetics of aqueous nitric oxide. *FEBS Letters* **1993,** 326, (1–3), 1-3.

18. Doyle, M. P.; Hoekstra, J. W., Oxidation of nitrogen oxides by bound dioxygen in hemoproteins. *Journal of Inorganic Biochemistry* **1981,** 14, (4), 351-358.

19. Hall, C. N.; Garthwaite, J., What is the real physiological NO concentration in vivo? *Nitric Oxide* **2009,** 21, (2), 92-103.

20. Boon, E. M.; Marletta, M. A., Sensitive and Selective Detection of Nitric Oxide Using an H−NOX Domain. *Journal of the American Chemical Society* **2006,** 128, (31), 10022-10023.

21. Maragos, C. M.; Morley, D.; Wink, D. A.; Dunams, T. M.; Saavedra, J. E.; Hoffman, A.; Bove, A. A.; Isaac, L.; Hrabie, J. A.; Keefer, L. K., Complexes of .NO with nucleophiles as agents for the controlled biological release of nitric oxide. Vasorelaxant effects. *Journal of Medicinal Chemistry* **1991,** 34, (11), 3242-3247.

22. Keefer, L. K.; Nims, R. W.; Davies, K. M.; Wink, D. A., "NONOates" (1-substituted diazen-1-ium-1,2-diolates) as nitric oxide donors: Convenient nitric oxide dosage forms. In *Methods in Enzymology*, Lester, P., Ed. Academic Press: 1996; Vol. Volume 268, pp 281-293.

23. Davies, K. M.; Wink, D. A.; Saavedra, J. E.; Keefer, L. K., Chemistry of the Diazeniumdiolates. 2. Kinetics and Mechanism of Dissociation to Nitric Oxide in Aqueous Solution. *Journal of the American Chemical Society* **2001,** 123, (23), 5473-5481.

24. Bedioui, F.; Villeneuve, N., Electrochemical Nitric Oxide Sensors for Biological Samples – Principle, Selected Examples and Applications. *Electroanalysis* **2003,** 15, (1), 5-18.

25. McQuade, L. E.; Lippard, S. J., Fluorescent probes to investigate nitric oxide and other reactive nitrogen species in biology (truncated form: fluorescent probes of reactive nitrogen species). *Current Opinion in Chemical Biology* **2010,** 14, (1), 43-49.

26. Beckman, J. S.; Congert, K. A., Direct Measurement of Dilute Nitric Oxide in Solution with an Ozone Chemiluminescent Detector. *Methods* **1995,** 7, (1), 35-39.

27. Noack, E.; Kubitzek, D.; Kojda, G., Spectrophotometric determination of nitric oxide using hemoglobin. *Neuroprotocols* **1992,** 1, (2), 133-139.

28. Ertekin, V.; Selimoglu, M. A.; Türkan, Y.; Akçay, F., Serum Nitric Oxide Levels in Children with Celiac Disease. *Journal of Clinical Gastroenterology* **2005,** 39, (9), 782-785.

29. Sledzinski, T.; Sledzinski, M.; Smolenski, R.; Swierczynski, J., Increased Serum Nitric Oxide Concentration After Bariatric Surgery—A Potential Mechanism for Cardiovascular Benefit. *Obesity Surgery* **2010,** 20, (2), 204-210.

30. Fareed, D.; Iqbal, O.; Tobu, M.; Hoppensteadt, D. A.; Fareed, J., Blood Levels of Nitric Oxide, C-Reactive Protein, and Tumor Necrosis Factor-α Are Upregulated in Patients with Malignancy-Associated Hypercoagulable State: Pathophysiologic Implications. *Clinical and Applied Thrombosis/Hemostasis* **2004,** 10, (4), 357-364.

31. Hord, N. G.; Tang, Y.; Bryan, N. S., Food sources of nitrates and nitrites: the physiologic context for potential health benefits. *The American Journal of Clinical Nutrition* **2009,** 90, (1), 1-10.

32. Lundberg, J. O.; Weitzberg, E.; Gladwin, M. T., The nitrate-nitrite-nitric oxide pathway in physiology and therapeutics. *Nat Rev Drug Discov* **2008,** 7, (2), 156-167.

33. Griess, P., On a New Series of Bodies in Which Nitrogen is Substituted for Hydrogen. *Philosophical Transactions of the Royal Society of London* **1864,** 154, (ArticleType: research-article / Full publication date: 1864 /), 667-731.

34. Miranda, K. M.; Espey, M. G.; Wink, D. A., A Rapid, Simple Spectrophotometric Method for Simultaneous Detection of Nitrate and Nitrite. *Nitric Oxide* **2001,** 5, (1), 62-71.

35. Sun, J.; Zhang, X.; Broderick, M.; Fein, H., Measurement of Nitric Oxide Production in Biological Systems by Using Griess Reaction Assay. *Sensors* **2003,** 3, (8), 276-284.

36. Pluth, M. D.; Tomat, E.; Lippard, S. J., Biochemistry of Mobile Zinc and Nitric Oxide Revealed by Fluorescent Sensors. *Annual Review of Biochemistry* **2011,** 80, (1), 333-355.

37. Haussmann, H. J.; Werringloer, J., Nitric oxide and nitrite formation during degradation of N-nitrosamines. *Naunyn-Schmiedeberg's archives of pharmacology* **1985,** 329 (Supplement), R21.

38. Murphy, M. E.; Noack, E., Nitric oxide assay using hemoglobin method. In *Methods in Enzymology*, Lester, P., Ed. Academic Press: 1994; Vol. Volume 233, pp 240-250.

39. Shin, J. H.; Weinman, S. W.; Schoenfisch, M. H., Sol-gel derived amperometric nitric oxide microsensor. *Analytical Chemistry* **2005,** 77, (11), 3494-3501.

40. Christodoulou, D.; Kudo, S.; Cook, J. A.; Krishna, M. C.; Miles, A.; Grisham, M. B.; Murugesan, R.; Ford, P. C.; Wink, D. A., Electrochemical methods for detection of nitric oxide. In *Methods in Enzymology*, Lester, P., Ed. Academic Press: 1996; Vol. Volume 268, pp 69-83.

41. Malinski, T.; Taha, Z., Nitric oxide release from a single cell measured in situ by a porphyrinic-based microsensor. *Nature* **1992,** 358, (6388), 676-678.

42. Shibuki, K., An electrochemical microprobe for detecting nitric oxide release in brain tissue. *Neuroscience Research* **1990,** 9, (1), 69-76.

43. Shin, J. H.; Privett, B. J.; Kita, J. M.; Wightman, R. M.; Schoenfisch, M. H., Fluorinated Xerogel-Derived Microelectrodes for Amperometric Nitric Oxide Sensing. *Analytical Chemistry* **2008,** 80, (18), 6850-6859.

44. Piantadosi, C. A., Biological Chemistry of Carbon Monoxide. *Antioxidants & Redox Signaling* **2002,** 4, (2), 259-270.

45. Wu, L.; Wang, R., Carbon Monoxide: Endogenous Production, Physiological Functions, and Pharmacological Applications. *Pharmacological Reviews* **2005,** 57, (4), 585-630.

46. Fan, C.; Liu, X.; Pang, J.; Li, G.; Scheer, H., Highly sensitive voltammetric biosensor for nitric oxide based on its high affinity with hemoglobin. *Analytica Chimica Acta* **2004,** 523, (2), 225-228.

47. Bates, J. N., Nitric oxide measurement by chemiluminescence detection. *Neuroprotocols* **1992,** 1, (2), 141-149.

48. Kikuchi, K.; Nagano, T.; Hayakawa, H.; Hirata, Y.; Hirobe, M., Detection of nitric oxide production from a perfused organ by a luminol-hydrogen peroxide system. *Analytical Chemistry* **1993,** 65, (13), 1794-1799.

49. Nagano, T., Practical methods for detection of nitric oxide. *Luminescence* **1999,** 14, (6), 283-290.

50. Zhang, X.; Kim, W.-S.; Hatcher, N.; Potgieter, K.; Moroz, L. L.; Gillette, R.; Sweedler, J. V., Interfering with Nitric Oxide Measurements. *Journal of Biological Chemistry* **2002,** 277, (50), 48472-48478.

51. Kim, W.-S.; Ye, X.; Rubakhin, S. S.; Sweedler, J. V., Measuring Nitric Oxide in Single Neurons by Capillary Electrophoresis with Laser-Induced Fluorescence: Use of Ascorbate Oxidase in Diaminofluorescein Measurements. *Analytical Chemistry* **2006,** 78, (6), 1859-1865.

52. Broillet, M.-C.; Randin, O.; Chatton, J.-Y., Photoactivation and calcium sensitivity of the fluorescent NO indicator 4,5-diaminofluorescein (DAF-2): implications for cellular NO imaging. *FEBS Letters* **2001,** 491, (3), 227-232.

53. McQuade, L. E.; Ma, J.; Lowe, G.; Ghatpande, A.; Gelperin, A.; Lippard, S. J., Visualization of nitric oxide production in the mouse main olfactory bulb by a cell-trappable copper(II) fluorescent probe. *Proceedings of the National Academy of Sciences* **2010,** 107, (19), 8525-8530.

54. McQuade, L. E.; Lippard, S. J., Fluorescence-Based Nitric Oxide Sensing by Cu(II) Complexes That Can Be Trapped in Living Cells. *Inorganic Chemistry* **2010,** 49, (16), 7464-7471.

55. Lim, M. H.; Xu, D.; Lippard, S. J., Visualization of nitric oxide in living cells by a copper-based fluorescent probe. *Nat Chem Biol* **2006,** 2, (7), 375-380.

56. Sato, M.; Hida, N.; Umezawa, Y., Imaging the nanomolar range of nitric oxide with an amplifier-coupled fluorescent indicator in living cells. *Proceedings of the National Academy of Sciences of the United States of America* **2005,** 102, (41), 14515-14520.

57. Honda, A.; Adams, S. R.; Sawyer, C. L.; Lev-Ram, V.; Tsien, R. Y.; Dostmann, W. R. G., Spatiotemporal dynamics of guanosine 3 ',5 '-cyclic monophosphate revealed by a genetically encoded, fluorescent indicator. *Proceedings of the National Academy of Sciences of the United States of America* **2001,** 98, (5), 2437-2442.

58. Sato, M.; Nakajima, T.; Goto, M.; Umezawa, Y., Cell-Based Indicator to Visualize Picomolar Dynamics of Nitric Oxide Release from Living Cells. *Analytical Chemistry* **2006,** 78, (24), 8175-8182.

59. Tsikas, D., Review. *Free Radical Research* **2005,** 39, (8), 797-815.

60. Jungersten, L.; Edlund, A.; Petersson, A. S.; Wennmalm, Å., Plasma nitrate as an index of nitric oxide formation in man: analyses of kinetics and confounding factors. *Clinical Physiology* **1996,** 16, (4), 369-379.

61. Andersen, J. F.; Gudderra, N. P.; Francischetti, I. M. B.; Valenzuela, J. G.; Ribeiro, J. M. C., Recognition of Anionic Phospholipid Membranes by an Antihemostatic Protein from a Blood-Feeding Insect. *Biochemistry* **2004,** 43, (22), 6987-6994.

62. Knipp, M.; Yang, F.; Berry, R. E.; Zhang, H.; Shokhirev, M. N.; Walker, F. A., Spectroscopic and Functional Characterization of Nitrophorin 7 from the Blood-Feeding Insect Rhodnius prolixus Reveals an Important Role of Its Isoform-Specific N-Terminus for Proper Protein Function†. *Biochemistry* **2007,** 46, (46), 13254-13268.

63. Weichsel, A.; Andersen, J. F.; Roberts, S. A.; Montfort, W. R., Nitric oxide binding to nitrophorin 4 induces complete distal pocket burial. *Nat Struct Mol Biol* **2000,** 7, (7), 551-554.

64. Maes, E. M.; Roberts, S. A.; Weichsel, A.; Montfort, W. R., Ultrahigh Resolution Structures of Nitrophorin 4: Heme Distortion in Ferrous CO and NO Complexes†,‡. *Biochemistry* **2005,** 44, (38), 12690-12699.

65. Andersen, J. F.; Weichsel, A.; Balfour, C. A.; Champagne, D. E.; Montfort, W. R., The crystal structure of nitrophorin 4 at 1.5 å resolution: transport of nitric oxide by a lipocalin-based heme protein. *Structure* **1998,** 6, (10), 1315-1327.

66. Maes, E. M.; Weichsel, A.; Andersen, J. F.; Shepley, D.; Montfort, W. R., Role of Binding Site Loops in Controlling Nitric Oxide Release: Structure and Kinetics of Mutant Forms of Nitrophorin 4†,‡. *Biochemistry* **2004,** 43, (21), 6679-6690.

67. Stutz, H., Protein attachment onto silica surfaces – a survey of molecular fundamentals, resulting effects and novel preventive strategies in CE. *ELECTROPHORESIS* **2009,** 30, (12), 2032-2061.

68. Rabe, M.; Verdes, D.; Seeger, S., Understanding protein adsorption phenomena at solid surfaces. *Advances in Colloid and Interface Science* **2011,** 162, (1–2), 87-106.

69. Gray, J. J., The interaction of proteins with solid surfaces. *Current Opinion in Structural Biology* **2004,** 14, (1), 110-115.

70. Anand, G.; Sharma, S.; Dutta, A. K.; Kumar, S. K.; Belfort, G., Conformational Transitions of Adsorbed Proteins on Surfaces of Varying Polarity. *Langmuir* **2010,** 26, (13), 10803-10811.

71. Carré, A.; Lacarrière, V.; Birch, W., Molecular interactions between DNA and an aminated glass substrate. *Journal of Colloid and Interface Science* **2003,** 260, (1), 49-55.

72. Van Wagenen, R. A.; Andrade, J. D.; Hibbs, J. B., Streaming Potential Measurements of Biosurfaces. *Journal of The Electrochemical Society* **1976,** 123, (10), 1438-1444.

73. Hair, M. L.; Hertl, W., Acidity of surface hydroxyl groups. *The Journal of Physical Chemistry* **1970,** 74, (1), 91-94.

74. Bradshaw, J. T.; Mendes, S. B.; Saavedra, S. S., Planar Integrated Optical Waveguide Spectroscopy. *Analytical Chemistry* **2005,** 77, (1), 28 A-36 A.

75. Bradshaw, J. T.; Mendes, S. B.; Saavedra, S. S., A Simplified Broadband Coupling Approach Applied to Chemically Robust Sol−Gel, Planar Integrated Optical Waveguides. *Analytical Chemistry* **2002,** 74, (8), 1751-1759.

76. Saavedra, S. S.; Reichert, W. M., Integrated optical attenuated total reflection spectrometry of aqueous superstrates using prism-coupled polymer waveguides. *Analytical Chemistry* **1990,** 62, (20), 2251-2256.

77. Hu, X.; Feng, C.; Hazzard, J. T.; Tollin, G.; Montfort, W. R., Binding of YC-1 or BAY 41-2272 to Soluble Guanylyl Cyclase Induces a Geminate Phase in CO Photolysis. *Journal of the American Chemical Society* **2008,** 130, (47), 15748-15749.

78. Montfort, W. R.; Weichsel, A.; Andersen, J. F., Nitrophorins and related antihemostatic lipocalins from Rhodnius prolixus and other blood-sucking arthropods. *Biochimica et Biophysica Acta (BBA) - Protein Structure and Molecular Enzymology* **2000,** 1482, (1–2), 110-118.

79. Andersen, J. F.; Champagne, D. E.; Weichsel, A.; Ribeiro, J. M. C.; Balfour, C. A.; Dress, V.; Montfort, W. R., Nitric Oxide Binding and Crystallization of Recombinant Nitrophorin I, a Nitric Oxide Transport Protein from the Blood-Sucking Bug Rhodnius prolixus†. *Biochemistry* **1997,** 36, (15), 4423-4428.

80. Fritz, B. G.; Hu, X.; Brailey, J. L.; Berry, R. E.; Walker, F. A.; Montfort, W. R., Oxidation and Loss of Heme in Soluble Guanylyl Cyclase from Manduca sexta. *Biochemistry* **2011,** 50, (26), 5813-5815.

81. Fritz, B. G. Molecular Model of Soluble Guanylyl Cyclase Insight into Allostery in Nitric Oxide Signaling. Thesis, University of Arizona, Tucson, AZ, 2011.

82. Hrabie, J. A.; Klose, J. R.; Wink, D. A.; Keefer, L. K., New nitric oxide-releasing zwitterions derived from polyamines. *The Journal of Organic Chemistry* **1993,** 58, (6), 1472-1476.

83. Andersen, J. F.; Ding, X. D.; Balfour, C.; Shokhireva, T. K.; Champagne, D. E.; Walker, F. A.; Montfort, W. R., Kinetics and Equilibria in Ligand Binding by Nitrophorins 1−4: Evidence for Stabilization of a Nitric Oxide−Ferriheme Complex through a Ligand-Induced Conformational Trap†. *Biochemistry* **2000,** 39, (33), 10118-10131.

84. Miranda, K. M.; Nims, R. W.; Thomas, D. D.; Espey, M. G.; Citrin, D.; Bartberger, M. D.; Paolocci, N.; Fukuto, J. M.; Feelisch, M.; Wink, D. A., Comparison of the reactivity of nitric oxide

and nitroxyl with heme proteins: A chemical discussion of the differential biological effects of these redox related products of NOS. *Journal of Inorganic Biochemistry* **2003,** 93, (1–2), 52-60.

85. Berry, R.; Ding, X.; Shokhireva, T.; Weichsel, A.; Montfort, W.; Walker, F. A., Axial ligand complexes of theRhodnius nitrophorins: reduction potentials, binding constants, EPR spectra, and structures of the 4-iodopyrazole and imidazole complexes of NP4. *Journal of Biological Inorganic Chemistry* **2004,** 9, (2), 135-144.

86. Poulos, T. L., Soluble guanylate cyclase. *Current Opinion in Structural Biology* **2006,** 16, (6), 736-743.

87. Barker, S. L. R.; Clark, H. A.; Swallen, S. F.; Kopelman, R.; Tsang, A. W.; Swanson, J. A., Ratiometric and fluorescence lifetime-based biosensors incorporating cytochrome c ' and the detection of extra- and intracellular macrophage nitric oxide. *Analytical Chemistry* **1999,** 71, (9), 1767-1772.

88. Friebe, A.; Schultz, G.; Koesling, D., Sensitizing soluble guanylyl cyclase to become a highly CO-sensitive enzyme. *EMBO J.* **1996,** 15, (24), 6863-6868.

89. Evgenov, O. V.; Pacher, P.; Schmidt, P. M.; Hasko, G.; Schmidt, H. H. H. W.; Stasch, J.-P., NO-independent stimulators and activators of soluble guanylate cyclase: discovery and therapeutic potential. *Nat Rev Drug Discov* **2006,** 5, (9), 755-768.

90. Stones, J. R.; Marletta, M. A., Synergistic activation of soluble guanylate cyclase by YC-1 and carbon monoxide: implications for the role of cleavage of the iron-histidine bond during activation by nitric oxide. *Chemistry & biology* **1998,** 5, (5), 255-261.

91. Saibil, H., Macromolecular structure determination by cryo-electron microscopy. *Acta Crystallographica Section D* **2000,** 56, (10), 1215-1222.

92. Ludtke, S. J.; Baker, M. L.; Chen, D.-H.; Song, J.-L.; Chuang, D. T.; Chiu, W., De Novo Backbone Trace of GroEL from Single Particle Electron Cryomicroscopy. *Structure* **2008,** 16, (3), 441-448.

93. Ohi, M.; Li, Y.; Cheng, Y.; Walz, T., Negative staining and image classification — powerful tools in modern electron microscopy. *Biological Procedures Online* **2004,** 6, (1), 23-34.

94. Dubochet, J.; Groom, M.; Mueller-Neuteboom, S., *The Mounting of Macromolecules for Electron Microscopy with Particular Reference to Surface Phenomena and the Treatment of Support Films by Glow Discharge*. 1982.

95. Shiau, A. K.; Harris, S. F.; Southworth, D. R.; Agard, D. A., Structural Analysis of E. coli hsp90 Reveals Dramatic Nucleotide-Dependent Conformational Rearrangements. *Cell* **2006,** 127, (2), 329-340.

96. Southworth, D. R.; Agard, D. A., Species-Dependent Ensembles of Conserved Conformational States Define the Hsp90 Chaperone ATPase Cycle. *Molecular Cell* **2008,** 32, (5), 631-640.

97. Ludtke, S. J.; Baldwin, P. R.; Chiu, W., EMAN: Semiautomated Software for High-Resolution Single-Particle Reconstructions. *Journal of Structural Biology* **1999,** 128, (1), 82-97.

98. Ludtke, S. J.; Chen, D.-H.; Song, J.-L.; Chuang, D. T.; Chiu, W., Seeing GroEL at 6 Å Resolution by Single Particle Electron Cryomicroscopy. *Structure* **2004,** 12, (7), 1129-1136.

99. Tang, G.; Peng, L.; Baldwin, P. R.; Mann, D. S.; Jiang, W.; Rees, I.; Ludtke, S. J., EMAN2: An extensible image processing suite for electron microscopy. *Journal of Structural Biology* **2007,** 157, (1), 38-46.

100. Jain, N. K.; Roy, I., Effect of trehalose on protein structure. *Protein Science* **2009,** 18, (1), 24-36.

101. Anderson, N. L.; Anderson, N. G., The Human Plasma Proteome. *Molecular & Cellular Proteomics* **2002,** 1, (11), 845-867.

102. Shao, W.; Zhou, Z.; Laroche, I.; Lu, H.; Zong, Q.; Patel, D. D.; Kingsmore, S.; Piccoli, S. P., Optimization of Rolling-Circle Amplified Protein Microarrays for Multiplexed Protein Profiling. *Journal of Biomedicine and Biotechnology* **2003,** 2003, (5), 299-307.

103. Schweitzer, B.; Roberts, S.; Grimwade, B.; Shao, W.; Wang, M.; Fu, Q.; Shu, Q.; Laroche, I.; Zhou, Z.; Tchernev, V. T.; Christiansen, J.; Velleca, M.; Kingsmore, S. F., Multiplexed protein profiling on microarrays by rolling-circle amplification. *Nat Biotech* **2002,** 20, (4), 359-365.

104. Gavin, A.-C.; Aloy, P.; Grandi, P.; Krause, R.; Boesche, M.; Marzioch, M.; Rau, C.; Jensen, L. J.; Bastuck, S.; Dumpelfeld, B.; Edelmann, A.; Heurtier, M.-A.; Hoffman, V.; Hoefert, C.; Klein, K.; Hudak, M.; Michon, A.-M.; Schelder, M.; Schirle, M.; Remor, M.; Rudi, T.; Hooper, S.; Bauer, A.; Bouwmeester, T.; Casari, G.; Drewes, G.; Neubauer, G.; Rick, J. M.; Kuster, B.; Bork, P.; Russell, R. B.; Superti-Furga, G., Proteome survey reveals modularity of the yeast cell machinery. *Nature* **2006,** 440, (7084), 631-636.

105. Washburn, M. P.; Wolters, D.; Yates, J. R., Large-scale analysis of the yeast proteome by multidimensional protein identification technology. *Nat Biotech* **2001,** 19, (3), 242-247.

106. Mattoon, D.; Merkel, J.; Michaud, G.; Schweitzer, B., Biomarker discovery using protein microarray technology platforms: antibody-antigen complex profiling. *Expert Review of Proteomics* **2005,** 2, (6), 879+.

107. Ingvarsson, J.; Wingren, C.; Carlsson, A.; Ellmark, P.; Wahren, B.; Engström, G.; Harmenberg, U.; Krogh, M.; Peterson, C.; Borrebaeck, C. A. K., Detection of pancreatic cancer using antibody microarray-based serum protein profiling. *PROTEOMICS* **2008,** 8, (11), 2211-2219.

108. Wingren, C.; Borrebaeck, C. A. K., Antibody-Based Microarrays *Methods in Molecular Biology* **2009,** 509, 57-84.

109. MacBeath, G.; Schreiber, S. L., Printing Proteins as Microarrays for High-Throughput Function Determination. *Science* **2000,** 289, (5485), 1760-1763.

110. Cretich, M.; di Carlo, G.; Longhi, R.; Gotti, C.; Spinella, N.; Coffa, S.; Galati, C.; Renna, L.; Chiari, M., High Sensitivity Protein Assays on Microarray Silicon Slides. *Analytical Chemistry* **2009,** 81, (13), 5197-5203.

111. Pawlak, M.; Schick, E.; Bopp, M. A.; Schneider, M. J.; Oroszlan, P.; Ehrat, M., Zeptosens' protein microarrays: A novel high performance microarray platform for low abundance protein analysis. *PROTEOMICS* **2002,** 2, (4), 383-393.

112. Kusnezow, W.; Jacob, A.; Walijew, A.; Diehl, F.; Hoheisel, J. D., Antibody microarrays: An evaluation of production parameters. *PROTEOMICS* **2003,** 3, (3), 254-264.

113. Angenendt, P.; Glökler, J.; Murphy, D.; Lehrach, H.; Cahill, D. J., Toward optimized antibody microarrays: a comparison of current microarray support materials. *Analytical Biochemistry* **2002,** 309, (2), 253-260.

114. Charles, P. T.; Goldman, E. R.; Rangasammy, J. G.; Schauer, C. L.; Chen, M.-S.; Taitt, C. R., Fabrication and characterization of 3D hydrogel microarrays to measure antigenicity and antibody functionality for biosensor applications. *Biosensors and Bioelectronics* **2004,** 20, (4), 753-764.

115. Stillman, B. A.; Tonkinson, J. L., FASTÔ Slides: A Novel Surface for Microarrays. *BioTechniques* **2000,** 29, 630-635.

116. Zheng, S.; Zhang, H.; Ross, E.; Le, T. V.; Wirth, M. J., Silica Colloidal Crystals for Enhanced Fluorescence Detection in Microarrays. *Analytical Chemistry* **2007,** 79, (10), 3867-3872.

117. Mihi, A.; Ocaña, M.; Míguez, H., Oriented Colloidal-Crystal Thin Films by Spin-Coating Microspheres Dispersed in Volatile Media. *Advanced Materials* **2006,** 18, (17), 2244-2249.

118. Jiang, P.; McFarland, M. J., Large-Scale Fabrication of Wafer-Size Colloidal Crystals, Macroporous Polymers and Nanocomposites by Spin-Coating. *Journal of the American Chemical Society* **2004,** 126, (42), 13778-13786.

119. Van Le, T.; Ross, E. E.; Velarde, T. R. C.; Legg, M. A.; Wirth, M. J., Sintered Silica Colloidal Crystals with Fully Hydroxylated Surfaces. *Langmuir* **2007,** 23, (16), 8554-8559.

120. Pease, L. F.; Elliott, J. T.; Tsai, D.-H.; Zachariah, M. R.; Tarlov, M. J., Determination of protein aggregation with differential mobility analysis: Application to IgG antibody. *Biotechnology and Bioengineering* **2008,** 101, (6), 1214-1222.

121. Freeman, N. J.; Peel, L. L.; Swann, M. J.; Cross, G. H.; Reeves, A.; Brand, S.; Lu, J. R., Real time, high resolution studies of protein adsorption and structure at the solid–liquid interface using dual polarization interferometry. *Journal of Physics: Condensed Matter* **2004,** 16, (26), S2493-S2496.